Tectonics

RESEARCH ARTICLE
10.1029/2019TC005677

Special Section:
Tethyan dynamics: from rifting to collision

The Age, Origin, and Emplacement of the Tsiknias Ophiolite, Tinos, Greece

Thomas N. Lamont[1,2], Nick M.W. Roberts[3], Michael P. Searle[1], Phillip Gopon[1], David J. Waters[1], and Ian Millar[3]

[1]Department Earth Sciences, Oxford University, Oxford, UK, [2]Now at: School of Earth and Environmental Sciences, University of St Andrews, St Andrews, UK, [3]Geochronology and Tracers Facility, British Geological Survey, Nottingham, UK

Abstract The Tsiknias Ophiolite, exposed at the highest structural levels of Tinos, Greece, represents a thrust sheet of Tethyan oceanic crust and upper mantle emplaced onto the Attic-Cycladic Massif. We present new field observations and a new geological map of Tinos, integrated with petrology, THERMOCALC phase diagram modeling, U–Pb geochronology and whole rock geochemistry, resulting in a tectonothermal model that describes the formation and emplacement of the Tsiknias Ophiolite and newly identified underlying metamorphic sole. The ophiolite comprises a succession of partially dismembered and structurally repeated ultramafic and gabbroic rocks that represent the Moho Transition Zone. A plagiogranite dated by U-Pb zircon at 161.9 ± 2.8 Ma, reveals that the Tsiknias Ophiolite formed in a suprasubduction zone setting, comparable to the "East-Vardar Ophiolites," and was intruded by gabbros at 144.4 ± 5.6 Ma. Strongly sheared metamorphic sole rocks show a condensed and inverted metamorphic gradient, from partially anatectic amphibolites at *P-T* conditions of ~8.5 kbar 850–600 °C, downstructural section to greenschist-facies oceanic metasediments over ~250 m. Leucosomes generated by partial melting of the uppermost sole amphibolite, yielded a U-Pb zircon protolith age of ~190 Ma and a high-grade metamorphic-anatectic age of 74.0 ± 3.5 Ma associated with ophiolite emplacement. The Tsiknias Ophiolite was therefore obducted ~90 Myr after it formed during initiation of a NE dipping intraoceanic subduction zone to the northeast of the Cyclades that coincides with Africa's plate motion changing from transcurrent to convergent. Continued subduction resulted in high-pressure metamorphism of the Cycladic continental margin ~25 Myr later.

Plain Language Summary Ophiolites (fragments of oceanic crust and mantle pushed onto the continents) are distributed throughout the Aegean and record the traces of relict subduction zones that were responsible for the closure of an earlier ocean to the Mediterranean (Tethys Ocean). In this work, the Tsiknias Ophiolite on Tinos, Greece, was investigated to improve our understanding of the geodynamic evolution of the Aegean. A new geological map of Tinos is presented and integrated with phase diagram modeling, geochemistry, and U-Pb dating of rocks from the ophiolite sequence and high-temperature metamorphic rocks beneath the ophiolite (Metamorphic Sole). The Tsiknias Ophiolite formed at 161.9 ± 2.8 Ma above a subduction zone, comparable to ophiolites on mainland Greece. The underlying Metamorphic Sole rocks comprise of hot mafic rocks at the top and colder oceanic sedimentary rocks at the bottom. The hottest rocks represent oceanic crust that formed at ~190 Ma and experienced heating and partial melting at 74 ± 3.5 Ma. The Metamorphic Sole formed by heating and shearing in a protosubduction zone ~90 Myr after the overlying ophiolite formed. Subduction continued until ~52–46 Ma, when the Adriatic continental margin jammed this subduction zone marking the collision between Adria and Eurasia.

Key Points:
- The Tsiknias Ophiolite formed at 161.9 ± 2.8 Ma in a suprasubduction zone environment, similar to "East Vardar Ophiolites"
- The Metamorphic Sole formed at ~74 ± 3.5 Ma, at *P-T* conditions of 8.5 kbar and 600–850 °C during the NE dipping subduction initiation
- Subduction of the Cycladic continental margin at ~52–46 Ma resulted in high-pressure metamorphism, as the Southern Vardar Ocean closed

Supporting Information:
- Supporting Information S1
- Table S1
- Table S2
- Table S3
- Figure S1

Correspondence to:
T. N. Lamont,
tnl1@st-andrews.ac.uk

Citation:
Lamont, T. N., Roberts, N. M. W., Searle, M. P., Gopon, P., Waters, D. J., & Millar, I. (2020). The age, origin, and emplacement of the Tsiknias Ophiolite, Tinos, Greece. *Tectonics*, *39*, e2019TC005677. https://doi.org/10.1029/2019TC005677

Received 20 MAY 2019
Accepted 8 SEP 2019
Accepted article online 26 SEP 2019

1. Introduction

Ophiolites are distributed along the entire Alpine-Himalayan belt and record oceanic spreading events within Neo-Tethys from late Jurassic to Eocene times (Figure 1). Together, these rocks have important implications for the regional-scale geodynamics, as they are interpreted as fragments of oceanic lithosphere emplaced onto continental margins during the early stages of orogenesis. In the Hellenides and Dinarides (Albania, Greece, Bulgaria, Croatia, and Serbia; Figure 1) most ophiolites (Dinaric-Mirdita-Pindos-Vourinous-Orthis and Guevgueli Ophiolites) have Jurassic U–Pb ages (e.g., Dilek et al., 2007; Froitzheim et al., 2014; Liati et al., 2004; Zachariadis, 2007), whereas most ophiolites in the Turkish Taurides and

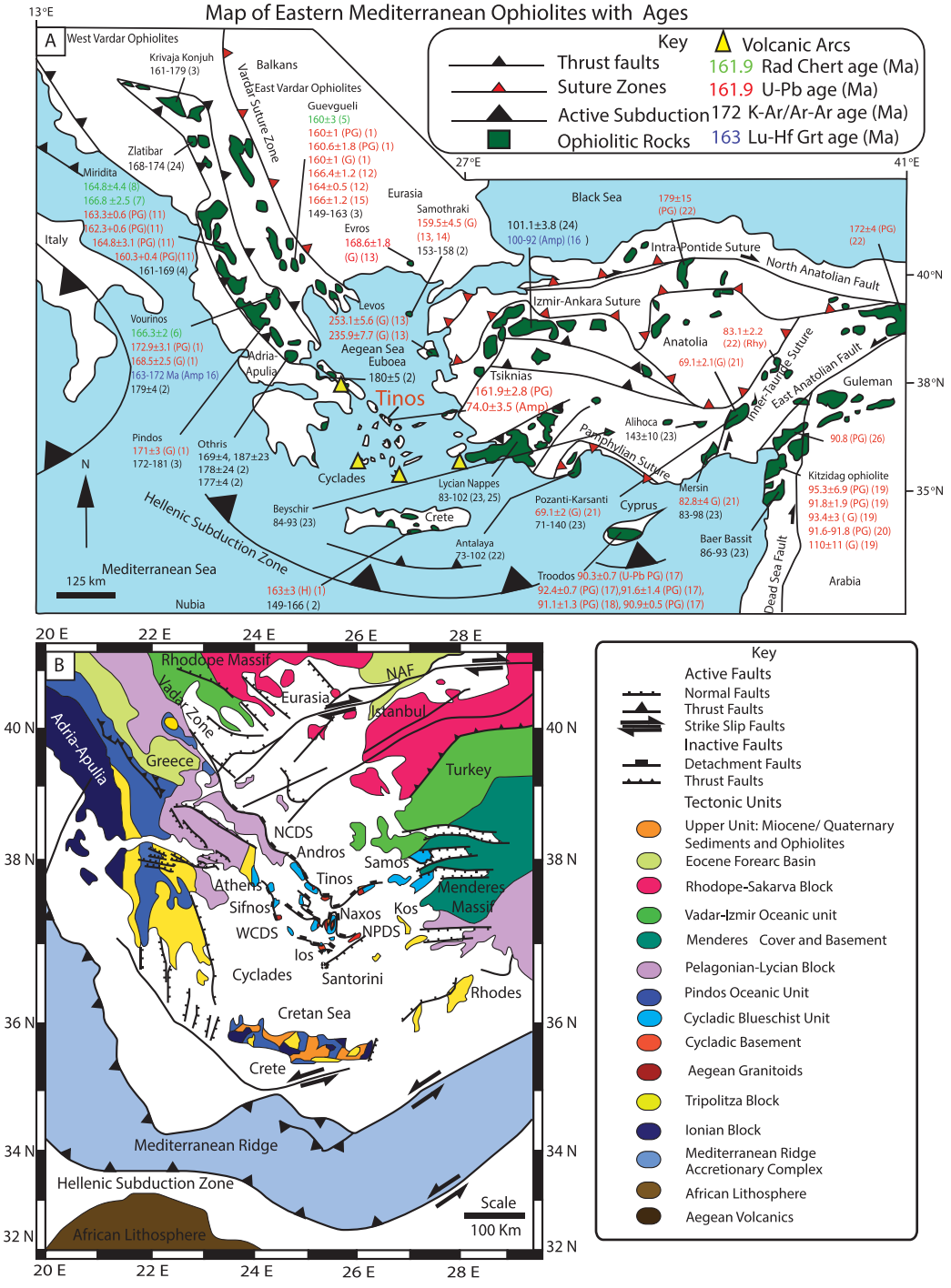

Figure 1. (a) Summary map of Aegean Ophiolites with their reported geochronology ages and uncertainties. G = Gabbro, PG = Plagiogranite, Amp = Amphibolite from the metamorphic sole, H = Hornblendite. Reported ^{40}Ar-^{39}Ar, ^{40}K-^{39}Ar, and Lu-Hf ages are from the ophiolite metamorphic soles. References: (1) Liati et al. (2004; U-Pb); (2) Ferriére (1982) ^{40}Ar-^{39}Ar; (3) Spray et al. (1984) ^{40}Ar-^{39}Ar, (4) Dimo-Lahitte et al. (2001) ^{40}Ar-^{39}Ar; (5) Jones and Robertson (1991) ^{40}Ar-^{39}Ar; (6) Danelian et al. (1996; radiolarian cherts); (7) Chiari et al. (2003; radiolarian cherts); (8) Prela et al. (2000; radiolarian cherts); (9) Marcucci et al. (1994) and Chiari et al. (1994; radiolarian cherts); (10) Zachariadis (2007; U-Pb); (11) Dilek et al. (2008); (12) Božović et al. (2013) U-Pb and ^{40}Ar-^{39}Ar; (13) Koglin (2008) U-Pb; (14) Koglin et al. (2009) U-Pb; (14) and (15) Kukoč et al. (2015; radiolarian cherts); (16) Peters et al. (2017) Lu-Hf garnet; (17) Mukasa and Ludden (1987) U-Pb; (18) Konstantinou et al. (2007) U-Pb; (19) Karaoğlan, Parlak, Kloetzli, Thöni, et al. (2013) U-Pb; (20) Dilek and Thy (2009); (21) Parlak et al. (2013); (22) Topuz et al. (2012) U-Pb; (23) Thuizat et al. (1981) ^{40}K-^{40}Ar; (24) Harris et al. (1994) ^{40}K-^{40}Ar; (25) Okrusch et al. (1978) ^{40}K-^{40}Ar; (26) Sarıfakıoğlu et al. (2012) U-Pb. (b) A regional tectonic map of the Aegean showing the major tectonostratigraphic units and structures; NCDS = North Cycladic Detachment System, WCDS = West Cycladic Detachment System, NPDS = Naxos–Paros Detachment System, NAF = North Anatolian Fault.

Pontides are Cretaceous in age (e.g., Çelik et al., 2006; Parlak et al., 2013; Karaoğlan et al., 2013; Peters et al., 2017). High-temperature metamorphic rocks, known as metamorphic soles, underlie many of these ophiolites and record the subduction processes during the initial stages of their obduction histories. A range of ^{40}Ar–^{39}Ar, U–Pb, and Lu–Hf garnet ages (Jones & Robertson, 1991; Parlak et al., 2013; Karaoğlan et al., 2013; Peters et al., 2017) show that these features usually form at the same time as the ophiolites directly above them. Suprasubduction zone (SSZ) geochemical signatures of the ophiolites support a model whereby ophiolite protoliths formed above subduction zones and were emplaced onto the respective continental margins during ocean closure (e.g., Maffione & van Hinsbergen, 2018; Schmid et al., 2008; Sharp & Robertson, 2006; Wakabayashi & Dilek, 2000).

In the Aegean Sea area (Figure 1), several distinct ophiolite belts record traces of subduction zones that were active at different times during the closure of the Neo-Tethys Ocean. These include the Dinaric-Mirdita-Pindos-Vourinos-Orthis Ophiolites that make up the "Western Vardar Ophiolites" that sit on Adriatic-Apulian continental crust, and the Guevgueli and Serbo-Macedonian Ophiolites that make up the "Eastern Vardar Ophiolites" that lie on Eurasian continental crust (Schmid et al., 2008). However, integrating these ophiolites into regional geodynamic models is often difficult as most occur as isolated fragments and have been overprinted by subsequent tectonic movements (e.g., Bortolotti et al., 2013; Maffione & van Hinsbergen, 2018; Sharp & Robertson, 2006). Topics of debate include the following: (1) How do the Balkan ophiolites relate to the younger Turkish ophiolites? (2) At what time did the Neo-Tethys Ocean close and was this associated with the closure of one, two, or three basins? (3) Are ophiolitic rocks within the Aegean Sea related and can they be correlated to the surrounding well-studied ophiolite belts?

The Cycladic Islands in southern Greece (Figure 1b) are a key area for addressing all of these questions. Rocks of ophiolitic affinity crop out commonly along shear zones and mélanges within eclogite- and blueschist-facies rocks, or at higher levels bounded by low-angle normal faults associated with Miocene to present-day extension of the Aegean region (Avigad & Garfunkel, 1989, 1991; Brichau et al., 2007; Jansen, 1973; Jansen & Schuiling, 1976; Jolivet et al., 2010; Katzir et al., 2007, 2002, 1996; Keay et al., 2001; Lamont et al., 2019; Melidonis, 1980; Stouraiti et al., 2017). Studies on the most complete ophiolite sections from several islands (Tinos, Andros, Ikaria, Paros, Naxos, Mykonos, Samos, and Skyros), which are at high structural levels, indicate that these bodies have a range of geochemical affiliations, including SSZ to ocean island basalts (OIB). Despite this work, there remains a limited understanding about how these rocks fit in with the current understanding of Aegean tectonics, as these sections are variably dismembered (Katzir et al., 2007, 2002, 1996; Stouraiti et al., 2017), and there is incomplete knowledge about their origin, emplacement mechanism(s), and their structural relationships to other metamorphic rocks of the Cyclades. It is poorly understood whether they form part of the same ophiolite sequence and can be correlated with other Balkan or Anatolian ophiolites, or whether they represent completely separate ocean crust formation and obduction event(s) that are not recorded elsewhere in the eastern Mediterranean. To help answer these questions, in this contribution we present a new geological map of Tinos and field observations, together with petrology, whole rock geochemistry, and U–Pb geochronology of the hitherto poorly understood Tsiknias Ophiolite exposed on Tinos, as well as a newly identified underlying metamorphic sole. These data provide new constraints on the geodynamic history of the Aegean region since the Jurassic.

2. Geology of Tinos

Tinos lies along the northern margin of the Cycladic-Attic Massif (Figure 1b). The island comprises of two distinct tectonostratigraphic units that each experienced a different tectonic and metamorphic histories. The "Lower Unit" (Bröcker et al., 1993) comprises continental margin lithologies that attained (M_1) blueschist-eclogite-facies conditions whereas the "Upper Unit" including ophiolitic rocks did not experience high pressures. Pioneering work by Melidonis (1980), Avigad and Garfunkel (1989), and Katzir et al. (1996) highlighted that the island is a northwest-southeast striking elongate dome composed of mainly retrogressed high-pressure rocks with variable amounts of intercalated fresh blueschists and some eclogite localities (e.g., Kionnia Peninsular; Figures 2 and 3) that are bounded by a major greenschist-facies extensional shear zone with top-to-NE kinematics (Tinos Shear Zone). The Tinos Shear Zone truncates and separates the high-pressure rocks in the footwall (Lower Unit) against the Upper Unit (Katzir et al., 1996; Melidonis, 1980; Patzak et al., 1994). This structure has been interpreted as part of the North Cycladic Detachment System

10.1029/2019TC005677

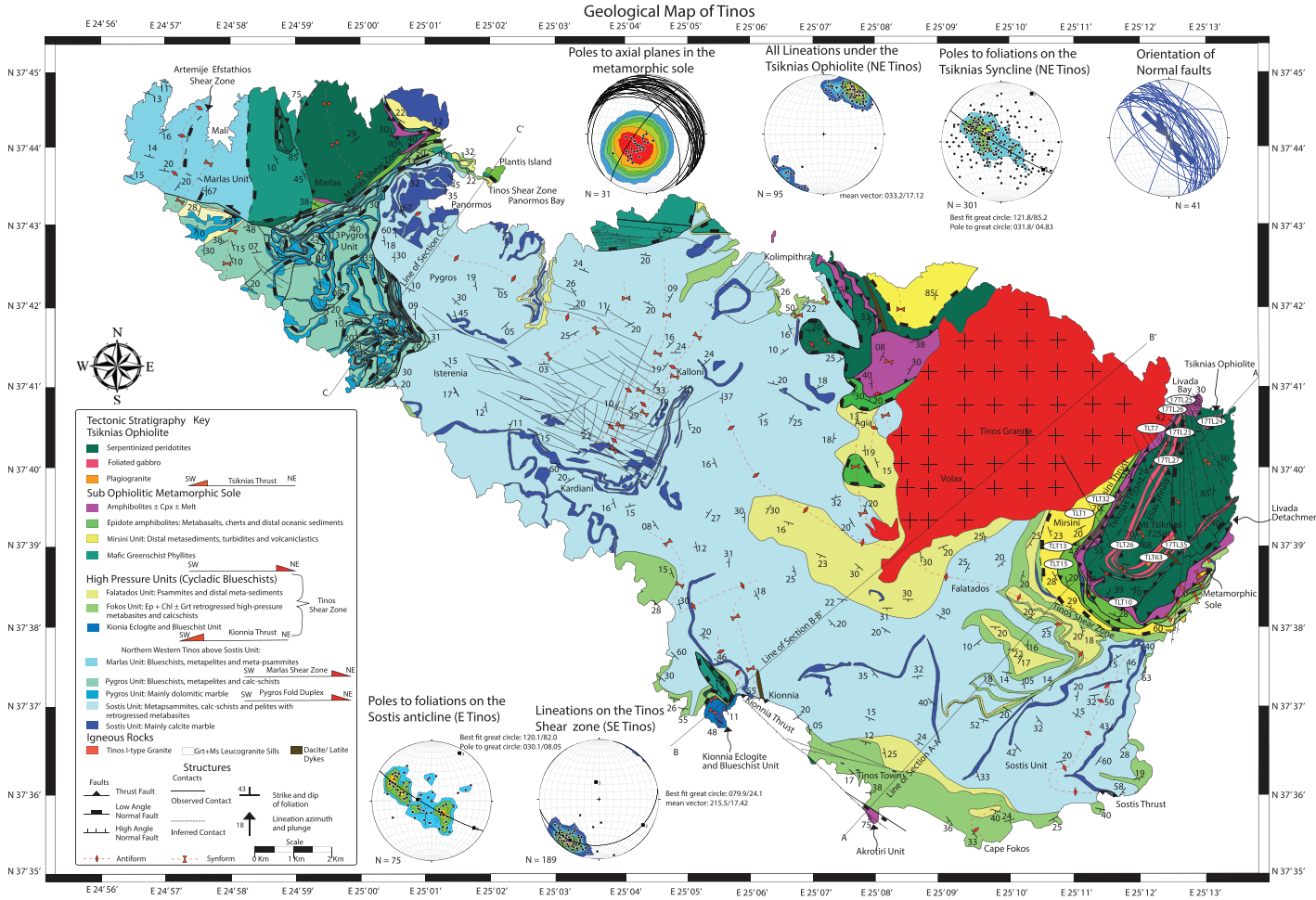

Figure 2. New geological map of Tinos with accompanying cross sections. The location of all samples described in the study are labeled, with major thrusts, normal faults, and fold axes. Stereonets of structural data from various parts of Tinos Upper Unit. NE plunging lineations in the sole of the Tsiknias Ophiolite, poles to fold axial planes in SW verging isoclinal folds in the metamorphic sole and Mirsini Unit in NE Tinos. Normal fault planes of normal faults in the Upper Unit commonly striking around 330/60 indicating ENE/WSW extension in present-day coordinates. Kilometer-scale upright open folds affecting both the Lower Unit and the Upper Unit with fold axial planes striking NE-SW indicating a component of E-W shortening, for example, Mount Tsiknias in NE Tinos represents an upright gently NE plunging synform. For cross-sections A–A′, B–B′, and C–C′ consult Figure 3.

(NCDS; Jolivet et al., 2004, 2010, 2013), a series of low-angle normal faults and shear zones interpreted to have formed during Miocene extension in the central Aegean. This shear zone is folded around Tinos island (Figure 3) and crosscut by a 14.6 Ma I-type granite (Brichau et al., 2007), various ~15 Ma dacite dykes, and ~14–13 Ma leucogranite sills (Avigad & Garfunkel, 1989; Katzir et al., 2007, 2002, 1996; Jolivet et al., 2010; Lamont, 2018). These relationships indicate that the shear zone was active prior to ~14.6 Ma. The Upper Unit comprises a thrust sheet of ophiolitic material including peridotites, gabbros, low-grade schists, and mafic phyllites, which are the subject of this paper. The Akrotiri Unit (Figures 2 and 5g) crops out on the island's southern coastline near Tinos Town and exposes meta-basalts and metasedimentary rocks metamorphosed to upper amphibolite-facies conditions (Patzak et al., 1994) and show no evidence for experiencing high-pressure conditions.

Previous K–Ar, ^{40}Ar–^{39}Ar, and Rb–Sr ages of the Upper Unit range from 95 to 13 Ma and include 95–47 Ma ages for metagabbros from Mount Tsiknias, and a ^{40}Ar–^{39}Ar plateau age of ~72 Ma for a metabasalt on Cape Fokos, SE Tinos (Figure 2; Zeffren et al., 2005). There are also ~76–66 Ma K–Ar ages from the Akrotiri Unit (Patzak et al., 1994), indicating a possible Late Cretaceous age of either formation, metamorphism, or emplacement of meta-basalts and gabbros within the Upper Unit. This contrasts with the Eocene high-pressure

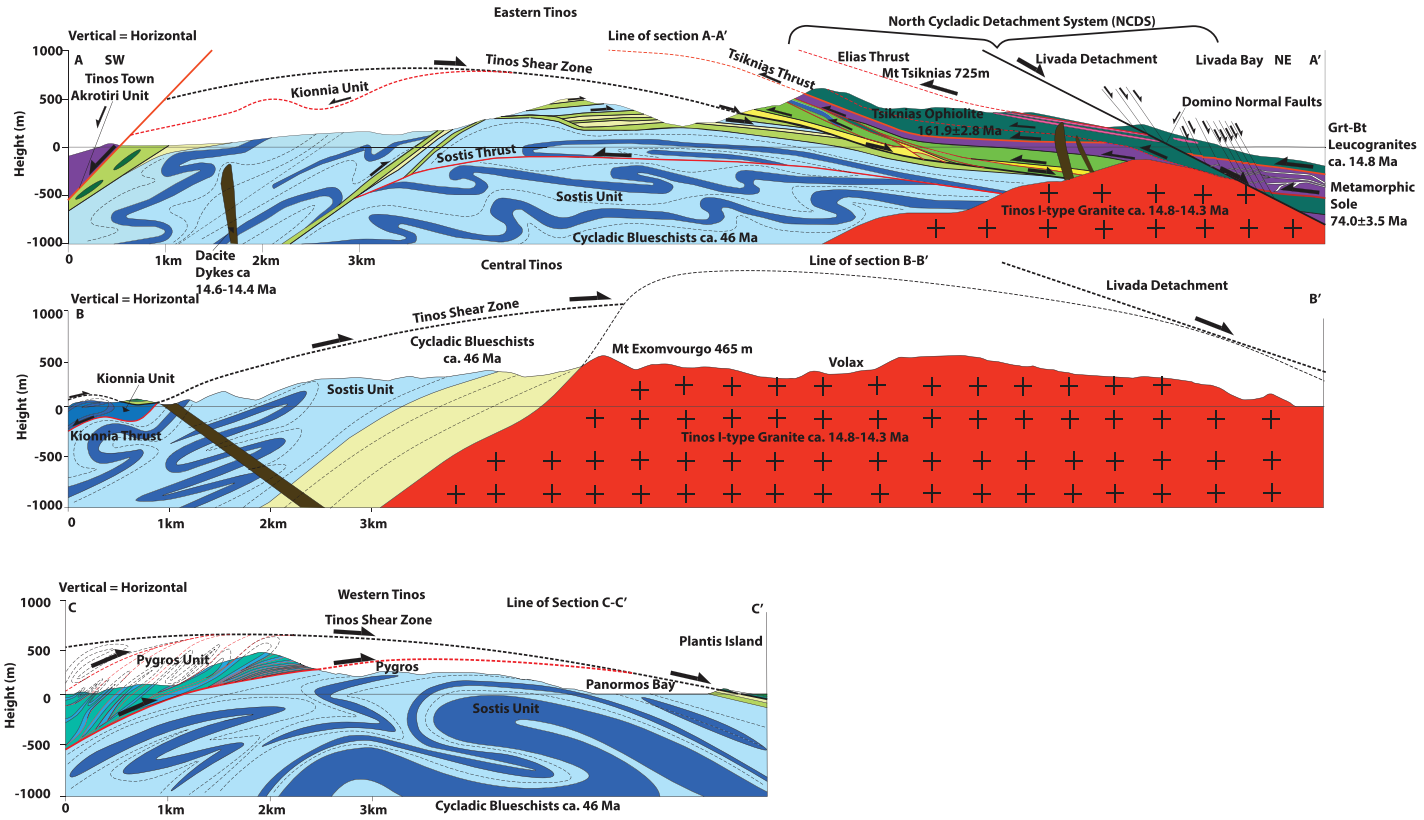

Figure 3. Cross sections through Tinos along the line of sections A-A′, B-B′, and C-C′. For locations consult the geological map in Figure 2. The thick red lines are tectonic contacts active during the ophiolite obduction high-pressure metamorphism stage (Late Cretaceous-Eocene) and the thick black lines are tectonic contacts active during the Miocene that crosscut the earlier structures.

metamorphic rocks in the Lower Unit, dated by ^{40}Ar-^{39}Ar on Tinos (Bröker et al., 1993) and indirectly by correlative rocks on other islands at ~52–45 Ma by U–Pb zircon (Tomaschek et al., 2003) and Lu–Hf in garnet (Dragovic et al., 2012, 2015; Lagos et al., 2007). However, there are inherent problems in determining what part of the rock's complex history is actually being dated with the K–Ar, ^{40}Ar–^{39}Ar, and Rb–Sr methods (e.g., Kelley, 2002; MacDonald et al., 2017; Bosse & Villa, 2019). Here we present new U–Pb zircon dates for the timing of formation and emplacement of the Tsiknias Ophiolite within the Upper Unit.

3. Methods and Scientific Rationale

A multidisciplinary approach was used in this study by integrating field and microstructural observations, electron microprobe analysis (EMPA), conventional thermobarometry, THERMOCALC phase diagram modeling, whole rock geochemistry, and U–Pb geochronology. Combining these methods provides great insight into the tectonothermal evolution of the Upper Unit on Tinos, which has significant implications for our understanding of Aegean geodynamics and the closure of the Tethys Ocean.

3.1. Field Methods

Structural mapping of Tinos Island was carried out at a 1:10,000 scale between 2015 and 2018, with new and important interpretations of both the Upper and Lower units. A new geological map of the entire island is presented in Figure 2 and in the supporting information Figure S1, with accompanying cross sections in Figure 3, and panoramic photographs in Figure 4. A tectonostratigraphic column is shown in Figure 5, with key field relationships shown in Figure 6 and the supporting information. A summary of the key tectono-stratigraphic units within the Upper Unit are presented in Table 1. A future paper will present the structural, petrographic, and thermobarometric results of the Lower Unit.

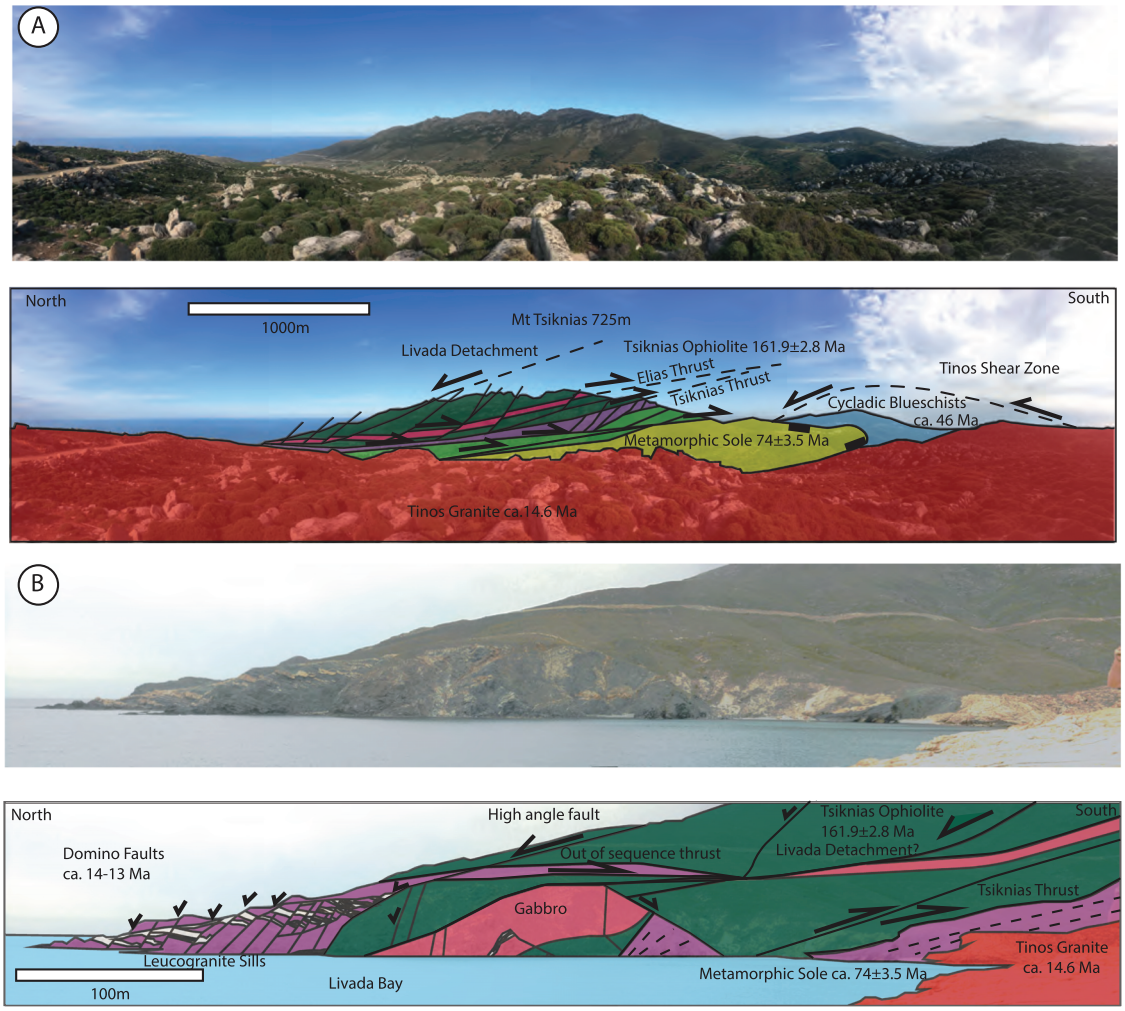

Figure 4. Panoramic photographs of the Tsiknias Ophiolite, metamorphic sole, and Livada Detachments. (a) Panoramic view of the Tsiknias Ophiolite and underlying sole illustrating its klippen structure on the Mount Tsiknias ridge (taken from N37.595986, E25.206158). (b) Panorama of Livada Bay showing the metamorphic sole, structural repetition and out of sequence thrusting and I-type granite intrusion (taken from N37.611794, E25.236271).

3.2. EMPA Methods

Samples of key rock types were collected, made into polished thin sections, and investigated with optical microscopy to determine the characteristic mineral assemblages and microstructures. The compositions of phases were derived from EMPA using a CAMECA SX5-FE (field emission) electron microprobe at the Department of Earth Sciences, University of Oxford. Operating conditions were as follows: an accelerating voltage of 15 keV, a current of 20 nA; a range of primary and secondary standards were used including andradite (Fe, Mg, and Ca), TiO2 (Ti), Mn metal (Mn), labradorite (Na, Al, and Si), and sanidine (K) for major elements and synthetic REE standards obtained from the Univeristy of Edinburough. For a complete description of analytical procedures, see the Text S1 and Table S1 for the complete EMPA data set across all studied samples.

3.3. Thermobarometry Methods

To determine the pressure (P) and temperature (T) evolution of the ophiolitic and metamorphic rocks, we used conventional thermobarometry using THERMOCALC mode 2; Average P–T (Av-PT), the Al in amphibole barometer, amphibole-plagioclase, and Ti-in-biotite thermobarometry and where possible the garnet-Cpx thermometer (Holland & Powell, 2011; Schmidt, 1992; Anderson & Smith 1995; Holland & Blundy, 1994; Henry et al., 2005; Powell, 1985 and Ravna, 2000). Equilibrium phase diagram modeling was also

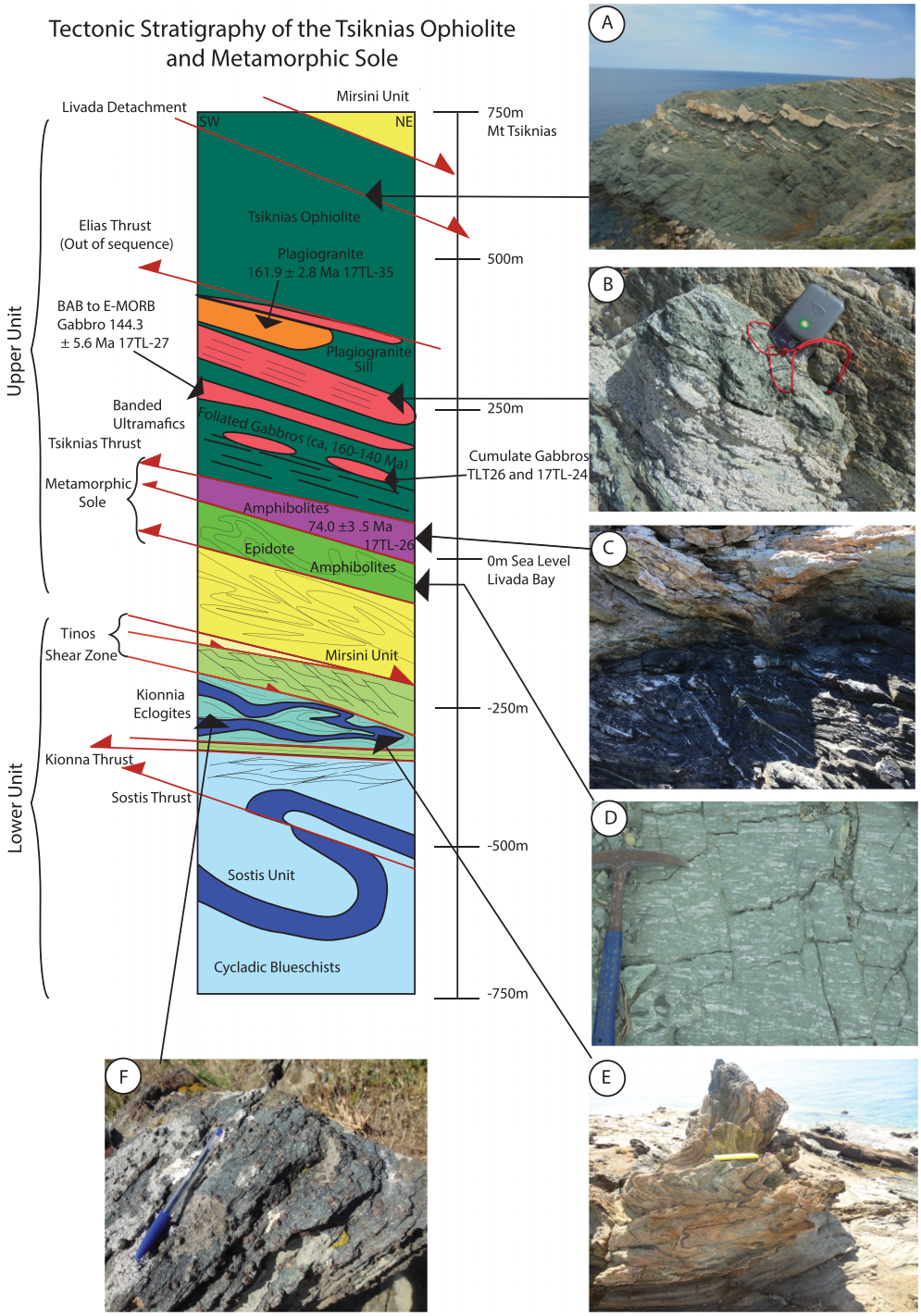

Figure 5. Annotated stratigraphic section through the Tsiknias Ophiolite and metamorphic sole, with outcrop photographs. (a) Domino style normal faults through the metamorphic sole at Livada Bay (N37.612559, E25.242034), rooting into the Livada Detachment. Granite sills emanate from the I-type granite and are pretectonic, although in places some degree of plasticity minor rotation into the fault planes can be seen. (b) Foliated hornblende rich gabbro bounded by serpentinized peridotites within the Moho-Transition Zone (N37.581116, E25.221087). (c) The Tsiknias Thrust at Livada Bay (N37.609901, E25.238966). Dark amphibolites below with white leuco-diorite melt veins emanating from the contact and pale completely serpentinzed and sheared ultramafics above. (d) Mylonitized amphibolite from the metamorphic sole with an exceptionally strong fabric and lineation defined by elongated plagioclase porphyroblasts indicating flattening strains of ~4:1, taken at (N37.609616, E25.238603) in Livada Bay. (e) Isoclinally folded eclogite-facies metasediments within the Kionnia Nappe of the Cycladic Blueschist Unit (Lamont, 2018) in the footwall of the Tinos Shear zone (taken at N37.547897, E25.125450). (f) Mafic eclogite within the Kionnia Unit of the Cycladic Blueschist Unit, associated with attempted subduction down a NE dipping subduction zone (Lamont, 2018) in the footwall of the Tinos Shear zone (taken at N37.550536, E25.124504).

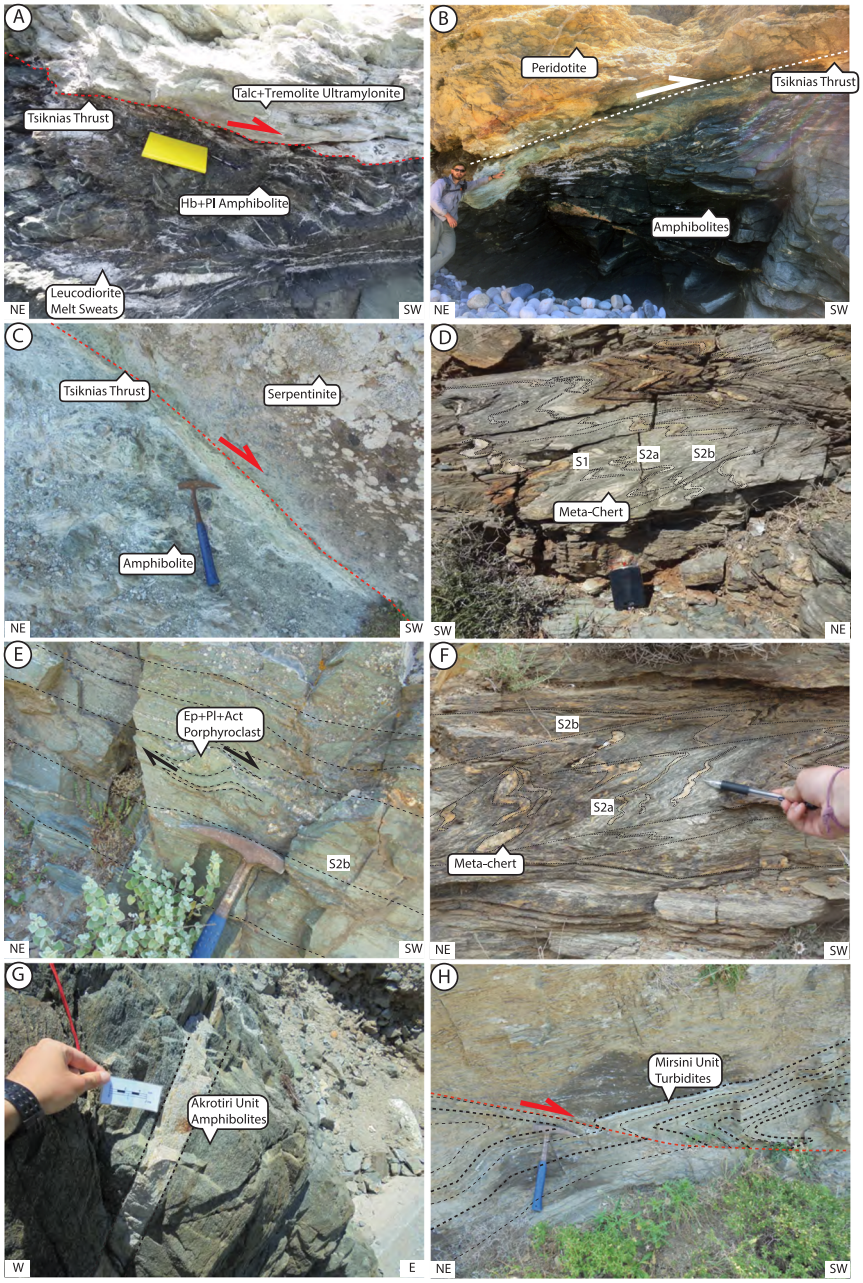

Figure 6. Annotated outcrop photographs of the metamorphic sole and Mirsini Unit, showing the range in lithology and deformation in these units. (a) The Tsiknias Thrust at Livada Bay (N37.609901, E25.238966), placing talc tremolite mylonites and serpentinized peridotites over anatectic clinopyroxene bearing amphibolites in the metamorphic sole. The extent of partial melting reaches up to ~20% of the rock volume within these upper 5 m of the sole, with leuco-dioritic melt emanating from the thrusted contact. (b) Metacherts and metabasalts of the metamorphic sole (N37.573234, E25.237498), showing extreme deformation and intense isoclinal folding and ductile thrusting. (c) The Tsiknias Thrust with a 5 cm thick cataclasite zone, indicative of intense localized ductile and brittle deformation (N37.582611, E25.216552). Serpentinized peridotites of the ophiolite adjacent to amphibolite mylonites with a heavy brittle overprint, suggesting the thrust has a long deformation history. (d) High-temperature mylonitized amphibolites that have metagabbroic protoliths from east of Mount Tsiknias (N37.572140, E25.231410), with plagioclase porphyroclasts indicative of top-to-SW shearing. (e) Epidote amphibolites with centimeter-scale porphyroclasts of epidote, plagioclase, and actinolite, which possibly pseudomorph an earlier porphyroblast (N37.587169, E25.225783). The retrograde assemblage shows top-to-SW shearing, indicating syntectonic deformation during epidote-amphibolite to greenschist-facies conditions. (f) Intensely deformed metachert and pelagic metasediments within the Mirsini Unit, with mylonitization overprinted by clear brittle-ductile thrusts with centimeter-scale offsets indicative of top-to-SW movement (N37.629003, E25.161868). (g) Amphibolites of the Akrotiri Unit with intercalated metasediments with a strong steeply dipping foliation, with flattening strains of ~10:1, from near Tinos Town (N37.529464, E25.163928). (h) Recumbently folded and extremely deformed metaturbidites and distal oceanic metasediments and metavolcanics of the Mirsini Unit directly under the metamorphic sole. These rocks contain amphibole and garnet indicating upper-greenschist facies conditions with brittle-ductile thrusting overprinting blast-mylonite fabrics (N37.587198, E25.209995).

Tectonics

10.1029/2019TC005677

Table 1
Summary of the Major Tectonostratigraphic Units on Tinos Including the Major Rock Types, Protolith Age, Metamorphic Age, Deformation and Fabrics, P-T conditions experienced and tectonic interpretation

Summary Table of the Tectono-Stratigraphy on Tinos

Tectonostratigraphic unit	Tectonostratigraphic subunit	Rock types	U-Pb formation Age (Ma)	U-Pb Metamorphic Age (Ma)	Geochemistry	Deformation features and fabrics	Mineral assemblages	P-T conditions	Tectonic interpretation
Tsiknias ophiolite	Serpentinized peridotites	Serpentinized peridotites	—	—	—	Tsiknias Thrust at the base, out of sequence thrusts (Elias Thrust) overprinted by ductile normal sensed shearing (top-to-NE; S1; Livada Detachment) and high-angle faults. The Ophiolite is intruded by the Tinos Monzogranite, Leucogranite Sills and Dacite Dykes.	Sepentinized peridotite: Serp+Ant +Ol ± Cpx ± Opx + Mag ± Magnesite	—	SSZ ophiolite that formed at 161.9 Ma to the NE of Tinos and was intruded by EMORB/ BAB gabbros at ~144 Ma.
	Moho-transition zone	Serpentinized peridotites, gabbros and a plagiogranite	161.9 ± 2.8 (17-TL35 plagiogranite), 144.3 ± 5.6 (17-TL27 Gabbro)	—	SSZ plagiogranite and gabbro, with E-MORB/ BAB type Gabro		Gabbro: Pl + Cpx + Amp + Sph, plagiogranite: Pl + Qtz + Ep + ilm + Chl ± Bt ± Rt ± Sph ± Ms	—	
Metamorphic sole	Amphibolites	Amphibolites, leucodiorite melt sweats and veins	190 ± 10 (17TL-26 Amphibolite with leucodiorite melt vein)	74.0 ± 3.5 (17TL-26 Amphibolite with leucodiorite melt vein)	E-MORB-IAT mafic protolith	Tsiknias Thrust at the top. S1 planar fabric, S2a crenulation cleavage (with F1 folding), S2b top-to-SW shear fabrics and S-C′, S3 post-tectonic amphibole rims and titanite. L1 plunges ~10° toward NE defined by plagioclase rods, syntectonic and crosscutting melt veins close to Tsiknias Thrust. Cut by high angle normal faults and intruded by Tinos Monzogranite, Leucogranite Sills and Dacite Dykes.	Amp + Pl + ilm + Mag ± Rt ± Sph ± Cpx ± Ep ± Qtz	6–8.5 kbar, 650–850 °C	E-MORB ~190 Ma Oceanic crust that was subduced and metamorphosed under the Tsiknias Ophiolite at ~74 Ma. High-grade metamorphism and anatexis occurred coeval with top-to-SW shearing.
	Mirsini unit	Pelagic metasediments, metacherts, metaturbidites	—	—	—	S0 sedimentary layering, S1 planar fabric, S2a crenulation cleavage (with F1 folding), S2b top-to-SW shear fabrics and S-C′, S3 posttectonic radiating amphibole and euhedral garnets. Sequence affected by several minor thrusts and isiclinal folds (F1), and intruded by Tinos Monzogranite, Leucogranite sills and Dacite Dykes.	Grt + Qtz + Amp + Pl + ilm + Mag ± Rt ± Sph ± Chl ± Cpx ± Ep	5.5–8.5 kbar, 600–680 °C	Pelagic sediments laying ontop of oceanic crust that were underthrusted beneath the amphibolites in a 74 Ma subduction zone and metamorphosed.
	Akrotiri Unit	Amphibolites and metasediments	—	~67 Ma (K-Ar; Patzak et al., 1994)	—	Lineation plunge 70° to WSW and top-to-WSW shear fabrics	Amp + Pl + ilm + Mag ± Sph ± Ep ± Qtz	5–7 kbar, 550–700 °C (Patzak et al., 1994)	A tectonically downthrown slice of the metamorphic sole.
Tinos monzogranite pluton	—	Hb, Bt monzogranite	14.6 Ma	—	—	Intrudes the Tsiknias ophiolite and	Hb + Bt + Sph + Pl + Qtz	—	Calc-alkaline magmatism from

Table 1 *(continued)*

Summary Table of the Tectono-Stratigraphy on Tinos									
Tectonostratigraphic unit	Tectonostratigraphic subunit	Rock types	U-Pb formation Age (Ma)	U-Pb Metamorphic Age (Ma)	Geochemistry	Deformation features and fabrics	Mineral assemblages	P-T conditions	Tectonic interpretation
						Metamorphic Sole, intruded by leucogranites and relatively undeformed at Livada Bay			Hellenic Subduction Zone (Brichau et al., 2007).
Garnet leucogranites sills	—	Grt, Ms Leucogranite	~14 Ma	—	—	Intrudes Metamorphic Sole amphibolites, parallel to S2b fabric	Pl + Qtz + Grt + Ms	—	—
Cycladic blueschist unit	—	Meta-turbidite successions, meta-psammites, dolomitic marbles and mafic eclogites	Juarrsic (Andriessen, 1978)	53.1–51.1 (Lu-Hf Syros; Lagos et al., 2007), 44.9–46.9 (Lu-Hf Sifnos), 51.1-53.4 (U-Pb Tomaschek et al., 2003)	—	Prograde top-to-SW fabrics, top-to-NE shearing fabrics (exhumation related), Isoclinal folds overprinted by top-to-NE greenschist facies shearing on the Tinos Shear Zone (Further details will be presented in a future paper.)	(This will be presented in a future paper.)	22–19 kbar, 550 °C (Syros; Laurent et al., 2018), 15–18 kbar, 490–500 °C (Parra et al., 2002)	Subduction of the leading edge of the Cycladic Continental Margin toward the NE at ~52–46 Ma followed by exhumation.

performed using THERMOCALC v3.40i and data set ds-62 (Powell & Holland, 1988; Holland & Powell, 2011), to provide further constraints on peak metamorphic conditions and to gain insight into the phase relations. This combined approach was performed on high-grade amphibolites (TLT10 and 17TL25), as well as the underlying metasediments 50–150 m structurally below (TLT1, TLT13, and TLT15). For a full description of analytical procedures and overview of phase equilibria modeling, please consult the supporting information Text S1.

3.4. Whole-Rock Geochemistry Methods

A suite of fresh amphibolite, gabbro, and plagiogranite samples were collected to investigate whole-rock geochemistry to place constraints on the tectonic setting the ophiolitic rocks formed in. Samples were prepared using techniques described in the supporting information and were analyzed by X-ray fluorescence (XRF) at the Department of Earth and Environment, Franklin and Marshall College, Lancaster, Pennsylvania, USA, using the procedures described in the supporting information. Trace elements were collected on a Perkin Elmer 6100DRC Quadrupole inductively coupled plasma mass spectrometer (ICP-MS) with a dynamic reaction cell at the Department of Earth Sciences, University of Oxford. Reported precision is better than ±5% (2 S.D., standard deviation). The new geochemical data (n = 10) are combined with those presented by Stouraiti et al. (2017) and Katzir et al. (1996; total n = 53).

3.5. Geochronology Methods

To determine the age of ophiolite formation and metamorphism, U–Pb zircon dating of a plagiogranite, gabbro, and amphibolite melt vein was carried out at the Geochronology and Tracers Facility at the British Geological Survey (Nottingham, UK). Samples were crushed using standard techniques (Jaw-crushing, disk milling, sieving, Rogers table, heavy liquids, and Frantz isodynamic magnetic separation). Zircon grains from each sample were then picked under alcohol, mounted in 1-inch epoxy resin mounts and polished until all grains were exposed. These were imaged by cathodoluminescence to distinguish zircon growth zoning. Additional analyses of the amphibolite of the metamorphic sole (17TL26) were conducted on zircon grains mounted on double-sided tape, to better determine the age of the thin outer rims. All U–Pb analyses were performed on a Nu Attom single collector inductively coupled plasma mass spectrometer (SC-ICP-MS) coupled to a New Wave Research 193UC excimer laser ablation system fitted with a TV2 cell. Standard-sample bracketing was employed with the full setup and protocols described previously in Roberts et al. (2016) and full analytical data provided in the supporting information. All data and ages are shown and quoted at 2σ, are $^{206}Pb/^{238}U$ ages, and follow uncertainty propagation guidelines of Horstwood et al. (2016). The data are presented as common-Pb weighted mean plots and Tera-Wasserburg plots using a regression through the data anchored at a $^{207}Pb/^{206}Pb$ value of 0.84 ± 0.02 (based on Stacey & Kramers, 1975). Lu–Hf garnet geochronology was undertaken on one metachert sample (TLT13), but unfortunately only a single garnet fraction could be collected for a two-point isochron and therefore the results need to be treated with caution. For a complete review of methods and results consult Text S1.

4. Field Relations of the Tsiknias Ophiolite

Ultramafic and gabbroic rocks crop out as part of the Upper Unit (Avigad & Garfunkel, 1989, 1991; Katzir et al., 1996) and represent an incomplete ophiolite sequence, herein referred to as the Tsiknias Ophiolite, named after Mount Tsiknias, the highest mountain on Tinos. The Tsiknias Ophiolite can be found at six exposures across Tinos, but the most complete are preserved as klippe on Mount Tsiknias, NE of Kolimpithra Bay and NE of Marlas village (Figure 2). Upper crustal lithologies such as sheeted dykes and basalts are missing and were presumably eroded. The ophiolite is structurally repeated by out-of-sequence thrusts and cut by late normal faults. A newly discovered metamorphic sole is exposed along the base of the Mount Tsiknias section (see below). The ophiolite and sole have been folded by kilometer-scale gentle open upright folds with NNE–SSW trending axes after obduction and metamorphism (see Figure 2, stereonets). This has refolded the metamorphic and ophiolitic stratigraphy on Mount Tsiknias into a gentle NE plunging synform. The Upper Unit and Tinos Shear Zone have been domed about a NW–SE axis that runs down the center of the island and defines the island's elongate shape. Below, we give a systematic description of the ophiolite structure and key tectonostratigraphic units from structurally high to low.

4.1. Mantle and Gabbro—Moho Transition Zone

Massive serpentinites form the prominent slopes of Mount Tsiknias, NE of Kolimpithra Bay and the mountain to the NE of Marlas in NW Tinos (Figure 2). There are two distinct horizons of serpentinized peridotites, both representing the mantle sequence of the Tsiknias Ophiolite. The first horizon occurs at the base of the ophiolite, directly above the metamorphic sole (see below and Figure 6) and is highly deformed with finely crystalline antigorite that displays NE–SW stretching lineations similar to the "Banded ultramafic unit" along the base of the Semail Ophiolite, Oman (Searle & Cox, 2002). The degree of deformation decreases structurally up-section, where primary harzburgite and dunite precursors can be found. Along the base of the ophiolite, notably at Livada Bay (Figure 2), some localized veins display transformation of primary olivine and minor pyroxene to antigorite, talc, and asbestos group minerals (Figure 6a). We interpret these to represent serpentinized dunites that formed part of a depleted mantle sequence underlying oceanic crust and estimate that there is approximate 100–400 m structural thickness of serpentinized mantle exposed today at the base of the ophiolite, beneath the first appearance of gabbro. The exposed upper levels of Mount Tsiknias, which overlay the serpentinites, represent a cross-section through the Moho Transition Zone and cumulate gabbro sequence, similar to the Moho Transition Zone of the Semail Ophiolite (Searle et al., 2015; Ambrose & Searle, 2019). The Moho Transition Zone is an ~150 m thick section of alternating meter-scale zones of foliated and tectonized hornblende-rich gabbros (Figure 5b) marked by the appearance of white saussurite (microcrystalline plagioclase + epidote) and almost completely serpentinized harzburgites, wehrlites, and pyroxenites (Figures 1a and 1b). A large plagiogranite sill intrudes this sequence (see Figure 7) and is aligned with the gabbros and has a strong internal NE–SW trending fabric. Gabbros form sills which vary from a few meters thick to over 50 m thick and are semicontinuous along strike. The gabbros show leucocratic and mafic varieties, and locally display magmatic fabrics (S_0) that are overprinted by a subhorizontal solid-state foliation (S_1), associated with top-to-NE kinematics, which maybe related to the Livada Detachment (see below).

Another horizon of almost completely serpentinized wehrlites and harzburgites, representing depleted mantle, overlay the Moho Transition Zone gabbros due to an out-of-sequence thrust (Elias Thrust, dashed line in Figures 2 and 3), that structurally repeats the ophiolite sequence. This thrust must have been associated with the late stages of the ophiolite emplacement process. Similar out-of-sequence thrusts structurally repeat parts of the metamorphic sole at Livada Bay and the western part of Mount Tsiknias (Figures 2 and 4). On the NW flank of Mount Tsiknias, close to the Tinos granite, many of the primary ophiolitic assemblages have been recrystallized with hornfels textures due to contact metamorphism associated with the granite intrusion (see Figure 8c; actinolite rims on hornblende). Miocene normal faulting further disrupts the sequence, creating uplifted and domino-rotated fault-blocks bounded by brittle faults that crosscut the Livada Detachment that truncates the ophiolite (Figure 5a). In contrast, ductile shearing on the Livada Detachment may have produced the top-to-NE (S_1) S–C fabrics throughout some of the gabbro horizons within the ophiolite described above.

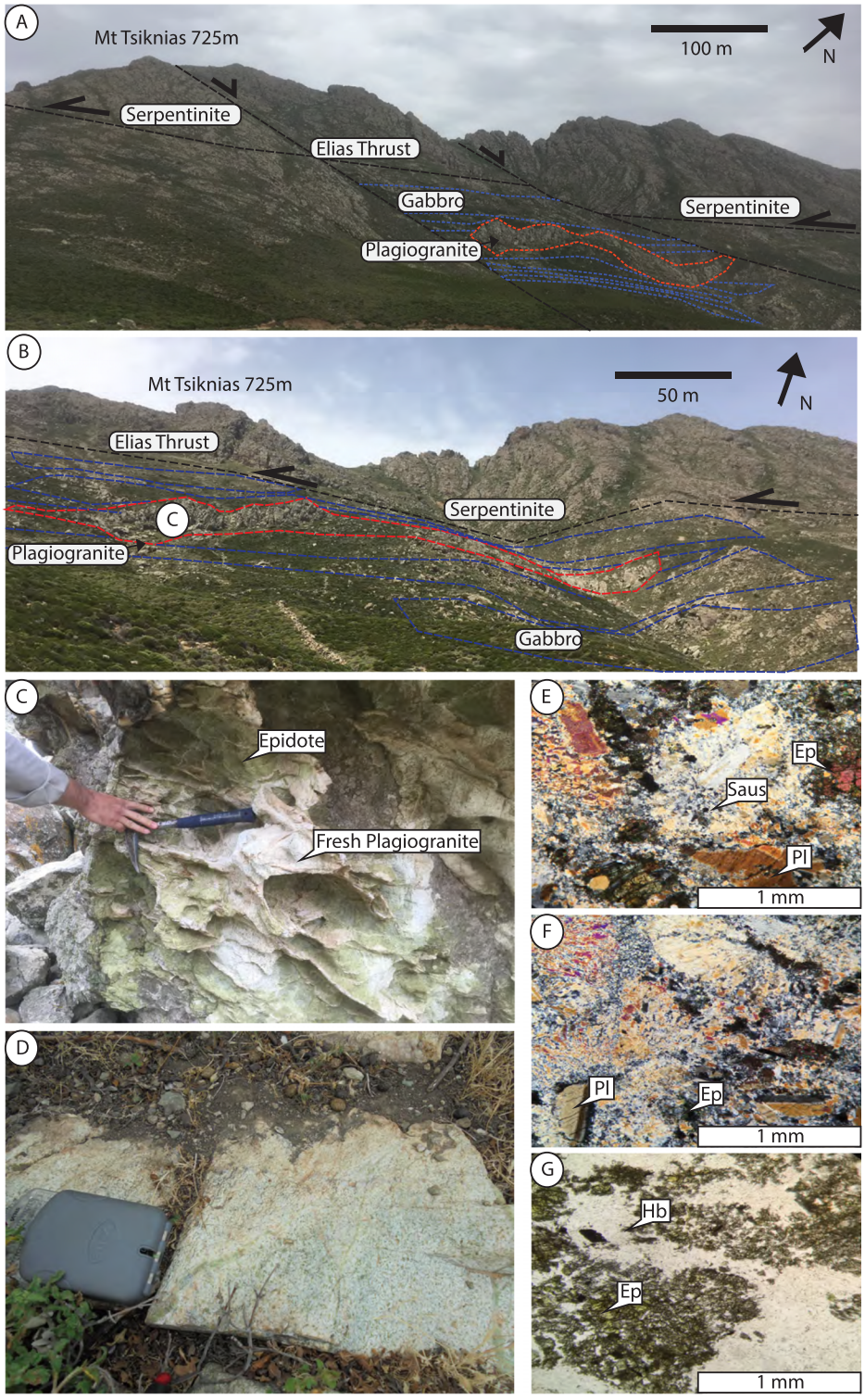

Figure 7. Representative photographs and photomicrographs of the plagiogranite body (N37.582399, E25.232871) intruding within the Moho Transition Zone on the eastern flank of Mount Tsiknias, it weathers proud against the surrounding highly serpentinized ultramafics and weathered gabbros (a and b). (c) Large degrees of epidotization around the margins of the granite. Above it lies a large continuous body of ultramafics that have been structurally repeated due to the SW verging out of sequence thrust, the Elias Thrust (a and b). (e and f) Somewhat fresh matrix of partially sausitized plagioclase graphitic groundmass with fresh phenocrysts of plagioclase with partial alignment of the phenocrysts defining a subhorizontal magmatic fabric. Secondary epidote occurs in clusters nucleating of more sausertized zones. (g) Plane polarised light (PPL) photomicrograph of plagiogranite 17TL35 showing clots of euhedral epidote and minor amphibole grains in a plagioclase groundmass.

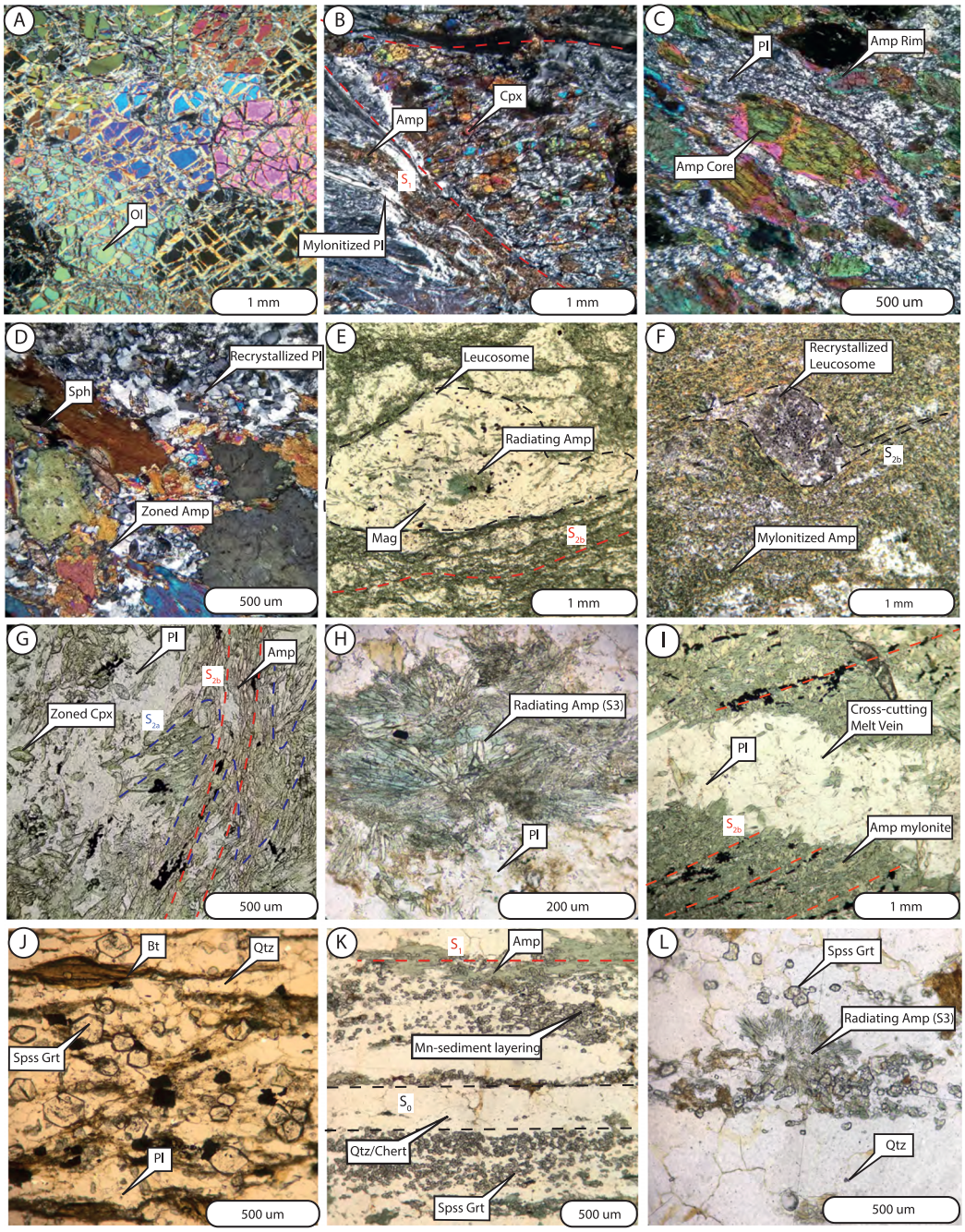

Figure 8. A representative selection of photomicrographs from the Tsiknias Ophiolite, metamorphic sole and Mirsini Unit. (a) 17TL-24, serpentinized dunite from a dunite channel within the base of the ophiolite, with partially serpentinized olivine with conchoidal fracture. (b) TLT42, sheared and mylonitized gabbro within the moho-transition zone. (c) TLT32, amphibolite from the metamorphic sole with overgrowths of actinolite amphibole and subgrain rotation in plagioclase. (d) TLT3, amphibolite from the metamorphic sole, with titanite and large-zoned amphiboles and extensive plagioclase dynamic recrystallization textures. (e) 17TL-25, anatectic amphibolite from the uppermost 5-m melt zone, with leucosomes of dominantly plagioclase and radiating hornblende, with a high abundance of magnetite. This cross cuts the mylonite amphibole fabric. (f) 17TL-25, recrystallized leucosome, with top-to-SW asymmetry, indicating shearing deformation coeval with melt crystallization. (g) TLT41 amphibolite textures with a strong S_2 fabric, with some radiating amphiboles (S_3), with some zoned metamorphic augite. (h) TLT41 radiating amphibole textures indicative of high temperatures outlasting deformation, with some degrees of static recrystallization in plagioclase. (i) TLT49, migmatized amphibolite, with a sharp boundary marked by crosscutting leuco-dioritic leucosome, that definitively postdates S_{2b} mylonitization. (j) TLT15, metasediment from the Mirsini Unit with macroscale mylonite S–C fabrics, that are overgrown by small posttectonic spessartine rich garnets. (k) TLT13, centimeter-scale layers of metachert and Mn-rich sediment, that have been metamorphosed to amphibolite grade. Mn rich layers grown spessartine garnet in abundance, that cross cut the previous mylonitization. (l) TLT13, showing intergrown garnet and radiating amphibole S_3, that are posttectonic with respect to deformation, indicative of high temperatures outlasting deformation.

4.2. Plagiogranites

A 50 m thick and 300 m long plagiogranite sill (Figure 7) intrudes the Moho Transition Zone on the eastern flank of Mount Tsiknias (N37.580458, E25.231727) and has intrusive contacts with the host gabbros and serpentinities. Along the margins of the plagiogranite, strong chlorite and epidote alteration represent blackwall reaction textures (alteration zones) with the host peridotites and gabbros, suggesting the plagiogranites intruded while the host rocks were still at high temperature. The plagiogranite is highly saussseritized and contains large euhedral epidotes, which point to a magmatic origin, and secondary epidote that forms along its surfaces and fractures (see Figure 7c).

4.3. Tsiknias Thrust

At the base of the Tsiknias Ophiolite, a 1–2 m wide shear zone juxtaposes banded and highly foliatated serpentinites and peridotites in the hanging wall against dark and locally partially melted amphibolites in the footwall (see Figures 5c and 6a–6d). These structural relationships have been previously described by Katzir et al. (1996) and are best exposed in Livada Bay (N37.609704, E25.238715), near an intrusive contact between the Tinos I-Type granite and amphibolites (Figure 4b). Several lines of evidence suggest this shear zone represents the basal thrust of an intact ophiolite sequence (herein referred to as the Tsiknias Thrust). The Tsiknias Thrust is continuous along strike for >5 km and is well exposed at several outcrops on the eastern and western flanks of Mount Tsiknias, NE of Kolimpithra Bay and NE of Marlas village (Figure 2). The core of the shear zone comprises microcrystalline talc-tremolite tectonites that display ultramylonite textures entrained in a microcrystalline cemented serpentinized gouge. An anastomosing and branching network of glassy magnesite and microcrystalline plagioclase veins crosscut the shear zone and emanate into the overlying serpentinites (Figure 6a). Clasts and angular fragments of serpentinized dunites (from the overlying peridoties) and amphibolites up to 50 cm wide occur within the gouge. The grain size within the underlying amphibolites decreases upward toward the shear zone, and the NE–SW lineation defined by recrystallized plagioclase rods in the amphibolites (Figure 5c and see below) strengthens toward the shear zone. Top-to-SW kinematic indicators such as stair stepping around plagioclase and epidote-rich enclaves consistently occur throughout the underlying amphibolites (Figure 6e), the opposite to the top-to-NE shear sense associated with normal sensed motion on the NCDS (see Figures 5 and 6). These features suggest that this structure represents a SW verging thrust that was responsible for emplacing the Tsiknias Ophiolite onto the underlying amphibolites. This thrust plunges toward the NE and preserves the Tsiknias Ophiolite as a klippe along the entire mountainside of Mount Tsiknias (Figures 2–4).

4.4. Metamorphic Sole:

A ~150 m thick series of high-grade foliated amphibolites (meta-basalts and gabbros) crop out underlying the base of the Tsiknias Ophiolite (Figures 4–6). These high-temperature metamorphic rocks are juxtaposed against highly serpentinized foliated and sheared peridotites in the hangingwall by the 1–2 m wide shear zone described above (Tsiknias Thrust). The amphibolites and underlying metasediments show many features consistent with what could be described as a metamorphic sole that formed in a subophiolitic subduction zone (Casey & Dewey, 1984). An extremely steep and inverted apparent metamorphic field gradient is observed below the Tsiknias Trust over a few hundred meters. Within 50 m below the Tsiknias Thrust, the amphibolites are highly strained S–L tectonites and display a clear NE–SW trending lineation (L_1) defined by elongated plagioclase rods that show an elongation ratio of >4:1 and plunge ~10° toward the NE (see steronet in Figure 2). Three major fabrics can be distinguished within the amphibolites. The S_0 fabric presumably represented the primary igneous fabric and has almost been completely destroyed by subsequent deformation and recrystallization. The S_1 fabric is planar and is preserved in dilatational strain sites, and is defined by compositional banding of hornblend rich amphiboles, plagioclase, rutile, and ilmentite. This fabric has been deformed into a spaced crenulation cleavage (S_{2a}) with microlithons characterized by recrystallized amphibole, plagioclase rutile, ilmenite titanite, and magnetite that show interlocking herringbone textures. The S_{2a} fabric is preserved in amphibole rich domains and is associated with macroscale and microscale isoclinal folding (F_1). However, it is commonly overprinted by the strong S_{2b} top-to-SW shear foliation, and is confined to depths >5 m below the Tsiknias Thrust, which have experienced lower intensities of ductile shearing shearing. S_{2b} is the dominant planar fabric in the amphibolites and underlying pelagic metasediments of the Mirsini Unit at outcrop and thin section scale. S_{2b} utilizes the S_{2a} cleavage domains and has dynamically recrystallized much of the matrix amphibole into uniformly small prismatic grains <50 μm in

diameter and is associated with S–C′ fabrics that consistently show top-to-SW shear. Near the contact with the Tsiknias Thrust, the S_{2b} fabric is so strong there is no evidence for the earlier microstructures; however, the intensity of the S_{2b} shear fabric decreases downward away from the Tsiknias Thrust over tens of meters. Within the uppermost 2 m of the amphibolites, directly below the Tsiknias Thrust, high-temperature assemblages, including clinopyroxene- and hornblende-bearing amphibolites are deformed with the S_{2b} foliation. Evidence for localized anatexis in the top few meters of the amphibolites is marked by the development of leucosomes and partial melt veins that appear to emanate from the Tsiknias Thrust (Figures 6a and 6b). Leucosomes and melt veins are composed of plagioclase with <5% hornblende, <3% quartz, and minor magnetite, suggesting a leuco-diorite composition and are either aligned with, or cross cut, the S_{2b} mylonite fabrics (see Figures 5, 6, and 8), suggesting partial melting occurred only within a few meters of the Tsiknias Thrust and was coeval with and shortly postdated ductile top-to-SW shearing. These features suggest that high-grade metamorphism was syntectonic with S_{2b}, which was associated with top-to-SW mylonitization induced due to ductile shearing under the Tsiknias Thrust.

The metamorphic field gradient decreases over <100 m down structural section to epidote-amphibolites (Figures 5–10), which consists of the assemblage: actinolite + albite + epidote + sphene ± chlorite ± hornblende ± clinopyroxene ± rodingitized garnet (e.g., Figures 6e and 10h). A lithological zonation is also preserved, grading from metabasalts and gabbros which form the uppermost and highest grade amphibolites, down to distal oceanic metasediments and cherts that display millimeter-sized Mn-rich layers that would have represented primary sedimentary layering of Mn-rich clays (S_0), which are now characterized by <30-μm diameter spessartine-rich garnet (e.g., Figures 8j–8l). On the northwestern side of Mount Tsiknias, both the Tinos I-type granite and leucogranite sills intrude into the sole. This has highly altered the S_1 and S_2 microstructures and mineral assemblages and overprinted them with hornfels textures (S_3) including <15-μm rims of actinolite and diopside on cores of higher temperature brown hornblende (see Figure 8c)(Bröcker & Franz, 2000).

4.5. Mirsini Unit

The Mirsini Unit represents the structurally deepest part of the metamorphic sole below the distinctive high-temperature amphibolites. The unit is exposed along the base of Mount Tsiknias (Figures 4–6) representing a structural thickness of up to 200 m. The unit is dominantly composed of distal oceanic metasediments, interlayered with metavolcanics, recrystallized quartzites and cherts, which have been metamorphosed to lower to middle amphibolite facies. Toward the base of this unit, metamorphosed turbidites suggest that the deepest levels of the Mirsini Unit were deposited in a distal continental slope environment. Deformation is highly penetrative throughout this unit, with evidence for ductile shearing and folding over a range of scales (Figures 4–6). At the top of the Mirsini Unit, the Mirsini Thrust is associated with top to SW kinematics and is interpreted to be responsible for overthrusting the amphibolite-facies metabasalts to produce an inverted stratigraphy. Contrastingly, the base of the Mirsini Unit is truncated by the Tinos Shear Zone, which is associated with top to NE kinematics. This late structure separates the Mirsini Unit, metamorphic sole, and Tsiknias Ophiolite (Upper Unit) from the underlying Cycladic Blueschists (Lower Unit).

4.6. Akrotiri Unit

The Akrotiri Unit, exposed to the south of Tinos Town, is characterized by steeply dipping (70°/85°) amphibolites and intercalated metasediments associated with a lineations plunging ~70° toward the WSW and associated with top-to-WSW S–C′ shear fabrics (Figure 6g). It has experienced amphibolite-facies metamorphic conditions (Patzak et al., 1994) and has previously been interpreted as an allochthonous unit. However, these rocks have many similarities with the amphibolites exposed in the north of Tinos and lie at a similar structural level. Although there is little context for this unit with the surrounding geology, one interpretation is that it represents a downthrown slice of the metamorphic sole (Figure 3). Movement on this steep shear zone must have occurred after high-pressure metamorphism of the Lower Unit as it truncates the high-pressure metamorphic foliation. Metagabbros and serpentinite outcrop to the west of Tinos Town, structurally along strike with this unit (Figure 2), possibly supporting this interpretation.

4.7. Livada Detachment and Brittle Normal Faults

The Tsiknias Ophiolite and metamorphic sole has been cross cut by a series of normal faults associated with the NCDS (Jolivet et al., 2010). The Livada Detachment, a low-angle normal fault (Jolivet et al., 2010), is

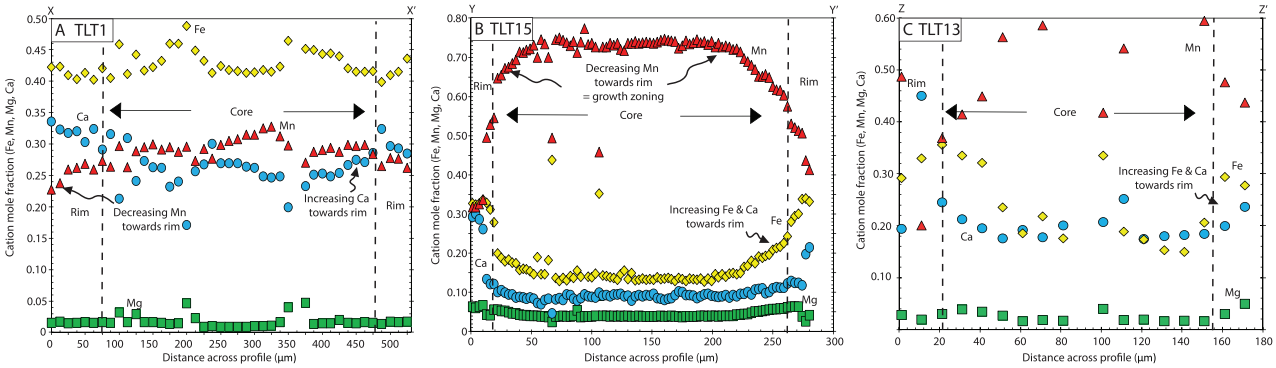

Figure 9. Line profiles of Mirsini Unit garnets showing cation mole fractions almandine, grossular, pyrope, and spessartine: (a) TLT1, (b) TLT15, (c) TLT13.

poorly exposed throughout the section, however, could be associated with ductile top-to-NE shear fabrics that cross cut several gabbro horizons and results in extreme grain size reduction and S–C fabrics (see above and supporting information). At Livada Bay, a series of steep, domino-style normal faults cross cut and offset the metamorphic sole and leucogranitic sills that contain garnet and muscovite (Figure 5a). These sills clearly predate many of the brittle normal faults, but in some occurrences show lobate margins and appear to propagate along the fault planes. Brittle normal faulting must be related to regional Aegean extension and immediately postdates sill intrusion. These normal faults record the first definitive evidence for extension in the region and presumably represent the brittle-ductile transition at the time of granite intrusion (~14.6 Ma; Brichau et al., 2007; Lamont, 2018).

4.8. Tinos Shear Zone

The Tinos Shear Zone is a normal sense greenschist-facies structure separating the Upper Unit from the underlying high-pressure rocks of the Cycladic Blueschist Unit (Jolivet et al., 2010). It is associated with top-to-NE kinematics and is domed around the island about an ENE–WSW axis. The gentle NNE dip of this structure on the island's north coast is responsible for the exposure of the Upper Unit as klippe on structurally high topography such as Mount Tsiknias. This shear zone is crosscut by the Tinos I-type granite, indicating it was active prior to intrusion (ca. 14.6 Ma; Brichau et al., 2007; Lamont, 2018) and has subsequently been folded. It is unclear if this structure is related to crustal extension, as normal sensed shear fabrics only record the relative ductile exhumation of material and cannot be used to characterize a specific tectonic regime (Searle & Lamont, 2019).

5. Petrography

5.1. Tsiknias Ophiolite Plagiogranite

The large plagiogranite on the eastern flank of Mount Tsiknias is characterized by dominantly plagioclase, quartz, muscovite, and epidote with minor rutile, chlorite, ilmenite, and sphene and <1% hornblende. Epidote forms stubby phenocrysts that display ophitic textures. Epidotes also show embayments when in contact with the quartzo-feldspathic matrix, suggesting they predate the leucocratic matrix. Epidotes also display allanite-rich cores with pristicine content (Fe^{3+}/Fe_{total}) varying between 0.962 and 0.995 from core to rim. Together these features suggest that epidote has a magmatic origin (Zen & Hammarstrom, 1984; Schmidt & Poli, 2004). In the crystallization sequence of a plagiogranite, epidote commonly appears in tonalite after hornblende but before or contemporaneous with biotite (Schmidt & Poli, 2004), indicating it is a relatively primary phase. Chlorite occurs as a secondary minor phase along fractures and as breakdown of the primary epidote and possibly relict biotite. Plagioclase is commonly saussurtized but fresh grains are of albite in composition with *X*Ca consistently <0.01.

5.2. Ophiolite Gabbros

Most of the gabbros comprise >50% amphibole and dominantly plagioclase with <5% clinopyroxene, ilmenite, and sphene. Amphiboles are zoned and coarse grained with compositions varying between hornblende to actinolite. Plagioclase shows a range of compositions from anorthite to pure albite, probably due to

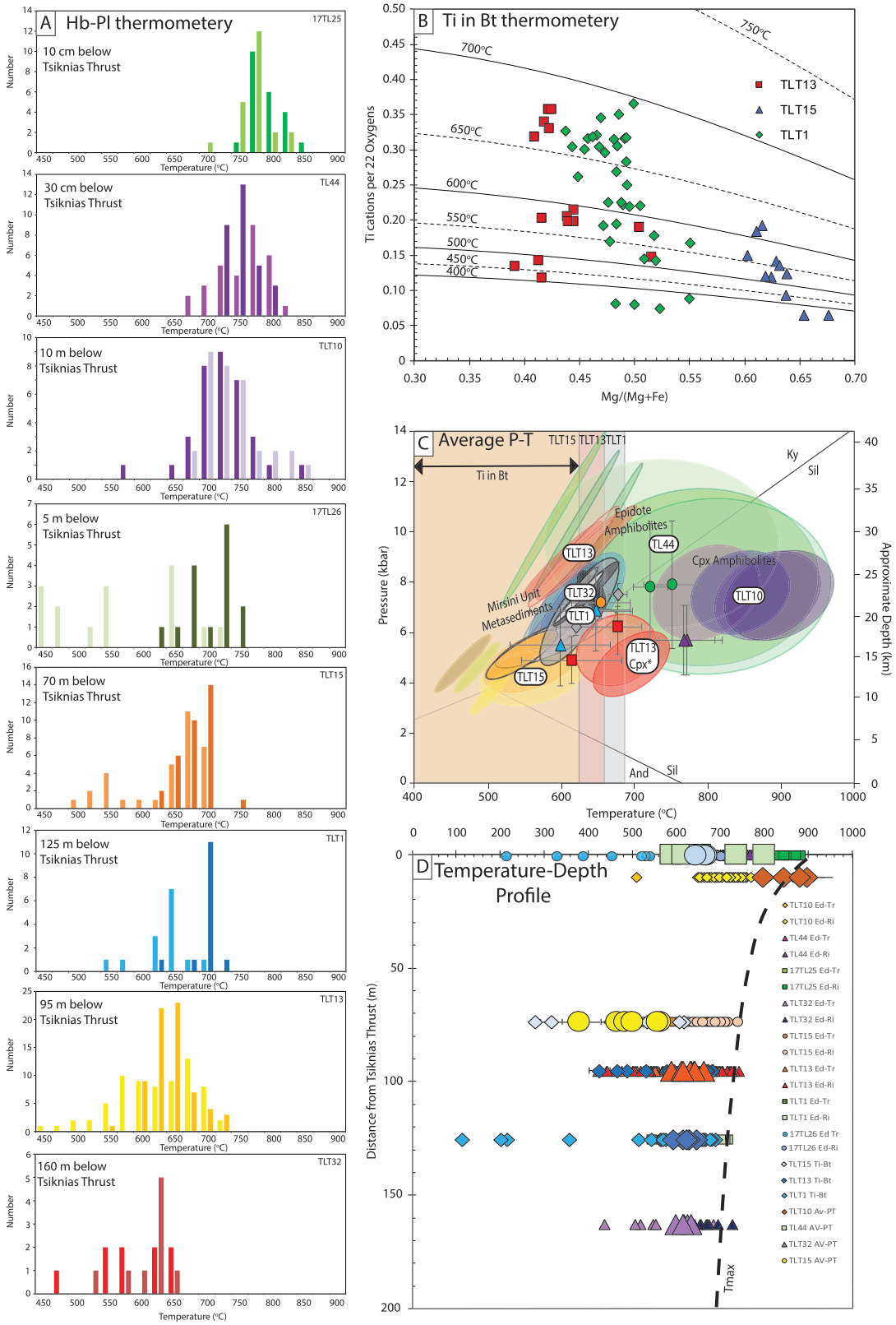

Figure 10. Summary of thermobarometry results of the metamorphic sole: (a) Hb-Pl temperature distributions across samples arranged in order of structural depth, (b) Ti in Bt thermometry for metasediments from the Mirsini Unit, (c) THERMOCALC Average *P-T* results with conventional thermobarometry. (d) Temperature vs depth beneath the Tsiknias Thrust profile for various thermometers used in the study, dashed line indicates approximate trend of peak metamorphic conditions.

retrogression and saussuritization. Fresh plagioclase is characterized by *X*Ca = 0.62–0.42, although most of the grains have been recrystallized and exhibit albite compositions with *X*Na = 0.90–0.99. Clinopyroxene is dominantly augite-diopside in composition but commonly breaks down to amphibole, which sometimes forms actinolite rims. Primitive amphiboles are hornblende to paragasite in composition and display eccentric zoning with actinolite rims, with Ti varying from 0.10–0.01 per formula unit (p.f.u), K between 0.2 and 0.02 p.f.u. Along the interpreted Moho Transition zone, gabbros are intensely foliated (S_1) with top-to-NE kinematics. The gabbros show a complete spectrum of deformation textures in plagioclase from magmatic fabrics to solid state dynamic recrystallization and subgrain rotation, indicating deformation and top-to-NE shearing occurred over a wide temperature range during and after crystallization.

5.3. Metamorphic Sole Amphibolites

High-grade amphibolites (samples TL44, 17TL25, 17TL26, TLT10, and TLT32) throughout the sole are composed of dominantly amphibole + plagioclase, with titanite and ilmenite, and contain enclaves of augitic clinopyroxene + amphibole, rare chromium spinel, and have secondary chlorite and epidote. Amphiboles display a range of chemistry (presented in the supporting information), and their composition representing peak metamorphic conditions is mainly pargasite to ferro-pargasite. Whereas fine-grained actinolite, which is deformed with the S_{2b} mylonite fabric, represents retrograde metamorphic compositions. Amphiboles are characterized by Ti between 0.18–0.03 and K between 0.11–0.03 p.f.u, with the most elevated Ti and K content associated with the most primitive high-temperature grains. These grains also exhibit the highest values of XAl in the M_2 site = 0.35–0.28, suggesting they also formed at the highest pressures. Plagioclase is finely crystalline within the S_{2b} mylonite fabric and is affected by dynamic recrystallization causing undulose extinction and is in low abundance, but comprises >90% of the leucosomes and melt veins, which exhibit a small range of *X*Ca = 0.32–0.43. However, >5 m below the Tsiknias Thrust, plagioclase forms rods up to 5 cm long that define the NE–SW trending lineation.

Leucocratic melt appears to emanate from the Tsiknias Thrust and the amphibolites from directly below into the underlying rocks and displays both synkinematic and postkinematic relationships with the S_{2b} top-to-SW ductile shearing fabrics (Figures 5, 6, and 8). Leucocratic veins clearly crosscut the S_{2b} mylonite fabrics and are composed of finely crystalline plagioclase with minor magnetite and hematite. Although many of the veins do not display microlite features (usually interpreted to indicate rapid quenching of melt; e.g., Del Gaudio et al., 1993), clear injection textures occur at the vein margins, including rip clasts of host amphibole (see Figure 8). Many of the melt veins have a preferential orientation down toward the SW; subparallel with the S_{2b} C′ shear bands, which have been demonstrated to represent melt crystallization coeval with top-to-SW ductile shearing (Kohlstedt & Holtzman, 2009). In numerous samples, crosscutting melt veins display dynamic recrystallization of plagioclase, whereas in situ leucosomes have augen geometries and are affected by consistent top-to-SW asymmetry, and therefore may represent previously boudinaged and deformed melt veins. Both these features are internally deformed in a ductile manner, indicating that deformation occurred at >550 °C (Rosenberg & Stünitz, 2003; Figures 8e, 8f, and 8i). Brittle deformation is superimposed on the amphibolite mylonite, and these fractures possibly influenced the migration of melt along distinct linear geometries, which have also been subsequently deformed in a ductile fashion upon crystallization.

The observation that melt features and veins are both undeformed in regions near the contact (i.e., most recent melting) and highly deformed and boudinaged in more distal regions a few centimeters to few meters away from the Tsiknias Thrust (older melting), suggests that anatexis occurred as a punctuated and episodic process. In contrast, ongoing ductile high-temperature creep was the likely dominant mode of deformation between melt episodes. The preservation of undeformed melt veins near the Tsiknias Thrust indicates that deformation within the sole propagated to deeper structural levels as the sole was heated and metamorphosed. Epidotization and secondary mineralization suggest that water-saturated conditions persisted during retrogression and implies that the dominant melting reaction was water-saturated melting of amphibolite, characteristically occurring at temperatures above 680 °C, with a negative *P*–*T* slope (e.g., Palin et al., 2016).

5.4. Mirsini Unit Metasediments

Pelagic metasediments (samples TLT1, TLT13, and TLT15) from the Mirsini Unit display a variety of protoliths including metaturbidites, volcanic sediments, and metacherts with significant Mn enrichment. All

samples are bidomanial preserving their S_0 primary sedimentary layering defined by quartz-rich domains (chert) separated from muddier domains defined by horizons of biotite, amphibole, sometimes Cpx, and small (10–350 μm) spessartine-rich garnets. On a thin section scale, the S_1 fabric is defined by preferred orientation of micas and recrystallization of quartz, subparallel to S_0, and is refolded at outcrop scale into isoclinal folds crenulation cleavages (S_{2a}). Top-to-SW shear fabric (S_{2b}) forms parallel along the cleavage domains to causing preferential alignment of matrix biotite and amphibole; however, in some low-strain domains they grow orthogonal to and crosscut the S_{2b} fabric and display dessucate textures (S_3; equigranular, interlocking, randonly orientated grains).

Small garnet crystals also crosscut the S_{2b} fabric, are inclusion free, and show straight faces suggesting garnets are posttectonic. The large abundance of small garnet crystals suggest that it may have been kinetically favorable to nucleate lots of grains upon overstepping the garnet-producing reaction (Waters & Lovegrove, 2002). This has been shown to be associated with either a rapid heating rate, fast reaction kinetics, or large reaction overstep. The tight crystal size distribution suggest that it was probably a combination of these factors, although a rapid heating rate is likely. Garnet line profiles for samples TLT1, TLT13, and TLT15 (Figure 9) reveal chemical zonation in garnet. Spessartine (XMn) content is >30% and is almost homogeneous across the garnet cores followed by a sharp decrease in the outer rims in all samples, suggesting a single stage of garnet growth. Similar albeit inverse patterns emerge in the grossular (XCa) and almandine although pyrope increases only slightly from core to rim. TLT1 shows slight zoning with spessartine content decreasing from 0.34 to 0.23 from core to rim, whereas grossular increases from 0.24–0.34 and pyrope remains flat. Sample TLT15 is characterized by extreme spessartine content in the core that decreases to 0.30 on the rim, whereas grossular and almandine increase to 0.32 and 0.33 at 0.06–0.07 pyrope. Garnets in TLT13 display similar patterns with high spessartine cores, with outer rims with similar abundances of almandine, grossular, and spessartine, at ~0.06 pyrope. These features suggest that all Mn was consumed by garnet during prograde metamorphism, whereas the last phase of garnet growth associated with the outermost rims had less available Mn. Matrix amphibolies range from actinolite to hornblende in composition (see supporting information), with Ti between 0.08 and 0.003 p.f.u. Biotites have XMg values ranging between 0.39 and 0.67 and Ti between 0.06 and 0.36, suggesting they grew over a range of pressure and temperature.

6. Pressures and Temperatures of Metamorphism

6.1. Thermobarometry

All thermometers consistently demonstrate that peak metamorphic temperatures span from ~600 °C (e.g., TLT15) to >850 °C (TLT10) across the current exposure of the metamorphic sole and specifically increase by ~200 °C, over just ~150 m directly below the Tsiknias Thrust. (Figures 5 and 10). The hornblende-plagioclase thermometer (Holland & Blundy, 1994) was used in all samples and relies upon two independent reactions, involving the Ca exchange between amphibole and plagioclase. Because this thermometer exhibits a very small dT/dP ~ 2–4 °C/kbar, pressure does not control the result significantly. Thus, a reference pressure of 8.5 kbar was chosen for final calculations based on Av-PT-derived average pressure results (see below), yielding temperatures ranging between 910 and 510 °C (Ca underflow) and 890–530 °C (no Ca underflow). Although there is a wide spectrum of amphibole compositions in each sample owing to variable degrees of retrogression, (see supporting information) the peak temperature distribution determined by this method systematically reveals a decrease from ~850 °C in samples TL44 and 17TL25 (within 1 m of the Tsiknias Thrust) to ~620 °C in sample TLT32 (150 m below the Tsiknias Thrust), with the largest temperature decrease directly beneath the Tsiknias Thrust. The Grt–Cpx thermometer was used exclusively for sample TLT13 and constrains the temperature to 608 ± 39 °C using the calibration of Powell, 1985 and 745 ± 52 °C using the calibration of Ravna (2000). The Ti in biotite thermometer was used in Mirsini samples TLT1, TLT13, and TLT15 and shows a range of maximum temperatures between samples from ~692–617 °C (TLT1–TLT15), with a reported uncertainty of ±24 °C (Henry et al., 2005) over ~50-m depth interval. The Al-in-amphibole barometer reveals a range of pressures; however, no amphibole exceeds 8.8 kbar across all samples and, therefore, provides a maximum estimate for the peak pressure of metamorphism.

Average *P–T* calculations were performed for a range of water activities from 0.7–1.0, and fluid-absent conditions and the results are plotted in Figure 10 and Table 2 with activities of solid-solution end members calculated using AX (Holland, 2009; last accessed August 2018). The results show that peak metamorphic

Tectonics

10.1029/2019TC005677

Table 2
Metamorphic Sole Thermobarometry Results

Tsiknias sole thermobarometry results				Thermocalc average *P-T*							Ti in Bt
Sample	Unit	GPS Location	Description	Endmembers	Notes	Temperature (°C)	S.D (T)	Pressure (kbar)	S.D. (P)	Corr	Temp range (°C)
TLT1	Mirsini	N37.58585 E25.21225	Metasediment/ Metavolcanic: Grt-Hb-Bt-Ms-Pl-Qtz-Sph-Ilm-Ep-CC	Prp-Alm-Fact-Ts-Parg-Phl-Ann-Mu-Pa-An-Ab-Cz-Qtz-Sph-Ilm-H2O (CO2-CC)	with CO_2 0.1	647	12	7.6	0.6	-0.628	115-692
					with CO_2 0.2	629	40	7.4	1.1	0.970	
					with CO_2 0.3	617	40	6.7	1.1	0.968	
					Pure H_2O	632	37	6.5	0.8	0.938	
					Fluid absent	595	65	5.8	0.9	0.861	
					$a(H_2O) = 0.9$	626	42	6.8	1.7	0.836	
TLT13	Mirsini	N37.58335 E25.20900	Metachert / Metavolcanic: Grt-Cpx-Hb-Bt-Pl-Qtz-Ms-Sph-Ilm-Ep-CC	Tr-Fact-Parg-Di-Hed-Acm-Cz-Ep-Prp-And-An-Ab-East-Ms-Fcel-Pa-Qtz-H2O-Sph-Ilm-H2O (CC-CO2)	with CO_2 0.1	582	22	8.1	0.9	0.947	419-676
					with CO_2 0.2	627	19	9.2	0.8	0.920	
					with CO_2 0.3	656	19	10.0	0.8	0.900	
					Pure H_2O	634	54	9.2	1.5	0.953	
					$a(H_2O) = 0.9$	625	51	9.1	1.4	0.952	
					$a(H_2O) = 0.7$	604	44	8.9	1.2	0.951	
					with CO_2 0.01	635	48	9.0	1.2	0.994	
					Pure H_2O	609	31	8.3	0.9	0.937	
TLT15	Mirsini	N37.58179 E25.20903	Metachert/ Metavolcanic: Grt-Hb-Bt-Qtz-Ep-Sph-Ilm-CC	Prp-Gr-Alm-Phl-Ann-An-Ab-Tr-Fact-Ts-Sph-ilm-Qtz-H2O (CC-CO2)	with CO_2 0.1	466	30	5	0.9	0.964	280-617
					with CO_2 0.2	484	25	4.6	0.8	0.956	
					with CO_2 0.01	380	45	5	1.6	0.970	
					with CO_2 0.3	501	21	3.6	0.7	0.920	
					Pure H_2O	563	56	4	0.9	0.238	
					$a(H_2O) = 0.9$	558	56	4.2	0.9	0.234	
TLT32	Amphibolite Sole	N37.57260 E25.23039	Metabasalt/ Metagabbro: Cpx-Hb-Pl-Qtz-Ep-CC-Sph-Ilm	Di-Hed-Jd-An-Ab-Tr-Fact-Ts-Parg-Gl-Ilm-Geik-Sph-Qtz-H2O (CC-CO2)	with CO_2 0.1	592	35	7.5	1.5	0.987	—
					with CO_2 0.2	610	32	7.0	1.3	0.986	
					with CO_2 0.3	619	33	6.7	1.4	0.985	
					Pure H_2O	628	47	7.1	1.7	0.676	
					$X(H_2O)$ 0.7	608	42	6.9	1.5	0.693	
TLT10	Amphibolite Sole	N37.60782 E25.23707	Metagabbro: Hb-Cpx-Pl-Qtz-Ep-Rhodingite-Sph-Ilm-Rt-Melt	Tr-Fact-Ts-Parg-Di-Hed-Jd-An-Ab-Sph-Ilm-Rt-Qtz-H2O	Pure H_2O	897	59	7.5	1.4	0.270	—
					$a(H_2O) = 0.7$	844	54	7.6	1.3	0.241	
					$a(H_2O) = 0.9$	881	58	7.5	1.4	0.262	
					$a(H_2O) = 0.5$	798	59	7.6	1.5	0.208	
TL44	Amphibolite Sole	N37.60987 E25.23942	Metabalt: Hb-Pl-Sph-Sp-Ilm-Rt-Qtz-Melt	Tr-Fact-Ts-Parg-An-Ab-Sph-Qtz-Ilm-Rt-H2O	with CO_2 0.1	590	56	10.5	2.8	0.995	—
					with CO_2 0.2	617	49	10.2	2.4	0.994	
					with CO_2 0.3	655	46	9.9	2.3	0.993	
					pure H_2O	802	132	7.9	2.8	0.019	
					$a(H_2O) = 0.5$	737	130	9.5	2.7	-0.018	
					$a(H_2O) = 0.9$	792	129	8.2	2.8	0.018	
17TL25	Amphibolite Sole	N37.60987 E25.23942	Mylonitized Metabasalt: Hb-Pl-Ilm-Sph-Melt-Mag	Tr-Fact-Parg-Di-Hed-Cz-Ab-An-Qtz-H2O	Pure H_2O	671	44	8.2	1.2	0.857	—
					$a(H_2O) = 0.9$	667	44	8.3	1.2	0.858	
					$a(H_2O) = 0.7$	658	43	8.5	1.2	0.859	
					$a(H_2O) = 0.5$	645	42	8.7	1.2	0.860	
17TL26	Amphibolite Sole	N37.60987 E25.23942	Mylonitized Metabasalt: Hb-Pl-Ilm-Sph-Melt-Mag	—	—	—	—	—	—	—	—

Tectonics

10.1029/2019TC005677

Table 2 *(continued)*

Tsiknias sole thermobarometry results	Hb-Pl thermometry				Grt-Cpx thermometry		Avg pressure (from Temp)			Al in amp barometry	
Sample	Temp (Ed-Tr) (Ca underflow)	Temp (Ed-Ri) (Ca underflow)	Temp (Ed-Tr) (No Ca underflow)	Temp (Ed-Ri) (No Ca underflow)	T (Powell, 1985)	T (Krough Ravana, 2000)	Temp (°C)	Pressure (kbar)	S.D (kbar)	*P* Max Schmidt, (1992)	*P* Max Ross & Anderson, (1996)
TLT1	547–672 (616 ± 30)	674–720 (700 ± 13)	547–675 (626 ± 31)	618–704 (684 ± 21)	—	—	600	5.8	0.3	4.76 ± 0.6	4.96 ± 0.6
							620	6.2	0.32		
							640	6.7	0.36		
							660	7.1	0.4		
							680	7.5	0.45		
							700	7.9	0.31		
TLT13	415–715 (595 ± 71)	496–636 (645 ± 40)	438–717 (610 ± 60)	545–723 (631 ± 32)	535 ± 30	655 ± 38	580	4.2	0.85	8.06 ± 0.6	8.38 ± 0.6
							600	4.6	0.88		
							620	5	0.92		
							640	5.4	0.97		
							660	5.8	1.02		
							680	6.2	1.09		
							700	6.6	1.05		
							720	6.9	1.23		
TLT15	484–709 (629 ± 66)	621–739 (680 ± 30)	484–697 (626 ± 64)	621–738 (667 ± 24)	—	—	600	5.9	0.42	10.11 ± 0.6	10.51 ± 0.6
							620	6.3	0.44		
							640	7.1	0.56		
							680	7.4	0.63		
							700	7.8	0.71		
							720	8.2	0.78		
TLT32	431–678 (572 ± 74)	591–722 (655 ± 34)	455–681 (584 ± 63)	520–641 (600 ± 33)	—	—	600	5.5	1.63	4.8 ± 0.6	5.11 ± 0.6
							620	6.1	1.55		
							640	6.7	1.6		
							660	7.2	1.65		
							680	7.6	1.77		
TLT10	511–847 (709 ± 52)	655–866 (732 ± 47)	396–844 (701 ± 73)	467–739 (617 ± 66)	—	—	740	5.6	1.53	7.75 ± 0.6	5.01 ± 0.6
							760	5.7	1.38		
							780	5.7	1.4		
							800	5.8	1.41		
TL44	742 ± 39 (661–803)	704–799 (740 ± 23)	680–794 (741 ± 32)	623–758 (683 ± 30)	—	—	700	7.7	2.31	8.69 ± 0.6	5.8 ± 0.6
							720	7.8	2.37		
							740	7.9	2.45		
							760	7.9	2.55		
							780	8	2.68		
							800	7.9	2.83		
17TL25	522–832 (688 ± 74)	764–884 (834 ± 24)	741–840 (779 ± 23)	683–820 (759 ± 27)	—	—	600	6.6	0.74	8.22 ± 0.6	5.4 ± 0.6
							650	7.7	0.58		
							700	8.9	0.62		
							750	10	0.86		
17TL26	216–715 (535 ± 133)	604–736 (690 ± 34)	216–715 (536 ± 126)	476-714 (657 ± 56)	—	—	—	—	—	8.07 ± 0.6	5.28 ± 0.6

pressure does not vary significantly with structural position across the metamorphic sole. Although there are substantial errors with some *P*–*T* estimates (±2 kbar, ± 100 °C), they consistently overlap between 6.5 and 9 kbar across the sole, implying the sole is affected by just a temperature gradient. The thermometry results also reveal that the temperature gradient is not linear and appears to get steeper within 50 m of the Tsiknias Thrust, where an apparent temperature difference of at least 150 °C occurs.

6.2. Equilibrium Phase Diagrams

Equilibrium phase diagrams (pseudosections) were constructed over a wide range of pressures and temperatures using THERMOCALC v3.40i and data set DS62 and are presented in Figure 11. Additional phase diagrams are presented in the supporting information. Due to reasonably high spessartine contents in garnets in metasediments, modeling of metasediments was performed in the $MnO–Na_2O–CaO–K_2O–FeO–MgO–Al_2O_3–SiO_2–H_2O–TiO_2–O$ (MnNCKFMASHTO) system using the White, Powell, Holland, et al. (2014); White, Powell, & Johnson (2014) activity-composition relations for the MnO system and the use of the omphacitic--clinopyroxene and amphibole activity-composition relations of Green et al. (2016). Whereas mafic rocks were modeled in the MnO free system (NCKFMASHTO) using the Green et al. (2016) activity models for partial melting in mafic rocks. The pure phases andalusite, kyanite, sillimanite, rutile, quartz, and H_2O were considered in all cases. The effective bulk rock composition used for modeling was initially calculated following the method of Carson et al. (1999), whereby modal proportions of minerals, calculated from representative SEM images and thin sections, were combined with their representative compositions. Where relevant, the Fe^{3+} content of individual minerals was calculated using the software AX (Holland, 2009; last accessed August 2018). The following phase diagrams of anatectic amphibolites were created using the observed mineralogy of an entire representative thin section which contained crystallized leucosomes and veins that may have been partially derived from melting adjacent rocks. Although it is acknowledged in the anatectic amphibolites, some degree of melt loss occurred resulting in ponding of leucocratic melt in veins and fractures on a microscale and macroscale (Figure 6 and supporting information), it is important to note that melting only occurred within a few meters of the Tsiknias Thrust and therefore did not migrate far from its source. We therefore believe that over a thin section scale, it represents the effective bulk rock composition during peak metamorphism.

6.2.1. TLT10 (Anatectic Amphibolite)

An equilibrium phase diagram of TLT10 taken from 1 m below the Tsiknias Thrust (Figures 11a and 11b) shows relatively complicated phase relationships at subsolidus temperatures but simple topology suprasolidus. The observed peak assemblage Hb + Aug + Pl + ilm + Qtz + Liq lies over a wide range of *P*–*T* conditions ~750–900 °C and 4–10 kbar along a positive *P*–*T* gradient, without a change in variance. Contours for y (amp) = XAl in M2 site and c(pl) = XCa show that aluminium content in amphibole increases with increasing pressure and increases in anorthite content with increasing temperature. Intersection of these isopleths (y(amp) = 0.28–0.35 corresponding to a c(pl) in plagioclase = 0.41) provide a *P*–*T* constraint of ~6–9 kbar at 850–900 °C for peak metamorphic conditions corresponding to melt fraction of 11–12% in the phase field Hb + Aug + Pl + ilm + Qtz + Melt, consistent with the observed assemblage. The range of XAl in M2 site in amphibole suggest the rock decompressed while at high temperature, although the lack of Opx (predicted in the bottom right corner of the diagram) in the sample indicates it must have also cooled. Titanite is predicted at lower temperatures indicating that it is a retrograde phase. The appearance of garnet at ~10.5–11 kbar provide a maximum upper constraint for the *P*–*T* conditions. These predictions agree with thermobarometry results, although they have a large uncertainty.

6.2.2. TLT1 (Mirsini Unit Metapelite)

The phase diagram for TLT1 (Figures 11c and 11d) predicts the observed assemblage Grt + Bt + Ms + Pl + ilm + Qtz + Liq in a small field directly on the water-saturated solidus at ~8.5 kbar and 680 °C and with a few degrees Celsius of the muscovite out reaction, consistent with <1% observed muscovite in the assemblage. The garnet in reaction is constrained to >640 °C and therefore provides a lower temperature bound. Consideration of garnet grossular (XCa) and pyrope (XMg) isopleths provides tight *P*–*T* constrains for garnet core growth (Prp = 0.02 and Grs = 0.19) at 7.7 kbar and 660 °C immediately after crossing the garnet producing reaction, and garnet rims (Prp = 0.04 and Grs = 0.24) at 8.7 kbar, 680 °C in the phase field Grt + Bt + Pl + Ms + ilm + Hb + Liq. These results suggest garnet grew along a path of both increasing pressure and temperature over a very limited *P*–*T* range and explains the rare occurrence of garnet at outcrop. The occurrence of relict epidote, commonly breaking down to muscovite and plagioclase in

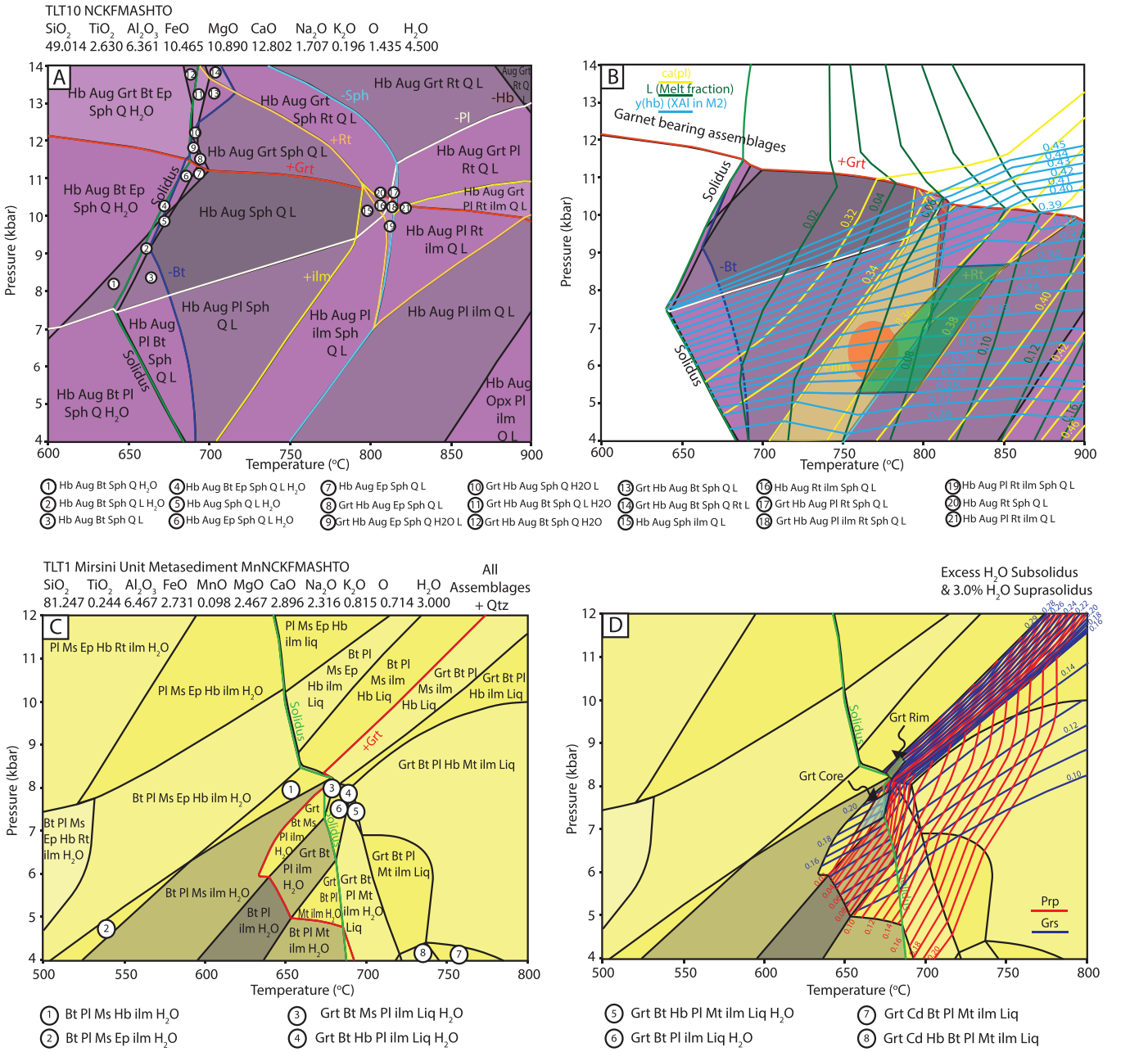

Figure 11. Equilibrium phase diagrams of anatectic amphibolite samples TLT10 and 17TL25: (a) TLT10 phase relations, (b) overlaid isopleths for y(hb), c(pl), and mode of melt for TLT10, (c) TLT1 phase relations with Grt in reaction (red line). (d) Overlaid garnet pyrope (Prp) and grossular (Grs) composition isopleths, showing the garnet core and rim intersection (shaded polygons).

the rock also strongly suggests that the rock underwent a clockwise prograde *P–T* path. These *P–T* constraints are consistent with thermobarometry results and this pressure constraint provides the best estimate for the depth of metamorphism in the sole and suggests at least under water saturated conditions, it started to melt. The presence of magnetite in the matrix, suggest its retrograde path involved decompression, while still at high temperature.

6.3. Summary of *P–T* results

The integrated equilibrium phase diagram modeling and independent thermobarometry (Figure 13) show that there is a resolvable temperature gradient of >300 °C/km throughout the metamorphic sole at

pressures of approximately 8.5 kbar, although some slightly lower pressures are recorded possibly due to thermal reequilibration during decompression. Anatectic amphibolites record temperatures of at least 850 °C directly under the Tsiknias thrust; they experienced at least 11–12% melting and show a range of pressures from ~9–6 kbar, implying they decompressed while at high temperature. The Mirsini Unit metasediments also record amphibolite facies-temperatures of up 600–715 °C, while also at ~8.5 kbar, although significantly lower temperature than the amphibolites 50–150 m directly above them. The rocks underwent a clockwise prograde *P*–*T* path as indicated by lower-pressure phases overprinting higher-pressure, peak metamorphic phases, and increases in pressure and temperature during garnet growth (TLT1). In summary, the consistent pressures of ~8–8.5 kbar recorded in the metamorphic sole suggest that the exposed structural section of the Upper Unit represents a subduction zone interface at ~25- to 30-km depth at the time of high-grade metamorphism.

7. Whole Rock Geochemistry

Spider diagrams (Figure 12) are normalized to normal mid-ocean ridge basalts (N-MORB) values from Sun and McDonough (1989), and V and Sc are included and are normalized to N-MORB values quoted in Klein (2004) and show there are at least two distinct gabbro chemistries from the Tsiknias Ophiolite on Tinos (Figure 12). Gabbro 17TL24 has significant large ion lithophile element (LILE) enrichment, with a negative Nb anomaly relative to Th, a subduction input proxy (Pearce, 2014), and a strong depletion in Hf. Gabbros also display flat high field strength (HFSE's) patterns relative to N-MORB and have slightly convex downward rare earth element (REE) patterns with relatively low REE abundances (~10 times N-MORB) and exhibit light rare earth element (LREE) patterns that indicate some enrichment relative to N-MORB. Gabbro sample 17TL27 shows similar REE patterns, although it lacks a depletion in Nb relative to Th, suggesting it was derived from a melt less influenced from subduction.

The other gabbro population (samples 17TL23 and TLT26) shows some enrichment in LILEs but depletion in Th and Nb and strong depletion in the HFSEs and REEs (0.1–0.9 times N-MORB). This HFSE depletion in these gabbros may be due to fractional crystallization, which changes the level but not the topology of the pattern (Pearce, 1983). There is also a positive Y and Sc excursion relative to the rest of the REEs, suggesting the crystallization of pyroxene from melt (Eby, 1973). This correlates with a depletion in these elements within the plagiogranites, suggesting that these gabbros are partial cumulates and are therefore not primary mantle melts. This inverse correlation in trace elements between cumulates and the plagiogranite suggest that the plagiogranite could be derived from the gabbros as a result of hydration and subsequent partial melting. Plagiogranite samples (TLT63 and 17TL35) also show some enrichment in LILE but remain relatively flat relative to MORB with significant depletion in Ti and Hf.

In contrast, the sole amphibolites show significant enrichment of LILEs and convex upward trends in REE with smaller degrees of enrichment in LREEs, relative to N-MORB and no obvious depletion in Nb relative to Th. In contrast, N-MORB samples invariably have LREE-depleted patterns (Saunders, 1984), whereas flat to REE-enriched patterns with relatively low abundances are more characteristic of island arc tholeiites (IAT). The metamorphic sole REE patterns therefore most closely match either enriched mid-ocean ridge basalt (E-MORB) or IAT trends.

Discrimination diagrams (Figure 13 and supporting information) reenforce the spiderdiagram patterns and verify the presence of cumulate gabbros as well as subduction (17TL-24) and nonsubduction influenced gabbros (sample 17TL27). Incorporation of literature gabbro data suggests the Tsiknias gabbros span the MORB-volcanic arc fields, reflecting a variable subduction input. The plagiogranites plot above the N-MORB/OIB array in the Th versus Nb diagrams and straddle the IAT to oceanic arc fields. These patterns are also observed in the Nb versus Y plot with the plagiogranites straddling the volcanic arc granite (VAG) and ocean ridge granite (ORG) and overlap with Oman and Troodos ophiolite plagiogranites. These samples also plot on the boundary between ocean ridge granite and volcanic arc affinities in the Rb versus (Y + Nb) and Rb versus (Yb + Ta) plots (see supporting information), strongly suggesting a suprasubduction zone signature.

The amphibolites plot within the MORB/OIB array with some potential Th enrichment in samples TLT7 and TLTN12. However, in the V versus Ti/100 discrimination plot, they plot exclusively in the MORB and slab distal back-arc basin fields. Combination of the V-Ti/100, total alkali versus silica and Zr/Ti versus Nb/Y immobile element proxy plot (Pearce, 1996) suggests that the sole rocks have basaltic protoliths, and

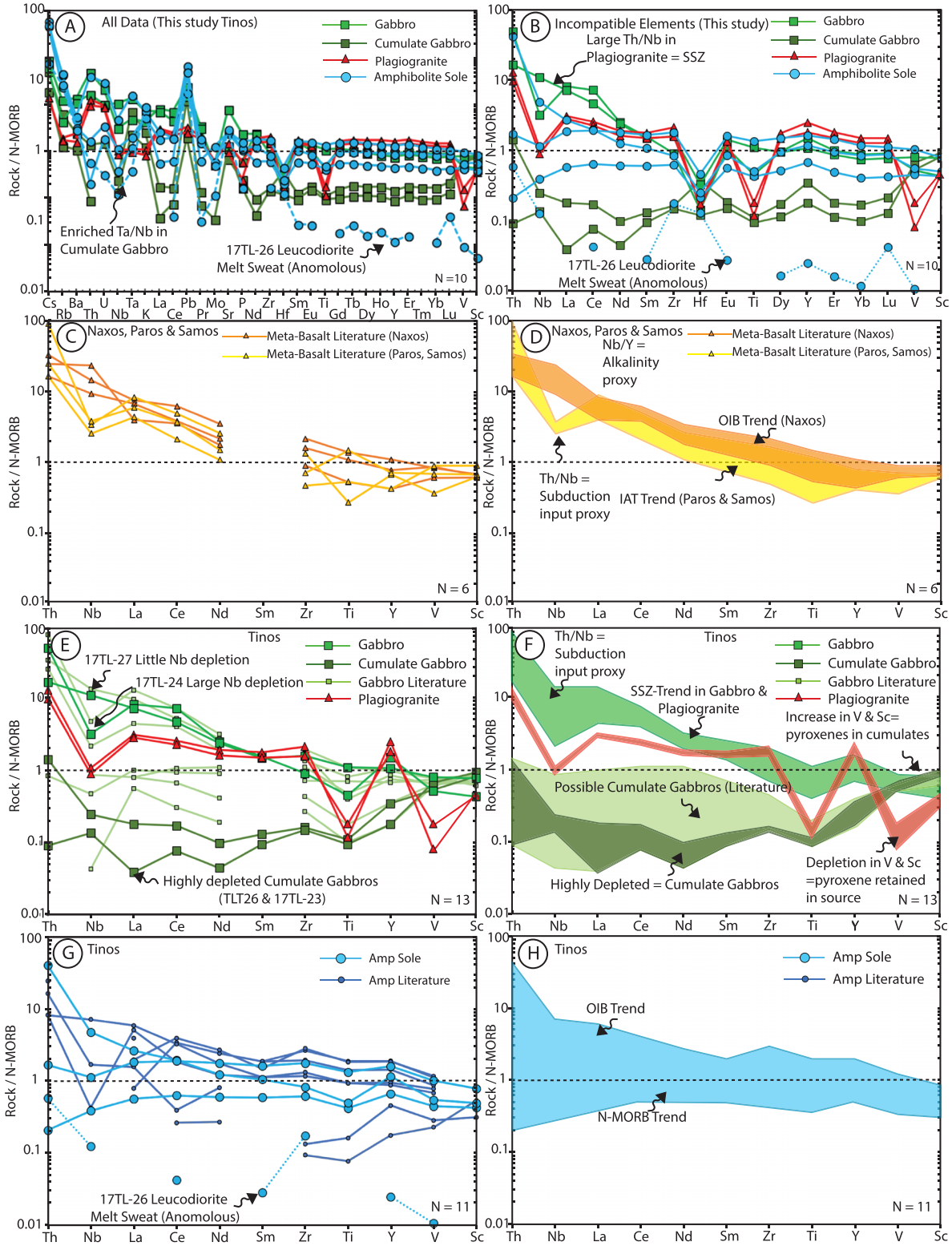

Figure 12. Spider diagrams of trace element data from the plagiogranite, gabbros, and amphibolites from the sole, plotted with literature metabasalt gabbro, and amphibolite data (from Stouraiti et al., 2017; Katzir et al., 1996) normalized to N-MORB using the normalization of Sun and McDonough (1989). (c–h) Simplified spider diagrams normalized to N-MORB combined with literature data and plotted for rock type and summary trends. (c and d) Cycladic metabasalts. (e and f) Intrusive ophiolitic rocks including primary gabbros and cumulate gabbros from this study, and literature gabbros and plagiogranites from this study. (g and h) Amphibolites including metamorphic sole rocks from this study and literature amphibolites, excluding 17TL26 leucodiorite melt vein.

10.1029/2019TC005677

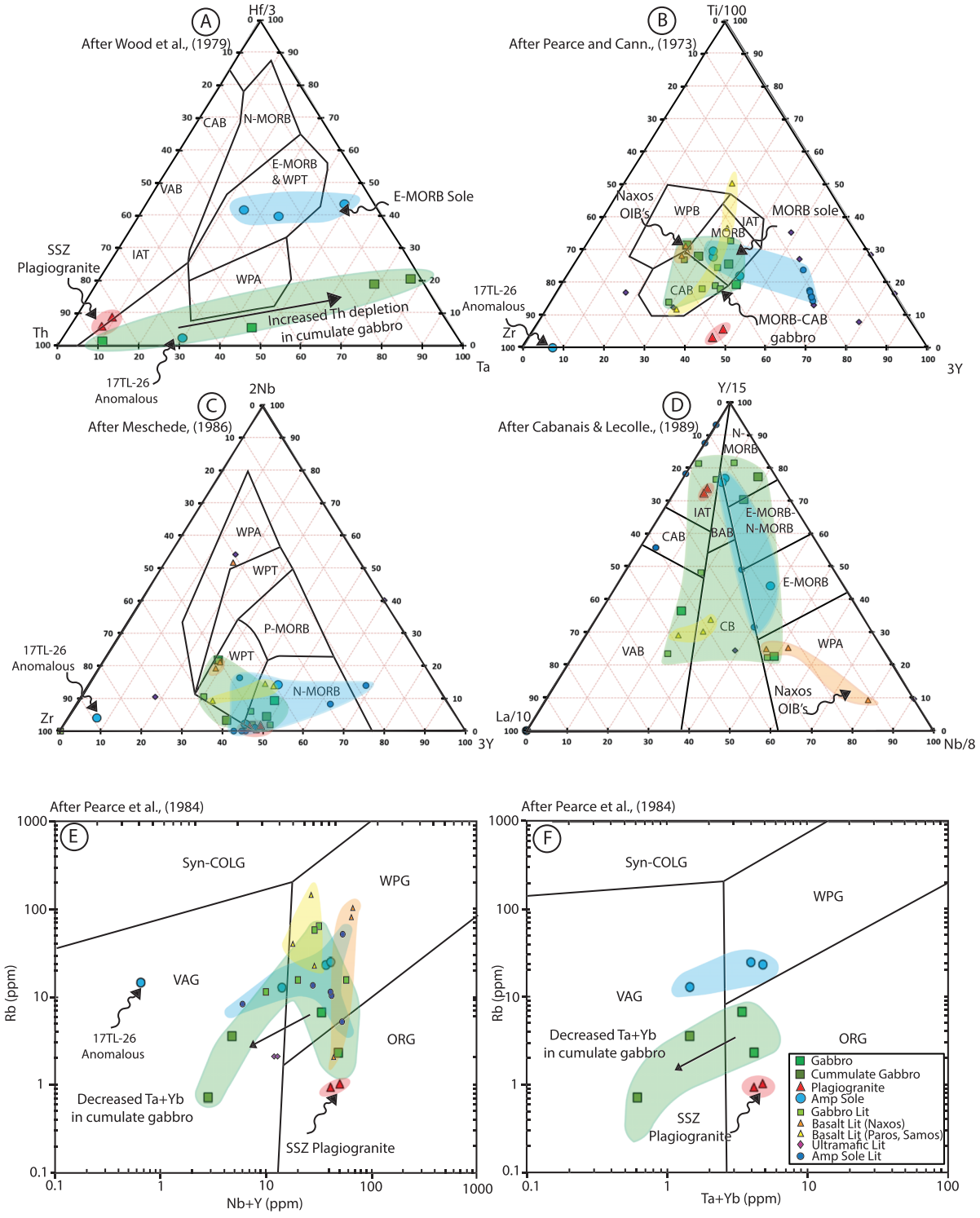

Figure 13. (a) Hf/3-Th-Ta after Wood et al. (1979); E-MORB, oceanic basalt from an anomalous MOR segment (e.g., high-heat flow); (b) Ti/100-Zr:3Y after Pearce and Cann (1973); WPB, within-plate basalt; OFB, ocean floor basalt; LKT, low-potassium tholeiite; CAB, calc-alkaline basalt. (c) 2Nb-Zr-3Y after Meschede (1986); WPA, within-plate alkaline; WPT, within-plate tholeiite, N-type MORB, oceanic basalt from a normal MOR; *P*-type MORB, basalt from plume-influenced MOR; VAB, volcanic arc basalt. (d) Y/15-La/10-Nb/8 after Cabanis and Lecolle (1989). E-MORB = enriched mid-ocean ridge basalt; N-MORB = normal mid-ocean ridge basalt. (e and f) Tectonic discrimination diagrams after Pearce et al., 1984.

integration of spiderdiagram patterns indicate they are best described as E-MORB and formed within the distal ocean.

Metabasalts from the Aegean literature show several patterns (Bröcker et al., 2014; Koglin et al., 2009; Mocek, 2001; Stouraiti et al., 2017). Naxos metabasalts which occur within the Upper Unit trench mèlange (Lamont et al., 2019) display weak depletion in Nb relative to Th, and positive and small REEs excursions relative to N-MORB, with a moderate Nb-Y variation, strongly suggesting an ocean island basalt (OIB) affinity (Stouraiti et al., 2017). Whereas on Paros and Samos, the basalts show some Nb depletion relative to Th, with mainly flat HFSE patterns and little variation between Nb and Y, indicative of an IAT affinity and show similar chemistry to the Tsiknias gabbros, potentially suggesting that they could represent the upper crustal rocks. In Figure 13, Naxos metabasalts plot mainly in the within-plate alkali basalt and within-plate tholeiite fields, whereas Paros and Samos rocks plot in the within-plate tholeiite to volcanic arc basalt fields (e.g., Ti/100-Zr-3Y, 2Nb-Zr-3Y, and Y/15-La/10-Nb/3 ternary diagrams). The OIB trends from Naxos metabasalts are distinctly different from the Tsiknias gabbros, which mainly plot across an array from IAT to within-plate basalt fields (e.g., Hf/3-Th-Ta and Y/15-La/10-Nb/8 ternary diagrams). In contrast, the high-pressure rocks on Sifnos and Tinos, protoliths of the eclogites within the Cycladic Blueschist Unit (Lower Unit) are characterized as calc-alkaline basalts, andesites, and Fe-rich tholeiites evolving in an island-arc setting (Bröcker et al., 2014; Mocek, 2001).

8. Geochronology

8.1. 17TL35 Plagiogranite

Zircons were small and mostly display sector zoning, although some display weak oscillatory zoning (Figure 14). Dating of both outer and inner regions (no distinct core-rim pairs were visible) gave a single age population ($n = 10$) with mainly concordant data. The lower intercept age using the Tera-Wasserburg diagram of this sample is 161.9 ± 1.3/2.8 Ma (MSWD of 0.68; Figure 15a). This date is interpreted as an absolute minimum age of the formation of oceanic crust associated with ophiolite formation. Because the plagiogranite retains a strong SSZ signature, this confirms that spreading at ~162 Ma occurred above a subduction zone.

8.2. 17TL27 Gabbro

A limited amount of zircon was successfully extracted from sample 17TL27, a partially tectonized gabbro horizon belonging to the interpreted Moho Transition Zone (see Figures 2–5). The zircon grains were small (<30 μm) and display weak oscillatory zoning textures typical of magmatic zircon (Corfu et al., 2003; Figure 17). The data comprised a component of common lead and have very low concentrations of U and Th (3–1,042 ppm U and 0.04–156 ppm Th). Dates from three zircon grains are interpreted as inheritance (227, 365, and 405 Ma). Five younger and overlapping dates provide a lower intercept age of 144.3 ± 5.2/5.6 Ma with an MSWD of 0.92 (Figure 15b).

8.3. 17TL26 Leucodioritic Melt Sweats From Metamorphic Sole

Zircon grains extracted from the melt sweats hosted within amphibolites directly below the contact with the ophiolite are rare, small, and have stubby to elongate morphologies (see Figure 14). Zoning in CL is variable, exhibiting weak oscillatory and weak fir-tree zonation patterns and characterized by low U concentrations suggesting a metamorphic origin. Core-rim relationships are not particularly clear (Figure 14). The first attempt at dating using the standard method of zircon mounted in epoxy and polished to expose the grains yielded a broad spectrum of dates from 113 to 64 Ma. To better constrain the age of the outermost zone, zircon was mounted on tape and analyzed from the outside in. The latter data yielded a better population of dates with a lower intercept age of 74.0 ± 3.3/3.5 Ma (MSWD = 3.1), that we interpret as reflecting crystallization of the outer and younger most zircon domains. Because zircons are weakly and heterogeneously zoned with fine overgrowths on inherited cores, we interpret this age as reflecting the crystallization of melt during fluid-assisted partial melting during metamorphism. Four older ages yield a weighted mean common lead corrected age of 189 ± 10/10 Ma (MSWD = 4.7), which we interpret as a constraint on the formation of the mafic protolith to the amphibolite.

Figure 14. Cathode luminescence images of zircon morphologies and zoning showing ablation spots from reported ages of (top row) Plagiogranite (17TL35), (middle row) Leuco-diorite melt sweats from the metamorphic sole (17TL26), and (bottom row) Gabbros (17TL27).

9. Discussion

9.1. Formation of the Tsiknias Ophiolite

The stratigraphy of the Tsiknias Ophiolite is unusual with respect to conventional Penrose stratigraphy, particularly the intrusion of such a large plagiogranite body (see Figure 7), the thick and highly tectonized gabbros of the Moho Transition Zone, and the lack of exposure of upper-crustal rock; all of which makes it difficult to fit this ophiolite into this traditional framework. However, it is consistent with more recent definitions of Ophiolite (Dilek & Furnes, 2011). Unfortunately, the lack of exposure and current erosion level of the Tsiknias ophiolite makes it difficult to make further suggestions for its formation beyond speculation.

U–Pb geochronology constrains the age of Tsiknias Ophilolite formation to 161.9 ± 2.8 Ma, within uncertainty of the reported U–Pb ages of 160 ± 1 Ma for the "East Vardar Ophiolites" on mainland Greece, particularly the Guevgueil Ophiolite (Froitzheim et al., 2014) and the Samothraki ophiolite sequence (Koglin, 2008). Although a similar age is reported for the Mirdita Ophiolite (Dilek et al., 2007; Figures 1 and 17), the N-MORB geochemistry is incompatible with that of Tsiknias plagiogranites and gabbros. Geochemistry of gabbro and plagiogranite within the Tsiknias Ophiolite sequence shows variable trace element patterns suggesting a complicated evolution. Plagiogranites and primary gabbros reveal an SSZ affinity, signifying that the ophiolite formed above a subduction zone. This is similar to many of the Dinaric Ophiolites, and the East Vardar Ophiolites but not the Vourinous or Orthis Ophiolites ("West Vardar Ophiolites") that display N-MORB/E-MORB geochemistries overprinted by SSZ signatures (e.g., Maffione

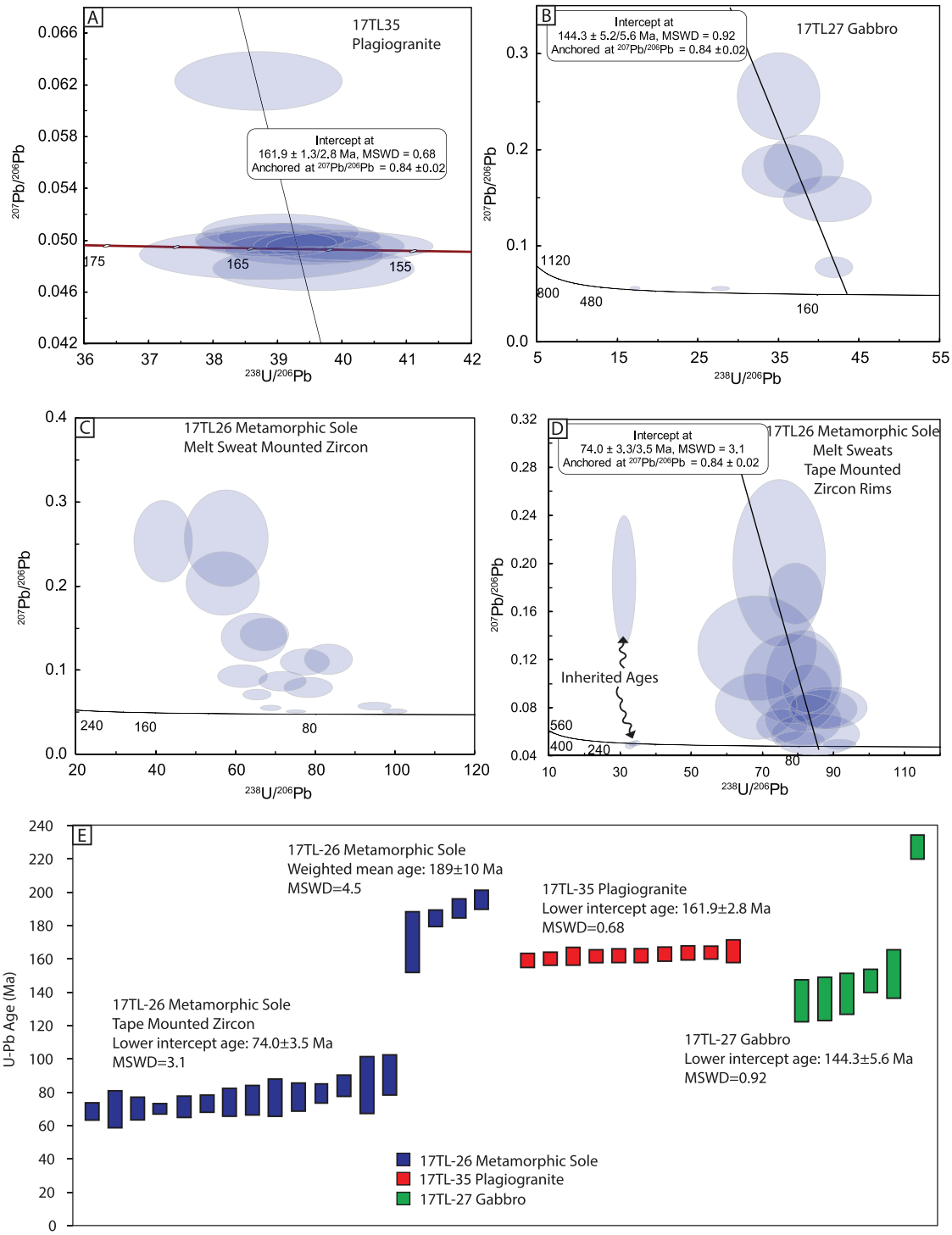

Figure 15. Tera-Wasserburg U-Pb plots for (a) 17TL35, plagiogranite; (b) 17TL27 a gabbro; (c) 17TL26 sole amphibolite (epoxy mounted zircon); (d) 17TL26 sole amphibolite (tape-mounted zircon), (e) Rank-age plot of common lead corrected $^{206}Pb/^{238}U$ ages for each sample showing only tape mounted zircon for 17TL26.

& van Hinsbergen, 2018, and references therein; Robertson, 2002; Katzir et al., 1996; Stouraiti et al., 2017), although the north Mirdita Ophiolite shows a complicated evolution with a strong subduction influence (Dilek & Furnes, 2009, 2014; Furnes et al., 2014; Furnes & Dilek, 2017). However, no further information on the geometry of the subduction zone responsible for the formation of the Tsiknias Ophiolite can be obtained from these data alone. One major difference compared to these ophiolites however, is a ~90-Myr

discrepancy between the ophiolite and sole age, as these ophiolites were obducted at the same time they formed (e.g., Maffione & van Hinsbergen, 2018, and references therein).

Gabbro and plagiogranite petrography and chemistry suggest a complicated history of partial melting and crystallization within the Tsiknias Moho Transition Zone. The formation of oceanic plagiogranite has been attributed primarily to either of the following: (1) late stage differentiation of low-K tholeiitic MORB magmas (Coleman & Donato, 1979; Coleman & Peterman, 1975; Floyd et al., 2000; Pallister & Knight, 1981); (2) hydrous partial melting of gabbro or similar melts in a MOR setting (Floyd et al., 2000; Gerlach et al., 1981; Spulber & Rutherford, 1983); or (3) liquid immiscibility in an evolved MORB liquid (Dixon & Rutherford, 1979; Floyd et al., 2000; Philpotts, 1976). In a simple fractional crystallization case, the observed volume of plagiogranite would require an exceptionally large initial volume of a low-K mantle melt that would have undergone extreme fractionation, much more than can be accounted for from the low volume of the underlying gabbroic intrusions. The inverse correlation in REEs between highly depleted cumulate gabbros and the plagiogranites, however, strongly suggests the two could be derived from an original mafic source that underwent either partial melting or fractional crystallization. To further complicate matters, another type of gabbro (17TL24 and 17TL27) with a composition lacking a subduction signature and of an E-MORB affinity forms part of the same sequence and has a U–Pb age of 144.3 $\pm$ 5.6 Ma, younger than the SSZ plagiogranite. Trace element data from this sample (17TL27) suggest an enriched signature relative to N-MORB, although the lack of Nb excursion relative to Th suggests that this sample did not derive from a magma influenced by subduction. This gabbro is composed of over 40% hornblende, indicating it was hydrated during crystallization. Zircon textures suggest an igneous origin (Corfu et al., 2003); however, four out of five grains yield the ~144 Ma age exhibit low Th/U ratios (<0.1), which is typically regarded as representing metamorphic zircon (Rubatto, 2017). Despite this, it has been shown that magmatic zircon can exhibit Th/U ratios <0.1, due to a relatively U-rich magma composition (during fractional crystallization) and the absence of other U-enriched accessory minerals during zircon crystallization (e.g., Lopez-Sanchez et al., 2016). Other hornblende rich ophiolitic gabbros with low Th/U magmatic zircon ratios have been documented in Corsica and Crete (Li et al., 2015; Liati et al., 2004). Alternatively, it is shown that zircon growth from relative U-rich and magma close to the solidus and under fluid rich conditions can contribute to low Th/U ratios in zircon (Yakymchuk et al., 2018). Full microprobe thin section maps for Th and phosphorous (see Figures S13–S15) show no other Th-bearing accessory phases (e.g., monazite, allanite), although a few grains of titanite contain trace amounts. Zircon in sample 17TL-27 is therefore interpreted to have an igneous origin. The ~18-Myr age discrepancy from the plagiogranite, which formed in an SSZ setting, suggest that gabbro formation, crystallization, and hydration occurred with variable amounts of subduction interaction. This implies that formation of the Tsiknias Ophiolite occurred first in an SSZ setting, followed by a transition to a back-arc basin setting, and/or the ending of subduction by ~144 Ma.

In contrast, the metabasalts on Naxos (Lamont et al., 2019; Stouraiti et al., 2017) cannot be related to the Tsiknias Ophiolite and probably represent alkali and ocean island basalts that formed on the subducting plate (lower plate) similar to the metamorphic sole protolith. Metabasalts on Naxos are exposed today within trench mélange, pelagic sediments, and limestone exotics (Lamont et al., 2019), similar to the Haybi Complex beneath the Oman/UAE Ophiolite (Searle et al., 2004).

9.2. Timing of Ophiolite Obduction and Metamorphism in the Sole

The youngest U–Pb age population associated with the zircon rims of ~74 Ma represents an absolute minimum constraint for the timing of high-grade metamorphism, anatexis, and top-to-SW shearing within the sole amphibolites, as there is no evidence for further deformation or metamorphism apart from granite intrusion (at ~14.6 Ma; Brichau et al., 2007) that postdates anatexis. This metamorphic age is further supported by K–Ar and Ar–Ar ages within the Upper Unit amphibolites of ~67 Ma (Maluski et al., 1987; Patzak et al., 1994) and our Lu–Hf garnet age (two-point isochron) of ~ 66 Ma (see Text S1), although this latter age must be treated with some caution. The ~190 Ma of the mafic protolith is significantly older than the formation age of the overriding ophiolite (~162 Ma). This combined with differences in trace element data suggesting an E-MORB to back-arc basin basalt affinity, reveal that the sole-amphibolite protolith belongs to a different fragment of oceanic crust to the overriding Tsiknias Ophiolite. The timing of high-grade metamorphism and anatexis within the sole is constrained to ~74 Ma, ~90 Myr after the formation of the overriding ophiolite. This is an unusual occurrence, as many ophiolites and their soles normally

form at, or around, the same time (van Hinsbergen et al., 2015; Wakabayashi & Dilek, 2000). Examples of simultaneous ophiolite and sole formation include the Semail Ophiolite (Searle & Malpas, 1982; Gnos & Peters, 1993; Searle & Cox, 1999; Rioux et al., 2016), the Vourinos-Pindos Ophiolite (e.g., Robertson, 2002), and Albanian ophiolites (Dilek et al., 2008). To explain subduction zone geochemical signatures within the ophiolitic crustal rocks, metamorphic sole formation in a subduction setting allows oceanic crust to be subducted simultaneous to forearc spreading and generation of SSZ crust in the overriding upper plate (e.g. Searle & Cox, 2002; Dewey & Cassey, 2011).

Importantly, the Tsiknias Ophiolite does not fit this pattern, as the ~ 90 Myr age difference between sole formation and ophiolite formation cannot be explained by a single subduction zone for both its origin and emplacement. Although different to most ophiolites, globally, no soles have been found that predate the ophiolites (Wakabayashi & Dilek, 2000), which suggests that metamorphic soles form simultaneously with or following the first generation of oceanic crust. This led Wakabayashi and Dilek (2003) to suggest that many ophiolites could have formed above an older subduction zone than the one responsible for the formation of their metamorphic sole. Under these circumstances, the ophiolite would be emplaced above a separate, younger, subduction zone than the one they formed above. The discrepancy in ages (~162 Ma vs. 74 Ma) and geochemistry (SSZ vs. E-MORB) between the Tsiknias Ophiolite and sole, are consistent with a model of separate subduction zones responsible for ophiolite formation and obduction, thus requiring the formation of the sole to be completely unrelated to the subduction zone that formed the ophiolite. The Tsiknias Ophiolite also likely formed over a short time interval specifically between ~162 Ma and 140 Ma, because ~90 Myr of continuous spreading equates to the formation of thousands of kilometers of oceanic crust. If the ophiolite did form above the same subduction zone as the one responsible for forming the sole, it would require thousands of kilometers of shortening to close a wide ocean basin, and is in disagreement with the present-day regional structure, which rather argues for orders of magnitude less shortening.

The ~74 Ma age of the sole formation is geodynamically important as it directly correlates with when the African lithospheric plate motion switches from dominantly E–W transcurrent to N–S convergent motion (Vissers & Meijer, 2012). The changes in regional tectonic stresses at around this time could possibly have induced the initiation of a new subduction zone at the location where there is a ~30 Myr age difference and hence density difference in oceanic lithosphere (190 Ma for the sole protolith vs. 162 Ma for the ophiolite). The Gorringe Bank off the coast of Iberia could be a present-day analogy to subduction initiation in cold ~90 Myr old oceanic crust (Hayward et al., 1999; Jiménez-Munt et al., 2010 and references therein). This feature represents an intraoceanic thrust, placing old oceanic crust and mantle over even older oceanic crust, strikes (NW-SE) oblique to the spreading direction, and could indeed represent similar processes in action to what is observed on the Tsiknias Thrust.

9.3. The Cause of Metamorphism in the Sole

Partial melting within the uppermost few meters of the sole amphibolites, directly under the Tsiknias Thrust and base of the ophiolite, occurred dominantly by water-saturated melting of amphibole during top-to-SW ductile shearing (Figures 5 and 6). The sole shows an inverted tectonostratigraphy with amphibolites at the top and pelagic metasediments including metacherts, flysch, and turbidite sequences toward the base. This suggests that there are several distinct thrust slices within the sole. However, all these lithologies record similar pressures of ~8–8.5 kbar, but with temperatures varying continually between 600 and 850 °C between the base and the top, implying that metamorphism occurred concomitantly with thrusting (Figure 16). Underthrusting, prograde metamorphism, and subsequent dehydration of underlying metasediments and amphibolites within the sole and Mirsini Unit could have acted as a possible water source to drive partial melting in the upper few meters of the sole where temperatures were greatest.

In many ophiolites worldwide (with coeval ophiolite and sole formation), the metamorphic sole has been proposed to represent the subduction zone interface with the heat causing metamorphism derived from the overlying mantle wedge. In these settings, the newly formed mantle wedge is expected to be hot and would conductively heat the top of the subducting slab. Based on this reasoning, many argue that subduction initiation must occur immediately prior to sole formation (Cowan et al., 2014; Hacker, 1990; Hacker et al., 1996; Hacker & Gnos, 1997), because if left any longer than a few million years, the mantle wedge would have sufficiently cooled (e.g., Gerya & Stöckhert, 2006).

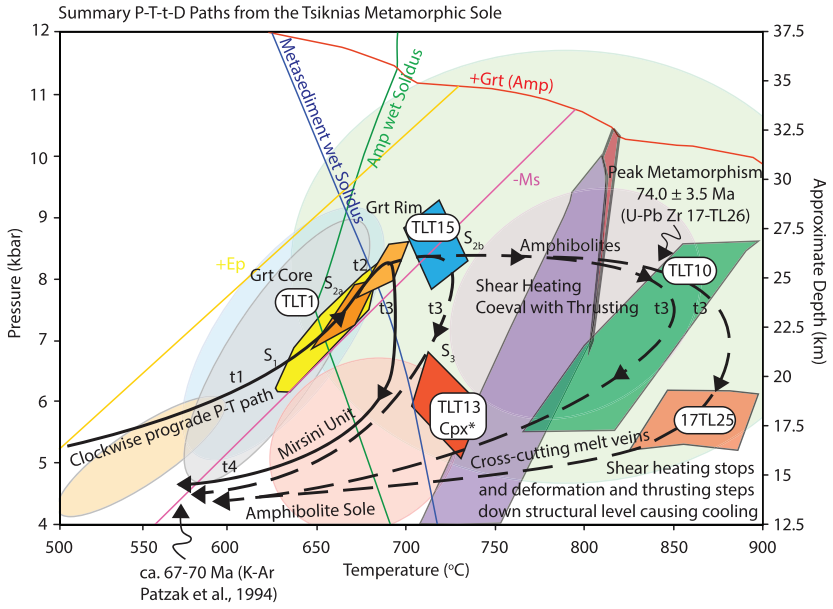

Figure 16. Summary *P-T* overlaying thermobarometry with pseudosection results, showing agreement between the results of the two methods. Although there are large-pressure uncertainities, the temperatures systematically increase by ~250 °C from the bottom to the top of the expose sole, at around the same pressure of ~8.5 kbar (best constrained by TLT1) reflecting a temperature gradient of ~ > 300 °C/km.

P–T conditions for metamorphism in the Tsiknias sole of ~8.5 kbar, 600–850 °C (Figure 16) correspond to an apparent inverted metamorphic field gradient of >300 °C/km. Several mechanisms have been proposed to produce such steep thermal gradients. Sequential underplating would result in a package of rocks that record their peak metamorphic temperatures at slightly different times and hence produce a diachronous apparent "frozen in" inverted temperature gradient that would be steeper than the true thermal gradient at any given time. In this model, metamorphism and deformation are expected to migrate down structural section with time, resulting in the earliest buried rocks at the top of the sequence and youngest buried rocks at the bottom. However, this mechanism is unlikely to be important in the Tsiknias metamorphic sole for several reasons: (1) The sequence is <300 m thick therefore requiring a significant quantity of missing subducted material to be accounted for. (2) The sequence does not show discrete jumps in metamorphic grade, neither does it show evidence for lower temperature deformation superimposed on the peak metamorphic assemblages. (3) According to this model, the deepest (and youngest) buried rocks in the sole sequence (metasediments) still record temperatures of ~600 °C. Because the metamorphic sole represents the interface between the top of the subducting slab and the overlying mantle, the heat source to cause metamorphism must have come from above rather than the colder underlying subducting crust. If the sole has not been subsequently attenuated, the overlying amphibolites <300 m away should therefore have also been strongly affected by this lower temperature regime and show features consistent with reequilibration at lower than their peak metamorphic temperatures that were recorded earlier in the rock's history. Such strong retrograde overprinting features are not observed. (4) Underplating cannot explain the high temperatures recorded across the sole (see argument below for additional heating mechanism required to cause metamorphism due to the 90-Myr age discrepancy between the ophiolite and the sole).

It has also been suggested that extreme postmetamorphic flattening and lateral attenuation during subsequent shearing could produce an extremely condensed metamorphic field gradient within metamorphic soles (Cowan et al., 2014; Searle & Cox, 2002). However, in the Tsiknias metamorphic sole there is no evidence for significant postmetamorphic flattening of isotherms as high-temperature posttectonic microstructures and anatectic features occur coeval with or have been superimposed on the deformation fabrics, as demonstrated by melt veins which crosscut the S_{2b} mylonite fabric (Figures 6 and 8).

If this steep and inverted thermal gradient across the Tsiknias metamorphic sole is not a diachronous feature and is representative of the temperature distribution through the uppermost few hundred meters of a

subducting slab, it is inconsistent with heating by exclusively thermal conduction due to the overriding mantle. This is because the length scale for thermal diffusion for this configuration would be on the order of kilometers to tens of kilometers. Furthermore, if subduction initiated within cold and old oceanic lithosphere, conductive heating alone from an already cooled 90-Myr-old mantle of the upper plate at 25–30 km depth would be insufficient to drive high-grade metamorphism at suprasolidus temperatures on the interface of the downgoing slab. The temperatures predicted by thermal plate models of ~90-Myr-old oceanic lithosphere at 25–30 km depth are only ~300–450 °C (Parsons & Sclater, 1977; Stein & Stein, 1992). Additional sources of heat are therefore necessary to form the metamorphic sole and its inverted temperature gradient.

It is possible that during subduction initiation, advection of hotter asthenospheric mantle would flow into the newly formed mantle wedge and would subsequently act to heat the subduction interface (e.g., Stern, 2004). However, this incursion of the mantle wedge is unlikely to reach depths as shallow as 25–30 km, although it may still experience some thermal effects.

Alternatively shear heating may play an important role (England & Molnar, 1993) and has been used to explain high-grade tectonites in major shear zones including the Alpine Fault and Great Slave Lake Shear Zone (Leloup et al., 1999, and references therein), and an inverted thermal gradient in the Pelona Schist in Southern California (Graham & England, 1976). In rocks affected by high strain rates and shear stresses of tens of megapascals (as predicted in subduction zones; England, 2018), dissipative heating should contribute significantly to the thermal budget of deforming metamorphic systems and increase temperatures by a few hundred degrees (England & Molnar, 1993; Mako & Caddick, 2018; Peacock, 1992). Shear heating would predict the following: (1) the highest strained rocks (closest to the Tsiknias Thrust) to record the highest temperatures and the lowest strained rocks (furthest away from the Tsiknias Thrust) to record the lowest temperatures; (2) peak metamorphism to be coeval with shearing (top-to-SW kinematics). Although, some workers have argued that shear heating would be localized along the particular fault plane or shear zone and the addition of fluids to a serpentinites would produce talc, which would substantially reduce the coefficient of friction and therefore limit the degree of heating (e.g., Dengo & Logan, 1981; Goswami & Barbot, 2018). The observation that the highest temperatures are recorded in the highest strained amphibolites closest (0–5 m) to the Tsiknias Thrust and the peak metamorphic assemblages (in the S_{2b} fabrics) are syntectonic with respect to top-to-SW shearing is consistent with the shear heating hypothesis (Wada et al., 2008; Duarte et al., 2015; Edwards et al., 2015; Rice, 2017; Tarling et al., 2018). Furthermore, it is demonstrated that dissipative heating is required to explain the measured heat flow discrepancies in many active steady-state subduction zones (England, 2018), particularly if the mantle wedge had cooled over a long time period. This is further supported by thermal models of subduction zones (Kohn et al., 2018; Peacock, 1992), where it is shown that adding dissipative heating reproduces the *P*–*T* conditions of exhumed high-pressure metamorphic rocks and could increase slab top temperatures by a few hundred degrees (Peacock, 1996).

In summary, we believe that the steep inverted metamorphic gradient recorded in the metamorphic sole is not a diachronous feature and has not been subsequently attenuated. It could be partially explained by incursion of the mantle wedge following subduction initiation; however, shear heating must be important to explain (1) the steep thermal gradient below the Tsiknias Thrust and (2) temperatures >800 °C close to the Tsiknias Thrust that are syntectonic with respect to shearing and correspond to the highest strained rocks.

9.4. Regional Tectonic Framework of Balkan and Aegean Ophiolites

Fitting the Tsiknias Ophiolite into the regional tectonic framework requires an understanding of the origin and emplacement mechanisms of the Western and Eastern Vardar Ophiolite belts. This has been a source of debate over the last three decades, particularly whether these Ophiolite belts represent closure of the same or separate ocean basins (Smith & Spray, 1984; Robertson, 2006). Assuming the single ocean basin and far traveled nappe model of Maffione and van Hinsbergen (2018), whereby both ophiolites originate from the same ocean basin. The West Vardar Ophiolites are interpreted to have formed above an eastward dipping subduction zone off the eastern margin of Adria-Apulia/ Pelagonia during the mid-Jurassic at ~170 Ma and were obducted to the SW onto the Adriatic-Apulian/Pelagonian margin in the latest Jurassic to Early Cretaceous (e.g., Schmid et al., 2008; Brown & Roberson, 2004). Crustal ages of the West Vardar Ophiolites span the latest Bajocian-early Oxfordian (~170–160 Ma) interval based on radiolarian cherts intercalated within the extrusive sequence of the Albanian Mirdita ophiolite (e.g., Chiari et al., 1994; Marcucci et al., 1994;

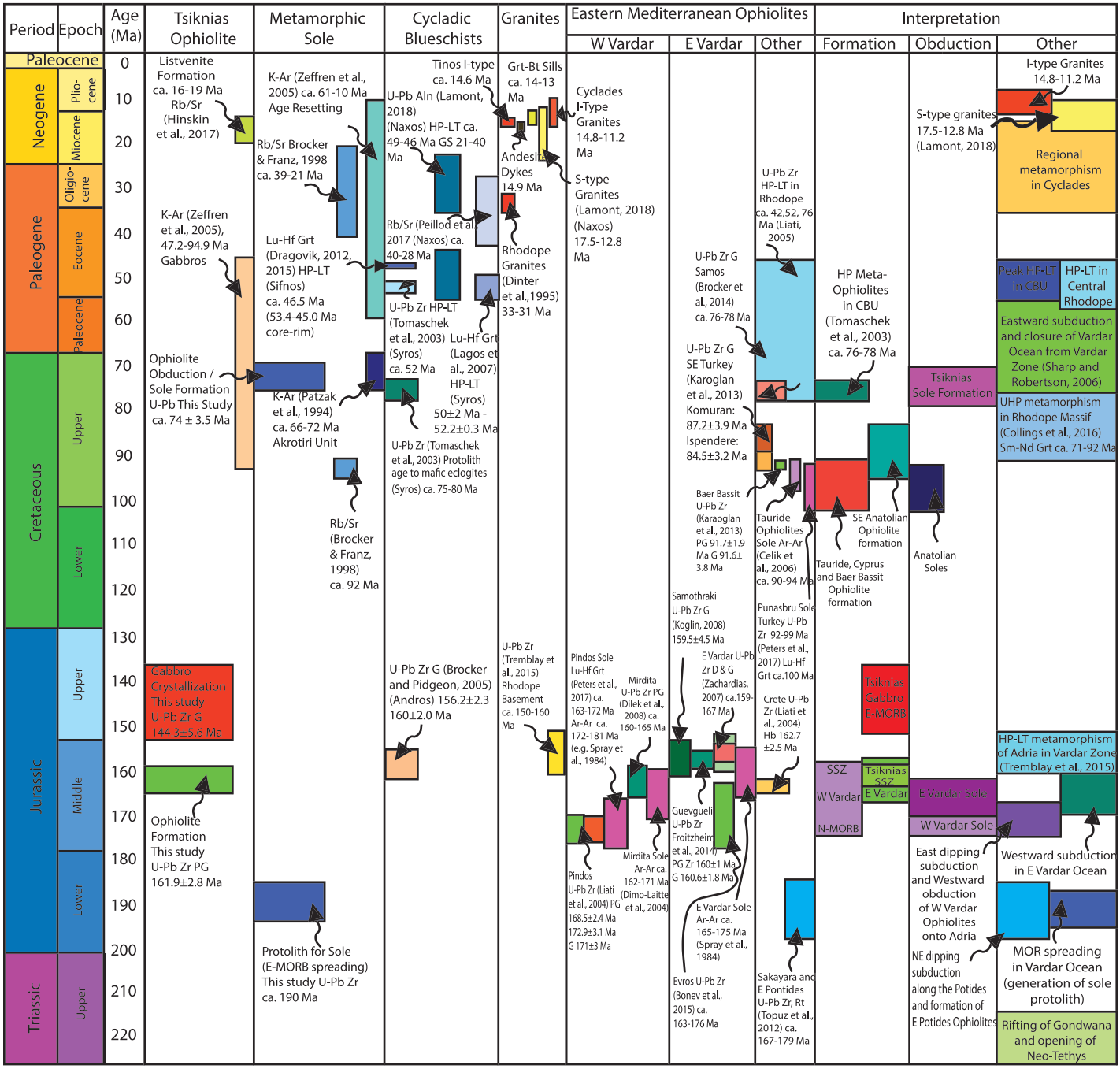

Figure 17. Annotated time chart for the Tsiknias Ophiolite and metamorphic sole with a compilation of literature age data from U-Pb, K-Ar, ^{40}Ar-^{39}Ar, Rb-Sr, and Lu-Hf and Sm-Nd garnet ages. It includes data from granites, the Cycladic Blueschists, and other Eastern Mediterranean Ophiolites to help correlate the reported ages in this study.

Marcucci & Prela, 1996; Prela et al., 2000) and the Vourinos ophiolite of Greece (Chiari et al., 2003; Figures 1 and 17). This age is comparable to zircon U–Pb ages of plagiogranites and gabbros from the Vourinos (172.9 ± 3.1 and 168.5 ± 2.4 Ma) and Pindos (171 ± 3 Ma) ophiolites (Liati et al., 2004; Figures 1 and 19). Metamorphic soles are widespread below the West Vardar Ophiolites and show K–Ar and ^{40}Ar–^{39}Ar hornblende closure temperature ages of ~170 Ma (Dimo-Lahitte et al., 2001; Roddick et al., 1979; Spray & Roddick, 1980; Spray et al., 1984; Sostarić et al., 2014; Figures 1 and 19). These isotopic closure temperature ages in metamorphic soles probably slightly postdate the actual inception of the subduction (van Hinsbergen

et al., 2015), indicating that NE dipping subduction in the Vardar Ocean initiated in the Middle Jurassic, sometime between 175 and 170 Ma (Maffione & van Hinsbergen, 2018). The West Vardar Ophiolites also show a distinct west to east change of geochemical composition and internal structure. The western part of the West Vardar Ophiolites is dominated by fertile lherzolites, locally exposed in relict oceanic core complexes (e.g., Maffione et al., 2013; Tremblay et al., 2009), and a thin crust with high-Ti MOR affinity (Dilek et al., 2008; Saccani & Photiades, 2004), whereas the eastern Mirdita ophiolite has up to 10–12 km in thickness and shows a predominantly SSZ geochemical affinity (Dilek & Furnes, 2009). The oldest magmatic rocks of these ophiolites (Mirdita, Orthis. and Pindos) display moderate to high Ti/V ratios, ranging between 20 and 50, are inconsistent with a significant subduction influence on magma generation (Dilek & Furnes, 2009; Reagan et al., 2010). This strongly suggests that these ophiolites have a MORB affinity and originally represent relics of Neo-Tethyan lithosphere formed prior to Jurassic subduction initiation (Maffione et al., 2015). However, the younger lavas and dykes of basaltic to rhyolitic compositions, show Ti/V ratios between 10 and 20, with some <10, and extremely low Ti and V contents grading into boninites (for the Mirdita ophiolite), suggesting that the youngest magmatic rocks were influenced by subduction (Dilek & Furnes, 2009).

In contrast the East Vardar Ophiolites are interpreted to have formed on the eastern side of the Vardar Ocean and have geochemical compositions that vary from back-arc basin (BAB) affinity in the south (Guevueli ophiolite; Saccani et al., 2008) to a mix of MOR- and SSZ geochemistries that also include boninites in Serbia and Macedonia (Božović et al., 2013; Marroni et al., 2004; Resimić-Šarić et al., 2005, 2006; Šarić et al., 2009). They either formed in a back-arc basin setting (e.g., Guevgeili Ophiolite), above a NE dipping subduction zone between the Paikon Arc and the Eurasian Margin (Ricou & Godfriaux, 1995; Robertson, 2002) or above a westward dipping subduction zone at ~160 Ma, responsible for SSZ signatures and eastward emplacement of ophiolites onto the Eurasian Margin (Maffione & van Hinsbergen, 2018 and references therein). The latter suggestion is the most likely, as continued westward dipping subduction on the eastern side of the Vardar Ocean resulted in high-pressure metamorphism as the Eurasian Margin attempted to subduct at ~150 Ma (Tremblay et al., 2015). Despite the Jurassic-aged deformation, it remains debated when the Eastern Vardar Ophiolites were emplaced either onto the Eurasian margin and whether they were emplaced onto the Adriatic–Apulian (Pelagonian) margin, associated with the closure of the Vardar Ocean as there are no identified metamorphic soles. In contrast Anatolian ophiolites yield Mid Cretaceous ages for formation and obduction, indicating they are not directly related to the East and West Vardar Ophiolites (e.g. Karaoğlan, Parlak, Kloetzli, Koller, et al., 2013; Karaoğlan, Parlak, Kloetzli, Thöni, et al., 2013; Karaoğlan, Parlak, Robertson, et al., 2013; Parlak & Delaloye, 1999)

Integration of our U–Pb and trace element data with this tectonic framework suggests that the Tsiknias Ophiolite must have also originated in an ocean to the northeast of Tinos, and this seaway must have remained open until at least ~74 Ma. The age and SSZ geochemistry of the Tsiknias Ophiolite (~162 Ma) matches Eastern Vardar Ophiolites, thus potentially making it an along-strike equivalent. In this scenario, the Tsiknias Ophiolite may have formed above an along-strike equivalent to the Jurassic age westward dipping subduction zone to explain its SSZ chemistry, but unlike the mainland counterparts further north, this fragment of oceanic lithosphere was not obducted to the east onto the Eurasian margin shortly after it formed. One possibility is that the westward dipping Jurassic subduction zone responsible for its formation initiated at the mid-ocean ridge-transform intersection, and therefore subduction was aligned perpendicular to the spreading axis (E-W; Figure 20). Under these circumstances, the southern portion of the spreading ridge may have survived obduction if the oceanic crust had migrated further south beyond the zone of active subduction. The migration of the ophiolite away from subduction is consistent with the transition from SSZ to BAB and E-MORB gabbro chemistry, with the latter associated with younger ages (144.3 $\pm$ 5.6 Ma). Alternatively, these patterns could also be explained if subduction ceased between ~150 and 144 Ma.

The southwest directed obduction of the Tsiknias Ophiolite and formation of the metamorphic sole at ~74 Ma may have occurred as the southern Vardar Ocean started to close during the Late Cretaceous times, as Africa began to move northward (Vissers & Meijer, 2012); this would have been associated with the development of a Late Cretaceous aged NE dipping subduction system. This is further supported by evidence from along the Paikon and Axion zones, which also suggest that the Vardar Ocean remained open until the Late Cretaceous-Paleogene (Sharp & Robertson, 2006). Recent Lu–Hf and Sm–Nd garnet dating of *(U)–HP* rocks within the Rhodope massif suggest that the Adriatic-Apulian margin attempted to subduct toward the NE

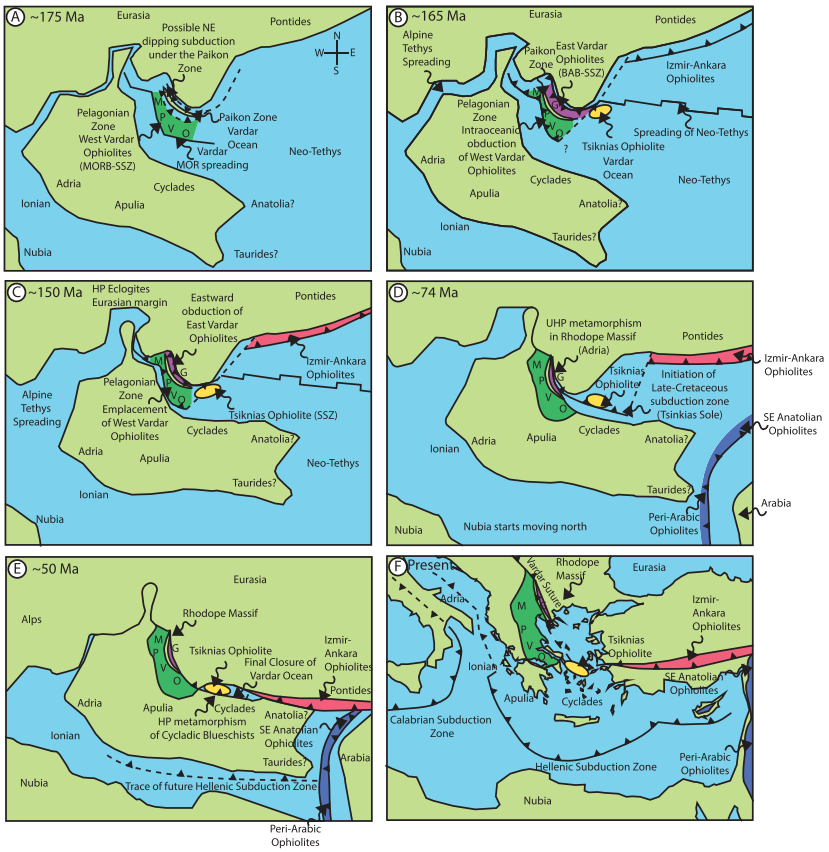

Figure 18. Cartoon paleogeographic reconstruction showing the position of the Tsiknias Ophiolite during the closure of the Vardar Ocean based on data from Maffione and van Hinsbergen (2018) and results from this study. (a) Approximately 175 Ma, MOR spreading the central Vardar Ocean forming MORB signature in the west Vardar Ophiolites, before initiation of eastward dipping subduction zone and obduction of the West Vardar Ophiolites. Possible NE dipping subduction at this time under the Paikon Zone to produce arc volcanism. (b) Approximately 165 Ma showing the position of the Eurasian, Adriatic-Apulian, and Nubian (African) continents and the positions of westward dipping subduction zone (forming the East Vardar Ophiolites) to the west of Eurasia and an east dipping subduction zone to the east of Adria. The location of the MOR ophiolites derived from the Vardar Ocean is shown in stage (a), while these plus the SSZ and BAB ophiolites produced after subduction initiation are shown in stage (b). (c) Approximately 150 Ma, obduction of the West Vardar Ophioites onto Adria-Apulia and eastward obduction of East Vardar Ophiolites on to Eurasia, subsequent *HP* metamorphism of Eurasian margin (Tremblay et al., 2015). Position of Tsiknias to the SE of the East Vardar Ophiolites to the east of the zone of active subduction. (d) Approximately 70 Ma, initiation of new NE dipping subduction zone, obduction of the Tsiknias Ophiolite, sole formation and *UHP* metamorphism of Adria-Apulia rocks in the Rhodope massif (Collings et al., 2016). (e) Approximately 50 Ma, final closure of the Vardar Ocean, *HP* metamorphism of Cycladic Blueschists and emplacement of the Tsiknias ophiolite onto the Cycladic (Adriatic–Apulian) continental margin. Key: Spreading ridges (thick black lines), inferred transform faults (thin dashed black line), trenches (thin line with triangles), and inferred positions of future trenches (dashed lines with triangles) are shown. (f) Present day tectonics. The ophiolite codes are as follows; M = Mirdita ophiolite; G = Guevgueli ophiolite; P = Pindos ophiolite, V = Vourinos ophiolite, and O = Othris ophiolite. The locations of the West Vardar Ophiolite belt (green), East Vardar Ophiolite belt (orange), Izmir-Ankara Ophiolite belt (purple), and Arabic-Tauride Ophiolites (dark blue) are indicated by the thick colored lines. MOR mid-oceanridge; SSZ = suprasubduction zone; BAB = back-arc basin.

beneath Eurasia at ~92–71 Ma (Collings et al., 2016). This is interpreted to record the closure of the Northern Vardar Ocean and precisely correlates with the timing of sole formation on Tinos.

9.5. Relating the Tsiknias Ophiolite and Metamorphic Sole to the Underlying High-Pressure Rocks (Cycladic Blueschist Unit)

The metamorphic sole to the Tsiknias Ophiolite represents moderate to shallow depths (25–30 km) of an infant subduction zone, during which oceanic crust and the overlying pelagic sedimentary cover were underthrusted beneath oceanic crust and mantle (Tsiknias Ophiolite). These rocks are now exposed within 1 km

10.1029/2019TC005677

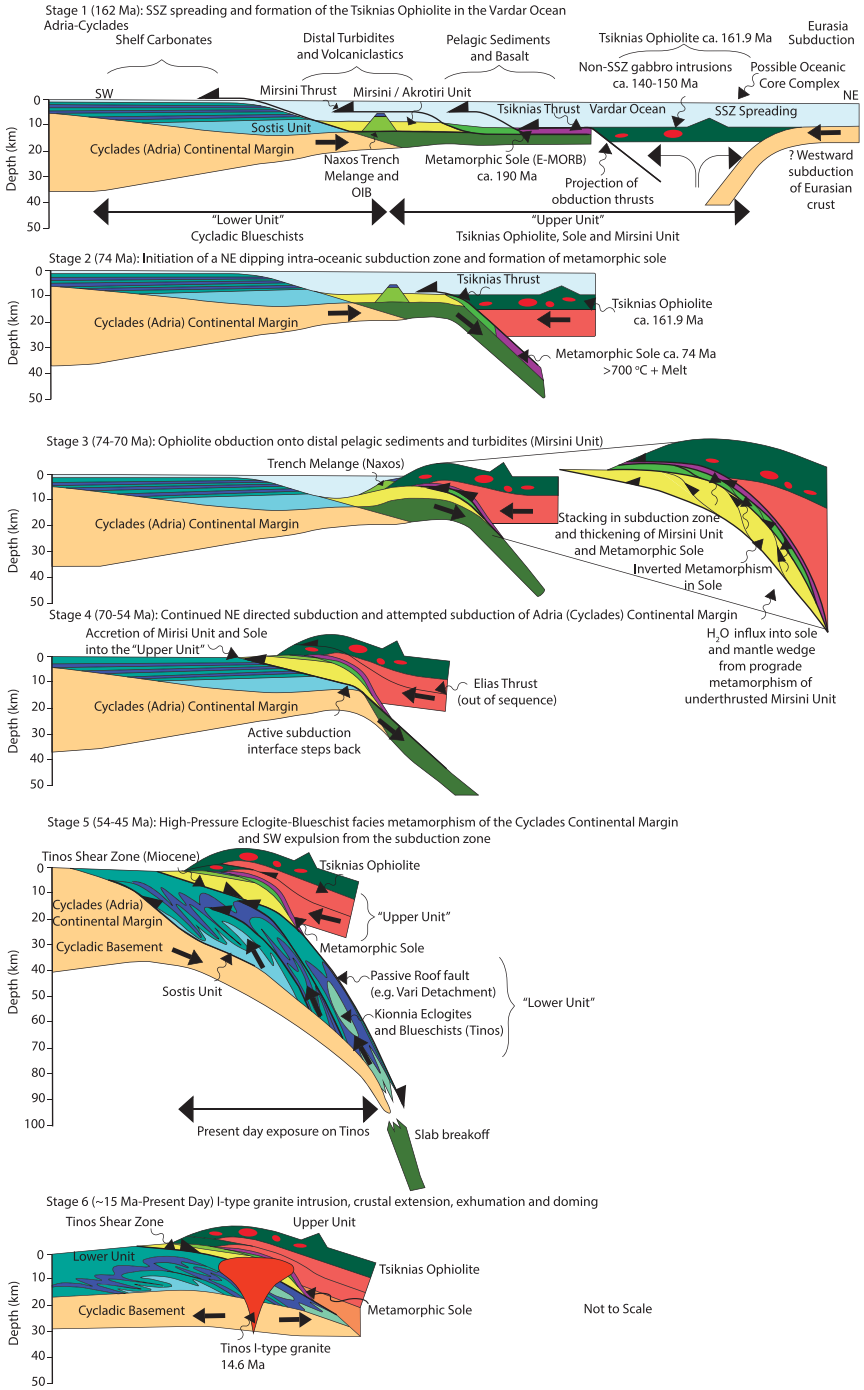

Figure 19. Tectonic model for the formation and emplacement of the Tsiknias Ophiolite, metamorphic sole, and subduction of the NE Cycladic continental margin. Stage 1: ~161.9 Ma: Tsiknias Ophiolite formation above a westward dipping subduction zone, preexisting ~190 Ma E-MORB crust to the SW which is the protolith to the metamorphic sole. Stage 2: ~74 Ma: Initiation of NE dipping subduction zone in ~90 Myr old oceanic crust and sole formation on the subduction interface due to conductive and shear heating. Stage 3: Ophiolite obduction and stacking of Mirsini Unit distal oceanic metasediments beneath the ophiolite. Stage 4: Detachment below the Mirsini Unit and main subduction thrust structurally steps backward. Continued subduction for 25 Myr before arrival of the Cycladic continental margin. Stage 5: Attempted subduction of the Cycladic continental margin at ~52–45 Ma causing high-pressure eclogite and blueschist-facies metamorphism of the Cycladic Blueschists and SW directed extrusion of the Cycladic Blueschists and stacking of the nappe pile. Top-to-NE shear fabrics are preserved at the top of the extruding slab and top-to-SW fabrics record internal thrusting within and at the base of the Cycladic Blueschist Unit. The highest-pressure rocks are preserved at the highest structural level of the Cycladic Blueschists (see Figures 2 and 3) and Laurent et al. (2016). Stage 6: 15 Ma: Present day: Onset of regional extension, I-type granite intrusion, exhumation of the Lower Unit and juxtaposition against the Upper Unit due to movement on the Tinos Shear Zone. E-MORB = enriched mid-ocean ridge basalt.

structurally above high-pressure continental margin-derived metasediments of the Cycladic Blueschists Unit, which also experienced subduction zone metamorphism at ~52–45 Ma (Dragovic et al., 2012, 2015; Lagos et al., 2007; Tomaschek et al., 2003). It therefore seems logical that following intraoceanic ophiolite obduction at ~74 Ma, the underlying high-pressure rocks of the Cycladic Blueschist Unit underwent cold subduction at ~52–45 Ma (e.g., Dragovic et al., 2012, 2015; Lagos et al., 2007; Tomaschek et al., 2003), also down a NE dipping subduction zone. We suggest that this subduction signature recorded by the high pressure to low temperature *HP–LT* rocks is related to the same subduction zone that formed the Tsiknias Ophiolite metamorphic sole, albeit ~ 25 Myr later. This implies that the NE dipping subduction zone responsible for both the metamorphic sole and the underlying high-pressure rocks must have remained static and did not roll back, as both rock types were subducted at different times (~74 and ~52–45 Ma, respectively) but are now preserved adjacent to each other. In contrast, under a scenario of a retreating subduction zone, we would expect the younger *HP–LT* rocks to be located much further south than their current position.

This subduction-obduction process is similar to that recorded in the Oman-UAE, where the As-Sifah eclogites and blueschists within the Arabian continental margin attempted to subduct on the same subduction zone that formed the sole (e.g., Searle et al., 2004). High-pressure metamorphism occurred ~17 Myr after the formation and initial detachment of the Semail Ophiolite (Searle et al., 2004). It suggested the closure of the Northern Vardar Ocean as recent as the Late Cretaceous-Paleogene (Sharp & Robertson, 2006) and 92–71 Ma *(U)–HP* metamorphism associated with attempted NE dipping continental subduction under Eurasia (Collings et al., 2016). In this scenario, the same Late Cretaceous to Eocene subduction zone to that recorded on Tinos continued along the entire western margin of the Vardar Ocean (striking NNE to SSW today) and was responsible for the collision with Eurasia to the NE and Cyclades (Adria-Apulia) to the SW producing what has been termed the Aegean Orogeny (Lamont et al., 2019). The Cycladic Blueschists could not have been subducted on the current Hellenic subduction zone, but this earlier Cretaceous-Eocene subduction system terminated following final closure of the Vardar Ocean at ~52–45 Ma and subsequent collision between Eurasia and Cyclades (Adria-Apulia).

10. Tectonic Model and Conclusions

The data presented and discussed above can be described in the following tectonic interpretation. A cartoon paleogeographic reconstruction of the closure of Vardar Ocean based on data from Maffione and van Hinsbergen (2018) is presented in Figure 18 and a simplified tectonic model of the Tsiknias Ophiolite in Figure 19.

1. Formation of the Tsiknias Ophiolite at ~162 Ma occurred due to SSZ spreading above a subduction zone to the NE of Tinos in present-day coordinates (Figure 19—Stage 1). The Tsiknias Ophiolite can be correlated both geochronologically and geochemically with the Eastern Vardar Ophiolites of mainland Greece and Macedonia that formed above a westward dipping subduction zone on the eastern side of the Vardar Ocean (off the western margin of Eurasia). We interpret the Jurassic subduction zone responsible for SSZ spreading of the Tsiknias Ohiolite to be equivalent to the inferred westward dipping subduction zone on the eastern side of the Vardar Ocean forming the East Vardar Ophiolites. E-type MORB gabbros which intrude the Tsiknias Ophiolite are associated with younger ages of ~144 Ma, suggesting that the later stages of Tsiknias Ophiolite spreading was not affiliated with subduction. The lower-plate material in the metamorphic sole is geochemically and petrologically distinct from all the rocks within the Tsiknias sequence. The lower-plate amphibolite protoliths and pelagic metasediments must have formed further westward potentially in the interior of the Vardar Ocean at ~190 Ma in an E-MORB to BAB setting as revealed by zircon core ages and trace element data. The metabasalts on Naxos (Lamont et al., 2019) also do not belong to the ophiolite sequence and have ocean island basalt affinities, they therefore also formed on the lower plate prior to obduction. However, the metabasalts on Paros and Samos could potentially represent the upper crust of the Tsiknias Ophiolite.
2. Unlike the East Vardar Ophiolites, the Tsiknias Ophiolite was not obducted at the time it formed and remained as a piece of cooling oceanic crust for ~90 Myr. At ~74 Ma, a new NE dipping intraoceanic subduction zone initiated within old cold ~190 Ma oceanic crust (the metamorphic sole protolith), potentially in a similar fashion to the Gorringe Bank intraoceanic thrust today (Figure 19—Stage 2). This subduction zone may have initiated due to a change in regional tectonic stresses as the African plate began to move northward (Vissers & Meijer, 2012). The metamorphic sole formed on the subduction

interface along the leading edge of the downgoing (~190 Ma) piece of oceanic crust. The metamorphic sole formed at ~74.0 ± 3.5 Ma attained upper amphibolite-facies anatectic conditions of ~8.5 kbar and 850 °C. Thermal conduction from the adjacent mantle is insufficient to explain such temperatures and calls for other heating mechanisms. It is possible that shearing provided an additional heating contribution to generate upper amphibolite facies temperatures and a steep inverted metamorphic field gradient below the Tsiknias Thrust.

3. During the initial stages of SW directed obduction, the metamorphic sole was accreted to the base of the ophiolite in the upper plate, and the Mirsini Unit pelagic metasediments were underthrusted and attained amphibolite facies conditions of ~8.5 kbar, 600–660 °C (Figure 19—Stage 3). During this process, prograde dehydration reactions within the Mirsini Unit metsediments hydrated the overlying rocks. Alkali and OIB basalts and marble "exotics" preserved on Naxos, that represented off-shore seamounts on the subducting plate, were underthrusted to shallow depths. This process formed trench mélange that is exposed on Naxos (Lamont et al., 2019), similar to the Haybi complex under the Oman/UAE ophiolite (Searle et al., 2004).
4. The Mirsini Unit, metamorphic sole, and Tsiknias Ophiolite together were accreted to become part of the upper plate, and the main subduction interface must have stepped back. NE directed subduction continued between ~74 and 54 Ma, before the arrival of the leading edge of the Cycladic continental margin (to the SW; representing the NE margin of Adria-Apulia). Out of sequence thrusts such as the Elias Thrust structurally thickened the Tsiknias Ophiolite, metamorphic sole, and Mirsini Unit during the later stages of the obduction process (Figure 19—Stage 4).
5. Attempted subduction of the Cycladic continental margin at ~52–45 Ma was associated with eclogite-blueschist-facies metamorphism and is recorded within the Tinos Lower Unit and the Cycladic Blueschist Unit (Figure 19—Stage 5). These rocks reached *P–T* conditions of ~22–24 kbars and 550 °C (Laurent et al., 2018), representing depths of up to 80 km, before extruding to the SW bounded by passive roof normal sensed top-to-NE sense shear zones at the top (e.g., Vari Detachment) and top-to-SW thrusts at the base (e.g., Laurent et al., 2018). This represents the final closure of the Vardar Ocean, and during this stage, the Tsiknias Ophiolite, metamorphic sole, and Mirsini Unit would have been thrust to the SW onto the depressed and underthrusted Cycladic (Adriaic–Apulian) continental margin. Following extrusion from 80-km depth and upon reaching mid-crustal depths later in the orogenic history, these high-pressure rocks were then juxtaposed against the Upper Unit by the greenschist-facies top-to-NE shear zone (The Tinos Shear Zone) active during the Miocene (Figure 19—Stage 5), although it remains debated whether this structure was active during regional extension or during a phase synorogenic extrusion (Searle & Lamont, 2019).
6. The onset of regional extension, exhumation, and the intrusion of the Tinos I-type granite intruded at ~14.6 Ma (Brichau et al., 2007; Figure 19—Stage 6). A component of E-W shortening caused upright folding during the Miocene that affected all units and folded the detachments. Leucogranite sills intrude the metamorphic sole at Livada Bay. Domino-style brittle normal faults associated with regional extension clearly cut these sills, indicating the timing of extension in the brittle crust must immediately postdate intrusion at ~14 Ma.

This subduction-obduction process between ~74 and 45 Ma marks the first stages of the Aegean Orogeny. We believe this event records the final closure of the southern Vardar Ocean to the NE of the Cyclades during the Late Cretaceous-Eocene associated with the transition in Nubia's motion from transcurrent (E-W) to convergent (N-S; Vissers & Meijer, 2012). This interpretation agrees with geological evidence from mainland Greece (Collings et al., 2016; Sharp & Robertson, 2006) where it is suggested that the northern part of Vardar Ocean remained as an open seaway until at least the Late Cretaceous time before NE directed subduction under Eurasia, subsequent *(U)–HP* metamorphism, and finally continental collision. Previous models of continuous slab rollback and extension in the Aegean since 70 Ma (Jolivet & Brun, 2010; Jolivet et al., 2013) should therefore be reexamined considering these new data.

Acknowledgments
This work forms part of Thomas Lamont's D.Phil project funded by the Natural Environment Research Council (Grant NE/L0021612/1). University College Oxford are thanked for providing a travel grant to help fund fieldwork and the University of Oxford are thanked for covering publication costs. Analytical work at the NERC Isotope Geosciences Laboratory was funded by NIGFSC Grant IP-1597-1115. Data used in this study are deposited in the Oxford University Research Archive, available using this URL (https://ora.ox.ac.uk). We thank Philip England, Lars Hansen, Tyler Ambrose, Jacob Forshaw, Andrew Parsons, Chris Ballhaus, and Anthony Watts for thought-provoking and critical discussion. We extend thanks to Marc St-Onge, Owen Weller, and Anna Bidgood for assistance and discussion in the field, Adrian Wood for assistance with mineral separation. Owen Green and Jonathon Wells for advice preparing samples and helping prepare thin sections. Philip Holdship, Steven Wyatt, and Stanley Mertzman are thanked for helping with preparation and overseeing ICP-MS trace element and XRF analysis. The authors thank the Editor Lauren Jolivet, Associate Editor Federico Rossetti, and Fernando Corfu, Uwe Ring, Harold Furnes, and two anonymous reviewers for critical and helpful reviews of an earlier version of the manuscript.

References

Ambrose, T. K., & Searle, M. P. (2019). 3-D structure of the northern Oman-UAE ophiolite: Widespread, short-lived, suprasubduction zone magmatism. *Tectonics*, *38*, 233–252. https://doi.org/10.1029/2018TC005038

Anderson, J. L., & Smith, D. R. (1995). The effects of temperature and f O2 on the Al-in-hornblende barometer. *American Mineralogist*, *80*(5–6), 549–559.

Avigad, D., & Garfunkel, Z. (1989). Low-angle faults above and below a blueschist belt—Tinos Island, Cyclades, Greece. *Terra Nova*, *1*, 182–187.

Avigad, D., & Garfunkel, Z. (1991). Uplift and exhumation of high-pressure metamorphic terrains: the example of the Cycladic blueschist belt (Aegean Sea). *Tectonophysics*, *188*, 357–372.

Bortolotti, V., Chiari, M., Marroni, M., Pandolfi, L., Principi, G., & Saccani, E. (2013). Geodynamic evolution of ophiolites from Albania and Greece (Dinaric-Hellenic belt): One, two, or more oceanic basins? *International Journal of Earth Sciences*, *102*(3), 783–811. https://doi.org/10.1007/s00531-012-0835-7

Bosse, V., & Villa, I. M. (2019). Petrochronology and hygrochronology of tectono-metamorphic events. *Gondwana Research*, *71*, 76–90. https://doi.org/10.1016/j.gr.2018.12.014

Božović, M., Prelević, D., Romer, R. L., Barth, M., van Den Bogaard, P., & Boev, B. (2013). The demir kapija ophiolite, Macedonia (FYROM): A snapshot of subduction initiation within a back-arc. *Journal of Petrology*, *54*, 1399–1425. https://doi.org/10.1093/petrology/egt016

Brichau, S., Ring, U., Carter, A., Monié, P., Bolhar, R., Stockli, D., & Brunel, M. (2007). Extensional faulting on Tinos Island, Aegean Sea, Greece: How many detachments? *Tectonics*, *26*, TC4009. https://doi.org/10.1029/2006TC001969

Bröcker, M., & Franz, L. (1998). Rb–Sr isotope studies on Tinos Island (Cyclades, Greece): additional time constraints for metamorphism, extent of infiltration-controlled overprinting and deformational activity. *Geological Magazine*, *135*, 369–382.

Bröcker, M., & Franz, L. (2000). Contact metamorphism on Tinos (Cyclades, Greece): The importance of tourmaline, timing of the thermal overprint and Sr isotope characteristics. *Mineralogy and Petrology*, *70*, 257–283.

Bröcker, M., Kreuzer, A., Matthews, A., & Okrusch, M. (1993). $^{40}Ar/^{39}Ar$ and oxygen isotope studies of poly-metamorphism from Tinos Island, Cycladic blueschist belt, Greece. *Journal of Metamorphic Geology*, *11*, 223–240.

Bröcker, M., Löwen, K., & Rodionov, N. (2014). Unraveling protolith ages of meta-gabbros from Samos and the Attic–Cycladic Crystalline Belt, Greece: Results of a U–Pb zircon and Sr–Nd whole rock study. *Lithos*, *198*, 234–248. https://doi.org/10.1016/j.lithos.2014.03.029

Brown, S. A. M., & Robertson, A. H. F. (2004). Evidence for Neotethys rooted within the Vardar suture zone from the Voras Massif, northernmost Greece. *Tectonophysics*, *381*(1-4), 143–173. https://doi.org/10.1 016/j.tecto.2002.06.001

Cabanis, B., & Lecolle, M. (1989). The La/10-Y/15-Nb/ 8 diagram: A tool for discriminating volcanic series and evidencing continental crust magmatic mixtures and/ or contamination. *C. R. Academic Science Series II*, *309*, 2023–2029.

Carson, C. J., Powell, R., & Clarke, G. L. (1999). Calculated mineral equilibria for eclogites in CaO–Na2O–FeO–MgO–Al2O3–SiO2–H2O: Application to the Pouebo Terrane, PamPeninsula, New Caledonia. *Journal of Metamorphic Geology*, *17*, 9–2.

Casey, J. F., & Dewey, J. F. (1984). Initiation of subduction zones along transform and accreting plate boundaries, triple-junction evolution, and forearc spreading centers— Implications for ophiolitic geology and obduction. *Geological Society, London, Special Publications*, *13*, 269–290.

Çelik, Ö. F., Delaloye, M., & Feraud, G. (2006). Precise $^{40}Ar–^{39}Ar$ ages from the metamorphic sole rocks of the Tauride Belt Ophiolites, southern Turkey: Implications for the rapid cooling history. *Geological Magazine*, *143*(02), 213. https://doi.org/10.1017/S0016756805001524

Chiari, M., Bortolotti, V., Marcucci, M., Photiades, A., & Principi, G. (2003). The middle Jurassic siliceous sedimentary cover at the top of the vourinos ophiolite (Greece). *Ofioliti*, *28*(2), 95–103.

Chiari, M., Marcucci, M., & Prela, M. (1994). Mirdita ophiolites project: 2 radiolarian assemblages in the cherts at Fushe Arrez and Shebaj (Mirdita area, Albania). *Ofioliti*, *19*(2).

Coleman, R. G., & Donato, M. M. (1979). Oceanic plagiogranite revisited. *Developments in petrology*, *6*, 149–168.

Coleman, R. G., & Peterman, Z. E. (1975). Oceanic plagiogranite. *Journal of Geophysical Research*, *80*(8), 1099–1108. https://doi.org/10.1029/JB080i008p01099

Collings, D., Savov, I., Maneiro, K., Baxter, E., Harvey, J., & Dimitrov, I. (2016). Late Cretaceous UHP metamorphism recorded in kyanite–garnet schists from the Central Rhodope Mountains, Bulgaria. *Lithos*, *246–247*, 165–181. https://doi.org/10.1016/j.lithos.2016.01.002

Corfu, F., Hanchar, J. M., Hoskin, P. W. O., & Kinny, P. (2003). Atlas of Zircon Textures. *Reviews in Mineralogy and Geochemistry*, *53*, 469–500. https://doi.org/10.2113/0530469

Cowan, R. J., Searle, M. P., & Waters, D. J. (2014). Structure of the metamorphic sole to the Oman Ophiolite, Sumeini Window and Wadi Tayyin: Implications for ophiolite obduction processes. *Geological Society, London, Special Publications*, *392*, 155–175.

Danelian, T., Robertson, A. H. F., & Dimitriadis, S. (1996). Age and significance of radiolarian sediments within basic extrusives of the marginal basin Guevgueli Ophiolite (northern Greece). *Geological Magazine*, *133*, 127–136. https://doi.org/10.1017/S0016756800008645

Del Gaudio, P., Di Toro, G., Han, R., Hirose, T., Nielsen, S., Shimamoto, T., & Cavallo, A. (2009). Frictional melting of peridotite and seismic slip. *Journal of Geophysical Research: Solid Earth*, *114*(B6).

Dengo, C. A., & Logan, J. M. (1981). Implications of the mechanical and frictional behavior of serpentinite to seismogenic faulting. *Journal of Geophysical Research*, *86*, 10771–10782. https://doi.org/10.1029/JB086iB11p10771

Dewey, J. F., & Casey, J. F. (2011). The origin of obducted large-slab ophiolite complexes. In *Arc-continent collision*, (pp. 431–444). Berlin Heidelberg: Springer.

Dilek, Y., & Furnes, H. (2009). Structure and geochemistry of Tethyan ophiolites and their petrogenesis in subduction rollback systems. *Lithos*, *113*(1-2), 1–20.

Dilek, Y., & Furnes, H. (2011). Ophiolite genesis and global tectonics: Geochemical and tectonic fingerprinting of ancient oceanic lithosphere. *Bulletin, v.*, *123*(3-4), 387–411.

Dilek, Y., & Furnes, H. (2014). Ophiolites and their origins. *Elements*, *10*(2), 93–100.

Dilek, Y., Furnes, H., & Shallo, M. (2007). Suprasubduction zone ophiolite formation along the periphery of Mesozoic Gondwana. *Gondwana Research*, *11*, 453–475.

Dilek, Y., Furnes, H., & Shallo, M. (2008). Geochemistry of the Jurassic Mirdita Ophiolite (Albania) and the MORB to SSZ evolution of a marginal basin oceanic crust. *Lithos*, *100*(1–4), 174–209.

Dilek, Y., & Thy, P. (2009). Island arc tholeiite to boninitic melt evolution of the Cretaceous Kizildag (Turkey) ophiolite: Model for multi-stage early arc-forearc magmatism in Tethyan subduction factories. *Lithos*, *113*, 68–87.

Dimo-Lahitte, A., Monié, P., & Vergély, P. (2001). Metamorphic soles from the Albanian ophiolites: Petrology, $^{40}Ar/^{39}Ar$ geochronology, and geodynamic evolution. *Tectonics*, *20*(1), 78–96. https://doi.org/10.1029/2000TC900024

Dinter, D. A., Macfarlane, A., Hames, W., Isachsen, C., Bowring, S., & Royden, L. (1995). U-Pb and $^{40}Ar/^{39}Ar$ geochronology of the Symvolon granodiorite: Implications for the thermal and structural evolution of the Rhodope metamorphic core complex, northeastern Greece. *Tectonics*, *14*(4), 886–908. https://doi.org/10.1029/95TC00926

Dixon, S., & Rutherford, M. J. (1979). Plagiogranites as late-stage immiscible liquids in ophiolite and mid-ocean ridge suites: An experimental study. *Earth and Planetary Science Letters*, *45*, 45–60.
Dragovic, B., Baxter, E. F., & Caddick, M. J. (2015). Pulsed dehydration and garnet growth during subduction revealed by zoned garnet geochronology and thermodynamic modeling Sifnos, Greece. *Earth and Planetary Science Letters*, *413*, 111–122, ISSN 0012-821X. https://doi.org/10.1016/j.epsl.2014.12.024
Dragovic, B., Samanta, L. M., Baxter, E. F., & Selverstone, J. (2012). Using garnet to constrain the duration and rate of water-releasing metamorphic reactions during subduction: An example from Sifnos. *Greece. Chemical Geology*, *314–317*, 9–22, ISSN 0009-2541. https://doi.org/10.1016/j.chemgeo.2012.04.016
Duarte, J. C., Schellart, W. P., & Cruden, A. R. (2015). How weak is the subduction zone interface? *Geophysical Research Letters.*, *42*, 2664–2673. https://doi.org/10.1002/2014GL062876
Eby, N. (1973). Scandium Geochemistry of the Oka Carbonatite Complex, Oka, Quebec. *American Mineralogist*, *58*, 819–825.
Edwards, S. J., Schellart, W. P., & Duarte, J. C. (2015). Geodynamic models of continental subduction and obduction of overriding plate forearc oceanic lithosphere on top of continental crust. *Tectonics*, *34*, 1494–1515. https://doi.org/10.1002/2015TC003884
England, P. (2018). On shear stresses, temperatures, and the maximum magnitudes of earthquakes at convergent plate boundaries. *Journal of Geophysical Research: Solid Earth*, *123*(8), 7165–7202.
England, P., & Molnar, P. (1993). The interpretation of inverted metamorphic isograds using simple physical calculations. *Tectonics*, *12*, 145–157.
Ferriére, J. (1982). Paléogéographie et tectonique superpose oes dans les Hellenides internes: Les massifs de l'Othrys et du Pélion (Gréce septentrionale). *Société de la Géologie du Nord*, *8*, 1–970.
Floyd, P. A., Göncüoğlu, M. C., Winchester, J. A., & Yaliniz, M. K. (2000). Geochemical character and tectonic environment of Neotethyan ophiolitic fragments and metabasites in the Central Anatolian Crystalline Complex, Turkey. *Geological Society, London, Special Publications*, *173*(1), 183–202.
Froitzheim, N., Jahn-Awe, S., Frei, D., Wainwright, A. N., Maas, R., Georgiev, N., et al. (2014). Age and composition of meta-ophiolite from the Rhodope Middle Allochthon (Satovcha, Bulgaria) A test for the maximum-allochthony hypothesis of the Hellenides. *Tectonics*, *32*, 1477–1500. https://doi.org/10.1002/2014TC003526
Furnes, H., & Dilek, Y. (2017). Geochemical characterization and petrogenesis of intermediate to silicic rocks in ophiolites: A global synthesis. *Earth-Science Reviews*, *166*, 1–37.
Furnes, H., De Wit, M., & Dilek, Y. (2014). Four billion years of ophiolites reveal secular trends in oceanic crust formation. *Geoscience Frontiers, v.*, *5*(4), 571–603.
Gerlach, D. C., Leeman, W. P., & Lallemant, H. G. A. (1981). Petrology and geochemistry of plagiogranite in the Canyon Mountain Ophiolite, Oregon. *Contributions to Mineralogy and Petrology*, *77*(1), 82–92.
Gerya, T., & Stöckhert, B. (2006). Two-dimensional numerical modeling of tectonic and metamorphic histories at active continental margins. *International Journal of Earth Sciences*, *95*(2), 250–274.
Gnos, E., & Peters, T. (1993). K-Ar ages of the metamorphic sole of the Semail Ophiolite: implications for ophiolite cooling history. *Contributions to Mineralogy and Petrology*, *113*, 325–332.
Goswami, A., & Barbot, S. (2018). Slow-slip events in semi-brittle serpentinite fault zones. *Nature Scientific reports*, *8*(1), 6181. https://doi.org/10.1038/s41598-018-24637-z
Graham, C. M., & England, P. C. (1976). Thermal regimes and regional metamorphism in the vicinity of overthrust faults: an example of shear heating and inverted metamorphic zonation from southern California. *Earth and Planetary Science Letters*, *31*(1), 142–152.
Green, E. C. R., White, R. W., Diener, J. F. A., Powell, R., Holland, T. J. B., & Palin, R. M. (2016). Activity-composition relations for the calculation of partial melting equilibria in metabasic rocks. *Journal of Metamorphic Geology*, *34*(9), 845–869.
Henry, D. J., Guidotti, C. V., & Thomson, J. A. (2005). The Ti-saturation surface for low-to-medium pressure metapelitic biotites: Implications for geothermometry and Ti-substitution mechanisms. *American Mineralogist*, *90*(2–3), 316–328.
Hacker, B. R. (1990). Simulation of the metamorphic and deformational history of the metamorphic sole of the Oman ophiolite. *Journal of Geophysical Research*, *95*, 4895–4907.
Hacker, B. R., & Gnos, E. (1997). The conundrum of Samail: Explaining the metamorphic history. *Tectonophysics*, *279*, 215–226.
Hacker, B. R., Mosenfelder, J. L., & Gnos, E. (1996). Rapid emplacement of the Oman ophiolite: thermal and geochronologic constraints. *Tectonics*, *15*, 1230–1247.
Harris, N. B., Kelley, S., & Okay, A. I. (1994). Post-collision magmatism and tectonics in northwest Anatolia. *Contribution to Mineralogy and Petrology*, *117*, 241–252.
Hayward, N., Watts, A., Westbrook, G., & Collier, J. (1999). A seismic reflection and GLORIA study of compressional deformation in the Gorringe Bank region, eastern North Atlantic. *Geophysics Journal International*, *138*, 831–850.
Holland, T., & Blundy, J. (1994). Non-ideal interactions in calcic amphiboles and their bearing on amphibole-plagioclase thermometry. *Contributions to Mineralogy and Petrology*, *116*, 433. https://doi.org/10.1007/BF00310910
Holland, T. J. B., (2009), AX: A program to calculate activities of mineral end-members from chemical analyses. Available at: http://www.esc.cam.ac.uk/research/research-groups/holland/ax (last accessed on 6th June 2018).
Holland, T. J. B., & Powell, R. (2011). An improved and extended internally consistent thermodynamic dataset for phases of petrological interest, involving a new equation of state for solids. *Journal of Metamorphic Geology*, *29*, 333–383.
Horstwood, M. S. A., Košler, J., Gehrels, G., Jackson, S. E., McLean, N. M., Paton, C., et al. (2016). Community-derived standards for LA-ICP-MS U-(Th-)Pb geochronology—Uncertainty propagation, age interpretation and data reporting. *Geostandard Geoanalytical Research*, *40*, 311–332. https://doi.org/10.1111/j.1751-908X.2016.00379.x
Jansen, J. B. H., (1973), Geological map of Greece, Island of Naxos, Institute for Geology and Mineral Resources, Athens.
Jansen, J. B. H., & Schuiling, R. D. (1976). Metamorphism on Naxos: Petrology and geothermal gradients. *American Journal of Science*, *276*, 1225–1253. https://doi.org/10.2475/ajs.276.10.1225.
Jiménez-Munt, I., Fernàndez, M., Vergés, J., Afonso, J. C., Garcia-Castellanos, D., & Fullea, J. (2010). Lithospheric structure of the Gorringe Bank: Insights into its origin and tectonic evolution. *Tectonics*, *29*, TC5019. https://doi.org/10.1029/2009TC002458
Jolivet, L., & Brun, J. P. (2010). Cenozoic geodynamic evolution of the Aegean region. *International Journal of Earth Sciences*, *99*, 109–138. https://doi.org/10.1007/s00531-008-0366-4
Jolivet, L., Faccenna, C., Huet, B., Labrousse, L., Le Pourhiet, L., Lacombe, O., et al. (2013). Aegean tectonics: Strain localisation, slab tearing and trench retreat. *Tectonophysics*, *597–598*, 1–33.
Jolivet, L., Famin, V., Mehl, C., Parra, T., Aubourg, C., Hébert, R., & Philippot, P. (2004). Strain localization during crustal-scale boudinage to form extensional metamorphic domes in the Aegean Sea, Special Paper. *Geological Society of America*, *380*, 185–210.

Jolivet, L., Lecomte, E., Huet, B., Denèle, Y., Lacombe, O., Labrousse, L., et al. (2010). The North Cycladic Detachment System. *Earth and Planetary Science Letters*, *289*, 87–104. https://doi.org/10.1016/j.epsl.2009.1010.1032.

Jones, G., & Robertson, A. H. (1991). Tectono-stratigraphy and evolution of the Mesozoic Pindos ophiolite and related units, northwestern Greece. *Journal of the Geological Society of London*, *148*(2), 267–288. https://doi.org/10.1144/gsjgs.148.2.0267

Karaoğlan, F., Parlak, O., Kloetzli, U., Koller, F., & Rızaoğlu, T. (2013). Age and duration of intra-oceanic arc volcanism built on a suprasubduction zone type oceanic crust in Southern Neotethys, SE Anatolia. *GeoScience Frontiers*, *4*, 399–408.

Karaoğlan, F., Parlak, O., Kloetzli, U., Thöni, M., & Koller, F. (2013). U–Pb and Sm–Nd geochronology of the Kızıldağ (Hatay, Turkey) ophiolite: Implications for the timing and duration of suprasubduction zone type oceanic crust formation in southern Neotethys. *Geological Magazine*, *150*, 283–299.

Karaoğlan, F., Parlak, O., Robertson, A. H. F., Thöni, M., Klötzli, U., Koller, F., & Okay, A. I. (2013). Eocene HT/ HP metamorphism of ophiolitic rocks and Eocene crosscutting granitoid intrusions (Doğanşehir, area SE Anatolia) related to late-stage Neotethyan subduction processes. In A. H. F. Robertson, O. Parlak, & U. C. Ünlügenç (Eds.), *Geological development of Anatolia and the Easternmost Mediterranean Region*, *Geological Society: London. Special Publication*, (Vol. 372, pp. 249–272).

Katzir, Y., Garfunkel, Z., Avigad, D., & Matthews, A. (2007). Emplacement of ultramafic rocks (Aegean Sea, Greece): Insights from diverse origins and modes of The geodynamic evolution of the Alpine orogen in the Cyclades. *Geological Society, London, Special Publications*, *291*, 17–40.

Katzir, Y., John, E., Valley, W., Matthews, A., & Spicuzza, M. J. (2002). Tracking fluid flow during deep crustal anatexis: Metasomatism of peridotites (Naxos, Greece). *Contributions to Mineral Petrology*, *142*, 700–713. https://doi.org/10.1007/s00410-001-0319-4

Katzir, Y., Matthews, A., Garfunkel, Z., Schliestedt, M., & Avigad, D. (1996). The tectono-metamorphic evolution of a dismembered ophiolite (Tinos, Cyclades, Greece). *Geological Magazine*, *133*, 237–254. https://doi.org/10.1017/S0016756800008992

Keay, S., Lister, G., & Buick, I. (2001). The timing of partial melting, Barrovian metamorphism and granite intrusion in the Naxos metamorphic core complex, Cyclades, Aegean Sea, Greece. *Tectonophysics*, *342*, 275–312. https://doi.org/10.1016/S0040-1951(01)00168-8

Kelley, S. (2002). Excess argon in K-Ar and Ar-Ar geochronology. *Chemical Geology*, *188*, 1–22. https://doi.org/10.1016/S0009-2541(02)00064-5

Klein, E. M. (2004). Geochemistry of the igneous oceanic crust. In H. D. Holland, & K. K. Turekian (Eds.), *Treatise on Geochemistry*, (Vol. 3, pp. 433–463). Amsterdam: Elsevier.

Koglin, N., (2008). Geochemistry, petrogenesis and tectonic setting of Ophiolites and mafic-ultramafic complexes in the Northeastern Aegean Region: New trace-element, isotopic and age constraints (PhD thesis). Mainz, Germany.

Koglin, N., Kostopoulos, D., & Reichmann, T. (2009). Reichmann, Geochemistry, petrogenesis and tectonic setting of the Samothraki mafic suite, NE Greece: Trace-element, isotopic and zircon age constraints. *Tectonophysics*, *473*, 53–68. https://doi.org/10.1016/j.tecto.2008.10.028

Kohlstedt, D. L., & Holtzman, B. K. (2009). Shearing melt out of the Earth: An experimentalist's perspective on the influence of deformation on melt extraction. *Annual Review of Earth and Planetary Sciences 37*, 561–593.

Kohn, M. J., Castro, A. E., Kerswell, B. C., Ranero, C. R., & Spear, F. S. (2018). Shear heating reconciles thermal models with the metamorphic rock record of subduction. *PNAS*, *115*(46), 11706–11711. https://doi.org/10.1073/pnas.1809962115

Konstantinou, A., Wirth, K. R., & Vervoort, J., (2007). U–Pb ısotopic dating of Troodos plagiogranite, Cyprus by LAICP-MS/. GSA Denver Annual Meeting, Denver, CO

Kukoč, D., Goričan, Š., Košir, A., Belak, M., Halamić, J., & Hrvatović, H. (2015). Middle Jurassic age of basalts and the post-obduction sedimentary sequence in the Guevgueli Ophiolite Complex (Republic of Macedonia). *International Journal of Earth Sciences*, *104*(2), 435–447.

Lagos, M., Scherer, E. E., Tomaschek, F., Munker, C., Keiter, M., Berndt, J., & Ballhaus, C. (2007). High precision Lu-Hf geochronology of Eocene eclogite-facies rocks from Syros, Cyclades Greece. *Chemical Geology*, *24*, 16–35.

Lamont, T. N. (2018). Unravelling the structural, metamorphic and strain history of the Aegean Orogeny, Southern Greece, with a combined structural, petrological and geochronological approach. *PhD Thesis*, Universisity of Oxford. Available at https://ora.ox.ac.uk/objects/uuid:46678b24-156d-4579-b758-e91834fb3236

Lamont, T. N., Searle, M. P., Roberts, N. M. W., Waters, D. W., Palin, R. M., Dyck, B., et al. (2019). Compressional origin of the Naxos metamorphic core complex: structure, petrography and thermobarometry. *Geological Society of America Bulletin.*. https://doi.org/10.1130/B31978.1

Laurent, v., Jolivet, L., Roche, V., Augier, R., Scaillet, S.,Cardello, G. L. (2016). Strain localization in a fossilized subduction channel: Insights from the Cycladic Blueschist Unit (Syros, Greece). *Tectonophysics*, *672–673*, 150–169. https://doi.org/10.1016/j.tecto.2016.01.036

Laurent, V., Lanari, P., Naïr, I., Augier, R., Lahfid, A., & Jolivet, L. (2018). Exhumation of eclogite and blueschist (Cyclades, Greece): Pressure-temperature evolution determined by thermobarometry and garnet equilibrium modelling. *Journal of metamorphic geology*, *36*(6), 769–798.

Leloup, P. H., Ricard, Y., Battaglia, J., & Lacassin, R. (1999). Shear heating in continental strike-slip shear zones: Model and field examples. *Geophysical Journal International*, *136*(1), 19–40.

Li, X., Faure, M., Rossi, P., Lin, W., & Lahondère, D. (2015). Age of Alpine Corsica ophiolites revisited: Insights from in situ zircon U-Pb age and O-Hf isotopes. *Lithos*, *220-223*, 179–190.

Liati, A. (2005). Identification of repeated Alpine (ultra) high-pressure metamorphic events by U–Pb SHRIMP geochronology and REE geochemistry of zircon: The Rhodope zone of Northern Greece. *Contributions to Mineralogy and Petrology*, *150*, 608–630.

Liati, A., Gebauer, D., & Fanning, C. M. (2004). The age of ophiolitic rocks of the Hellenides (Vourinos, Pindos, Crete): First U–Pb ion microprobe (SHRIMP) zircon ages. *Chemical Geology*, *207*, 171–188. https://doi.org/10.1016/j.chemgeo.2004.02.010

Lopez-Sanchez, M. A., Aleinikoff, J. N.,Marcos, A., Martïnez, F. J., & Llana-Fünez, S. (2016). An example of low-Th/U zircon overgrowths of magmatic origin in a late orogenic Variscan intrusion: the San Ciprián massif (NW Spain). *Journal of the Geological Society*, *173*(2), 282–291.

Macdonald, F. R., Karabinos, P. M., Crowley, J. L., Hodgin, E. B., Crockford, P. W., & And Delano, J. W. (2017). Bridging the gap between the foreland and hinterland II: Geochronology and tectonic setting of ordovician magmatism and basin formation on the Laurentian margin of New England and Newfoundland. *American Journal of Science*, *317*, 555–596. https://doi.org/10.2475/05.2017.02

Maffione, M., & van Hinsbergen, D. J. J. (2018). Reconstructing plate boundaries in the Jurassic Neo-Tethys from the East and West Vardar Ophiolites (Greece and Serbia). *Tectonics*, *37*, 858–887. https://doi.org/10.1002/2017TC004790

Maffione, M., Thieulot, C., van Hinsbergen, D. J., Morris, A., Plümper, O., & Spakman, W. (2015). Dynamics of intraoceanic subduction initiation: 1. Oceanic detachment fault inversion and the formation of supra-subduction zone ophiolites. *Geochemistry, Geophysics, Geosystems*, *16*, 1753–1770. https://doi.org/10.1002/2015GC005746

Mako, C. A., & Caddick, M. J. (2018). Quantifying magnitudes of shear heating in metamorphic systems. *Tectonophysics*, *744*, 499–517. https://doi.org/10.1016/j.tecto.2018.07.003

Maffione, M., Morris, A., &Anderson, M. W. (2013). Recognizing detachment-mode seafloor spreading in the deep geological past. *Scientific Reports*, *3*, 2336. https://doi.org/10.1038/srep02336

Maluski, H., Bonneau, M., & Kienast, J. R. (1987). Dating the metamorphic events in the Cycladic area: $^{40}Ar/^{39}Ar$ data from metamorphic rocks of the island of Syros (Greece). *Bulletin de la Société Géologique de France*, *8*, 833–841.

Marcucci, M., Kodra, A., Pirdeni, A., & Gjata, T. (1994). Radiolarian assemblages in the Triassic and Jurassic cherts of Albania. *Ofioliti*, *19*.

Marcucci, M., & Prela, M. (1996). The LumiiZi (Puke) section of the Kalur Cherts: Radiolarian assemblages and comparison with other sectionsin northern Albania. *Ofioliti*, *21*(1), 71–76.

Marroni, M., Pandolfi, L., Saccani, E., & Zelic, M. (2004). Boninites from the Kopaonik area (Southern Serbia): new evidences for supra-subduction ophiolites in the Vardar zone. *Ofioliti*, *29*(2), 251–254.

Melidonis, N. G. (1980). The geological structure and mineral deposits of Tinos island (Cyclades, Greece). *Geology of Greece*, *13*, 1–80.

Meschede, M. (1986). A method of discriminating between different types of mid-ocean ridge basalts and continental tholeiites with the Nb-Zr-Y diagram. *Chemical Geology*, *56*, 207–218.

Mocek, B. (2001). Geochemical evidence for arc-type volcanism in the Aegean Sea: The blueschist unit of Siphnos, Cyclades (Greece). *Lithos*, *57*, 263–289. https://doi.org/10.1016/S0024-4937(01)00043-3

Mukasa, S. B., & Ludden, J. N. (1987). Uranium-lead ages of plagiogranites from the Troodos ophiolite, Cyprus, and their tectonic significance. *Geology*, *5*, 825–828.

Okrusch, M., Seidel, E., Kreuzer, H., & Harre, W. (1978). Jurassic age of metamorphism at the base of the Brezovica peridotite (Yugoslavia). *Earth and Planetary Science Letters*, *39*(2), 291–297.

Palin, R. M., White, R. W., Green, E. C. R., Diener, J. F. A., Powell, R., & Holland, T. J. B. (2016). High-grade metamorphism and partial melting of basic and intermediate rocks. *Journal of Metamorphic Geology*, *34*, 871–892. https://doi.org/10.1111/jmg.12212

Pallister, J. S., & Knight, R. J. (1981). Rare-earth element geochemistry of the Samail Ophiolite near Ibra, Oman. *Journal of Geophysical Research*, *86*(B4), 2673–2697.

Parlak, O., Çolakoğlu, A., Dönmez, C., Sayak, H., Yildirim, N., Türkel, A., & Odabaşi, İ. (2013). Geochemistry and tectonic significance of ophiolites along the İzmir–Ankara–Erzincan Suture Zone in northeastern Anatolia. *Geological Society, London, Special Publications*, *372*(1), 75–105.

Parlak, O., & Delaloye, M. (1999). Precise $^{40}Ar/^{39}Ar$ ages from the metamorphic sole of the Mersin ophiolite (southern Turkey). *Tectonophysics*, *301*, 145–158. https://doi.org/10.1016/S0040-1951(98)00222-4

Parsons, B., & Sclater, J. G. (1977). An analysis of the variation of ocean floor bathymetry and heat flow with age. *Journal of Geophysical Research*, *82*(5), 803–827.

Patzak, M., Okrusch, M., & Kreuzer, H. (1994). The Akrotiri Unit on the island of Tinos Cyclades, Greece: Witness to a lost terrane of Late Cretaceous age. *Neues Jahrbuch fu¨r Geologie und Pala¨ontologie, Abhandlungen*, *194*, 211–252.

Peacock, S. M. (1992). Blueschist-facies metamorphism, shear heating, and P-T-t paths in subduction shear zones. *Journal of Geophysical Research*, *97*(B12), 17693–17707.

Peacock, S. M. (1996). Thermal and petrologic structure of subduction zones. *Geophysical Monographs*, *96*, 119–133.

Pearce, J. A. (1983). Role of the subcontinental lithosphere in magma genesis at active continental margins. In C. J. Hawkesworth, & M. J. Norry (Eds.), *Continental basalts and mantle xenoliths*, (pp. 230–249). Nantwich: Shiva.

Pearce, J. A. (1996). A users guide to basalt discrimination diagrams. In D. A. Wyman (Ed.), *Trace element geochemistry of volcanic rocks: Applications for massive sulfide exploration*, *Geological Association of Canada Short Course Notes*, (Vol. 12, pp. 79–113).

Pearce, J. A. (2014). Immobile element fingerprinting of ophiolites. *Elements*, *10*(2), 101–108.

Pearce, J. A., & Cann, J. R. (1973). Tectonic setting of basic volcanic rocks determined using trace element analyses. *Earth and Planetary Science Letters*, *19*, 290–300.

Pearce, J. A., Harris, N. B., & Tindle, A. G. (1984). Trace element discrimination diagrams for the tectonic interpretation of granitic rocks. *Journal of petrology*, *25*(4), 956–983.

Peters, K., Smit, M., van Hinsbergen, D., van Roermund, H., & Brouwer, F. (2017). The longevity of Neotethyan metamorphic soles from Lu-Hf garnet chronology. *Geophysical Research Abstracts*, *19*.

Philpotts, A. R. (1976). Silicate liquid immiscibility: Its probable extent and petrogenetic significance. *American Journal of Science.*, *276*, 1147–1177.

Prela, M., Chiari, M., & Marcucci, M. (2000). Jurassic radiolarian biostratigraphy of the sedimentary cover of ophiolites in the Mirdita area, Albania: New data. *Ofioliti*, *25*(1), 55–62.

Powell, R. (1985). Regression diagnostics and robust regression in geothermometer/geobarometer calibration: the garnet-clinopyroxene geothermometer revisited. *Journal of metamorphic Geology*, *3*(3), 231–243.

Powell, R., & Holland, T. J. B. (1988). An internally consistent dataset with uncertainties and correlations: 3. Applications to geobarometry, worked examples and a computer program. *Journal of metamorphic Geology*, *6*(2), 173–204.

Ravna, K. (2000). The garnet-clinopyroxene Fe2+−Mg geothermometer: an updated calibration. *Journal of metamorphic Geology*, *18*(2), 211–219.

Reagan, M. K., Ishizuka, O., Stern, R. J., Kelley, K. A., Ohara, Y., Blichert-Toft, J., et al. (2010). Fore-arc basalts and subduction initiation in the zu-Bonin-Mariana system. *Geochemistry, Geophysics, Geosystems*, *11*, Q03X12. https://doi.org/10.1029/2009GC002871

Resimić-Šarić, K., Cvetković, V., & Balogh, K. (2005). Radiometric K/Ar data as an evidence of the geodynamic evolution of the Ždraljicaophiolitic complex (central Serbia). *Annales Géologiques de la Péninsule Balkanique*, *66*, 73–79.

Resimić-Šarić, K., Cvetković, V., Balogh, K., & Koroneos, A., (2006), Main characteristics of ophiolitic complexes within the eastern branch of the Vardar Zone Composite Terrane in Serbia. In International Symposium on the Mesozoic ophiolite belts of the northern part of the Balkan Peninsula, Belgrade (Serbia) and Banja Luka (Bosnia and Herzegovina), pp. 112–115.

Rice, J. R. (2017). Heating, weakening and shear localization in earthquake rupture. *Philosophical Transactions of the Royal Society A: Mathematical, Physical and Engineering Sciences*, *375*. http://doi.org/10.1098/rsta.2016.0015

Ricou, L. E., & Godfriaux, I. (1995). Review on the Paikon multiple window and the structure of the Vardar in Greece French with abridged English. *Academie des Sciences Ser. II Sci. la Terre des Planetes*, *321*(7).

Rioux, M., Garber, J., Bauer, A., Bowring, S., Searle, M., Kelemen, P., & Hacker, B. (2016). Synchronous formation of the metamorphic sole and igneous crust of the Semail ophiolite: New constraints on the tectonic evolution during ophiolite formation from high-precision U–Pb zircon geochronology. *Earth and Planetary Science Letters*, *451*, 185–195.

Roberts, N. M. W., Thomas, R. J., & Jacobs, J. (2016). Geochronological constraints on the metamorphic sole of the Semail ophiolite in the United Arab Emirates. *Geoscience Frontiers*, *7*, 609–619.

Robertson, A. H. F. (2002). Overview of the genesis and emplacement of Mesozoic ophiolites in the eastern Mediterranean Tethyan region. *Lithos*, *65*, 1–67.

Robertson, A. H. F. (2006). Contrasting modes of ophiolite emplacement in the Eastern Mediterranean region. In A. H. F. Robertson, & D. Mountrakis (Eds.), *Tectonic development of the eastern Mediterranean region*, *Geological Society of London Special Publication*, (Vol. 260, pp. 235–261).

Roddick, J. C., Cameron, W. E., & Smith, A. G. (1979). Permo-Triassic and Jurassic ^{40}Ar-^{39}Ar ages from Greek ophiolites and associated rocks. *Nature*, *279*(5716), 788–790. https://doi.org/10.1038/279788a0

Rosenberg, C. L., & Stünitz, H. (2003). Deformation and recrystallization of plagioclase along a temperature gradient: an example from the Bergell tonalite. *Journal of Structural Geology*, *25*(3), 389–408.

Rubatto, D. (2017). Zircon: The metamorphic mineral. *Reviews in Mineralogy and Geochemistry*, *83*(1), 261–295. https://doi.org/10.2138/rmg.2017.83.9

Saccani, E., Bortolotti, V., Marroni, M., Pandolfi, L., Photiades, A., & Principi, G. (2008). The Jurassic ass ociation of back arc basin ophiolites and calc-alkaline volcanics in the Guevgueli complex (northern Greece): Implication for the evolution of the Vardar zone. *Ofioliti*, *33*(2), 209–227.

Saccani, E., & Photiades, A. (2004). Mid-ocean ridge and supra-subduction affinities in the Pindos ophiolites (Greece): Implications for magmagenesis in a forearc setting. *Lithos*, *73*(3–4), 229–253. https://doi.org/10.1016/j.lithos.2003.12.002

Šarić, K., Cvetković, V., Romer, R. L., Christofides, G., & Koroneos, A. (2009). Granitoids associated with East Vardar ophiolites (Serbia, F. Y.R. of Macedonia and northern Greece): Origin, evolution and geodynamic significance inferred from major and trace element data and Sr-Nd-Pb isotopes. *Lithos*, *108*(1-4), 131–150. https://doi.org/10.1016/j.lithos.2008.06.001

Sarıfakıoğlu, E., Dilek, Y., Uysal, I., (2012), The Petrogenesis and Geodynamic Significance of Bahçe (Osmaniye) Ophıolite. 5th Geochemistry Symposium, pp. 112–113.

Saunders, A. D. (1984). The rare earth element characteristics of igneous rocks from the ocean basins. In P. Henderson (Ed.), *Rare earth element geochemistry*, (pp. 205–236). Amsterdam: Elsevier.

Schmid, S. M., Bernoulli, D., Fügenschuh, B., Matenco, L., Schefer, S., Schuster, R., et al. (2008). The Alpine-Carpathian-Dinaridic orogenic system: Correlation and evolution of tectonic units. *Swiss Journal of Geosciences*, *101*, 139–183. https://doi.org/10.1007/s00015-008-1247-3

Schmidt, M. W. (1992). Amphibole composition in tonalite as a function of pressure: an experimental calibration of the Al-in-hornblende barometer. *Contributions to mineralogy and petrology*, *110*(2–3), 304–310

Searle, M., Warren, C. J., Waters, D. J., & Parrish, R. R. (2004). Structural evolution, metamorphism and restoration of the Arabian continental margin, Saih Hatat region, Oman. *Journal of Structural Geology.*, *26*, 451–473.

Searle, M. P., Waters, D. J., Garber, J. M., Rioux, M., Cherry, A. G., & Ambrose, T. K. (2015). Structure and metamorphism beneath the obducting Oman ophiolite: Evidence from the Bani Hamid granulites, northern Oman mountains. *Geosphere*, *11*(6), 1812–1836.

Searle, M. P., & Cox, J. (1999). Tectonic setting, origin, and obduction of the Oman ophiolite. *Geological Society of America Bulletin*, *111*, 104–122.

Searle, M. P., & Cox, J. (2002). Subduction zone metamorphism during formation and emplacement of the Semail ophiolite in the Oman Mountains. *Geological Magazine*, *139*, 241–255.

Searle, M. P., & Lamont, T. N. (2019). Compressional metamorphic core complexes, low-angle normal faults and extensional fabrics in compressional tectonic settings. *Geological Magazine*, 1–18. https://doi.org/10.1017/S0016756819000207

Searle, M. P., & Malpas, J. (1982). Petrochemistry and origin of sub-ophiolitic metamorphic and related rocks in the Oman Mountains. *Journal of the Geological Society*, *139*, 235–248.

Sharp, I. R., & Robertson, A. H. (2006). Tectonic-sedimentary evolution of the western margin of the Mesozoic Vardar Ocean: Evidence from the Pelagonian and Almopias zones, northern Greece. *Geological Society, London, Special Publications*, *260*(1), 373–412.

Smith, A. G., & Spray, J. G. (1984). A half-ridge transform model for the Hellenic-Dinaric ophiolites in Dixon, E., and Robertson, A.H.F. (Eds.), The geological evolution of the eastern Mediterranean. *Geological Society of London Special Publications*, *17*, 629–644.

Schmidt, M. W., & Poli, S. (2004). Magmatic epidote. *Reviews in Mineralogy and Geochemistry*, *56*(1), 399–430.

Sostarić, B. S., Palinkaš, A. L., Neubauer, F., Cvetković, V., Bernroider, M., & Genser, J. (2014). The origin and age of the metamorphic sole from the Rogozna Mts., Western Vardar Belt: New evidence for the one-ocean model for the Balkan ophiolites. *Lithos*, *192–195*, 39–55. https://doi.org/10.1016/j.lithos.2014.01.011

Spray, J. G., Bébien, J., Rex, D. C., & Roddick, J. C. (1984). Age constraints on the igneous and metamorphic evolution of the Hellenic-Dinaric ophiolites. *Geological Society London, Special Publications*, *17*, 619–627. https://doi.org/10.1144/GSL.SP.1984.017.01.48

Spray, J. G., & Roddick, J. C. (1980). Petrology and ^{40}Ar/^{39}Ar geochronology of some Hellenic sub-ophiolite metamorphic rocks. *Contributions to Mineralogy and Petrology, v.*, *72*(1), 43–55. https://doi.org/10.1007/BF00375567

Spulber, S. D., & Rutherford, M. J. (1983). The origin of rhyolite and plagiogranite in oceanic crust: An experimental study. *Journal of Petrology*, *24*(1), 1–25.

Stacey, J. S., & Kramers, J. D. (1975). Approximation of terrestrial lead isotope evolution by a two-stage model. *Earth and Planetary Science Letters*, *26*, 207–221.

Stein, C. A., & Stein, S. (1992). A model for the global variation in oceanic depth and heat flow with lithospheric age. *Nature*, *359*(6391), 123–129.

Stern, R. J. (2004). Subduction initiation: Spontaneous and induced. *Earth and Planetary Science Letters*, *226*, 275–292.

Stouraiti, C., Pantziris, I., Vasilatos, C., Kanellopoulos, C., P Mitropoulos, P., Pomonis, P., et al. (2017). Ophiolitic remnants from the upper and intermediate structural unit of the Attic-Cycladic Crystalline Belt (Aegean, Greece): Fingerprinting geochemical affinities of magmatic precursors. *Geosciences*, *7*, 14. https://doi.org/10.3390/geosciences7010014

Sun, S. S., & McDonough, W. F. (1989). Chemical and isotopic systematics of oceanic basalts: Implications for mantle composition and process. In A. D. Saunders, & J. M. Norry (Eds.), *Magmatism in the ocean basins*, *Geological Society, London, Special Publications*, (Vol. 42, pp. 313–345).

Tarling, M. S., Smith, S. A. F., Viti, C., & Scott, J. M. (2018). Dynamic earthquake rupture preserved in a creeping serpentinite shear zone. *Nature communications*, *9*(1), 3552–3552.

Thuizat, R., Whitechurch, H., Montigny, R., & Juteau, T. (1981). K-Ar dating of some infra-ophiolitic metamorphic soles from the Eastern Mediterranean: New evidence for oceanic thrustings before obduction. *Earth and Planetary Science Letters*, *52*(2), 302–310, ISSN 0012-821X. https://doi.org/10.1016/0012-821X(81)90185-0

Tomaschek, F., Kennedy, A., Villa, I. M., Lagos, M., & Ballhaus, C. (2003). Zircons from Syros, Cyclades, Greece—Recrystallization and mobilization of zircon during high-pressure metamorphism. *Journal of Petrology*, *44*, 1977–2002.

Topuz, G., Göçmengil, G., Rolland, Y., Çelik, Ö. F., Zack, T., & Schmitt, A. K. (2012). Jurassic accretionary and ophiolite from northeast Turkey: No evidence for the Cimmerian continental ribbon. *Geology*, *41*, 255–258. https://doi.org/10.1130/ G33577.1

Tremblay, A., Meshi, A., & Bédard, J. H. (2009). Oceanic core complexes and ancient oceanic lithosphere: Insights from Iapetan and Tethyanophiolites (Canada and Albania). *Tectonophysics*, *473*(1–2), 36–52. https://doi.org/10.1016/j.tecto.2008.08

Tremblay, A., Meshi, A., Deschamps, T., Goulet, F., & Goulet, N. (2015). The Vardar zone as a suture for the Mirdita ophiolites, Albania: Constraints from the structural analysis of the Korabi-Pelagonia zone. *Tectonics*, *34*, 352–375. https://doi.org/10.1002/2014TC003807

van Hinsbergen, D. J., Peters, K., Maffione, M., Spakman, W., Guilmette, C., Thieulot, C., et al. (2015). Dynamics of intraoceanic subduction initiation: 2. Suprasubduction zone ophiolite formation and metamorphic sole exhumation in context of absolute plate motions. *Geochemistry, Geophysics, Geosystems*, *16*, 1771–1785.

Vissers, R. L. M., & Meijer, P. T. (2012). Iberian plate kinematics and Alpine collision in the Pyrenees. *Earth Science Reviews*, *114*, 61–83.

Wada, I., Wang, K., He, J., & Hyndman, R. D. (2008). Weakening of the subduction interface and its effects on surface heat flow, slab dehydration, and mantle wedge serpentinization. *Journal of Geophysical Research: Solid Earth*, *113*(B4).

Wakabayashi, J., & Dilek, Y. (2000). *Spatial and temporal relationships between ophiolites and their metamorphic soles: A test of models of forearc ophiolite genesis*, *Geological Society of America, Special Papers*, (pp. 53–64).

Wakabayashi, J., & Dilek, Y. (2003). What constitutes 'emplacement' of an ophiolite? Mechanisms and relationship to subduction initiation and formation of metamorphic soles. In S. Dilek, & P. T. Robertson (Eds.), *Ophiolites in earth's history*, *Geological Society of London Special Publications*, (Vol. 218, pp. 427–447).

Waters, D. J., & Lovegrove, D. P. (2002). Assessing the extent of disequilibrium and overstepping of prograde metamorphic reactions in metapelites from the Bushveld Complex aureole, South Africa. *Journal of Metamorphic Geology*, *20*(1), 135–149.

White, R. W., Powell, R., Holland, T. J., Johnson, T. E., & Green, E. C. (2014). New mineral activity-composition relations for thermodynamic calculations in metapelitic systems. *J. Meta. Geol.*, *32*(261–286. https://doi.org/10.1111/jmg.12071

White, R. W., Powell, R., & Johnson, T. E. (2014). The effect of Mn on mineral stability in metapelites revisited: new a-x relations for manganese-bearing minerals. *Journal of Metamorphic Geology*, *32*, 809–828. https://doi.org/10.1111/jmg.12095

Wood, D. A., Joron, J. L., & Treuil, M. (1979). A reappraisal of the use of trace elements to classify and discriminate between magma series erupted in different tectonic settings. *Earth and Planetary Science Letters*, *45*, 326–336.

Yakymchuk, C., Kirkland, C. L., & Clark, C. (2018). Th/U ratios in metamorphic zircon. *Journal of Metamorph. Geology*, *36*, 715–737. https://doi.org/10.1111/jmg.12307

Zachariadis, P. T., (2007), Ophiolites of the eastern Vardar Zone, N. Greece, PhD thesis, University of Mainz, Mainz, Germany. Accesible at: https://publications.ub.uni-mainz.de/theses/volltexte/2007/1355/pdf/1355.pdf

Zeffren, S., Avigad, D., Heimann, A., & Gvirtzman, Z. (2005). Age resetting of hanging wall rocks above a low-angle detachment fault: Tinos Island (Aegean Sea). *Tectonophysics*, *400*, 1–25.

Zen, E. A., & Hammarstrom, J. M. (1984). Magmatic Epidote and Its Petrologic Significance. *Geology*, *12*(9), 515–518.